Enhancing performance of a vanadium redox flow battery by employing modified serpentine channels

Thesis submitted in partial fulfilment

for the Award of Degree

Doctor of Philosophy

By

HARSH SHARMA

RAJIV GANDHI INSTITUTE OF PETROLEUM TECHNOLOGY

JAIS, INDIA – 229304

PCH16002 2021

CERTIFICATE

It is certified that the work contained in the thesis titled "***Enhancing performance of a vanadium redox flow battery by employing modified serpentine channels***" *by* "***Harsh Sharma***" has been carried out under our supervision and that this work has not been submitted elsewhere for a degree.

It is further certified that the student has fulfilled all the requirements of Comprehensive, Candidacy and SOTA/Open seminar.

Supervisor
(Dr. Milan Kumar)

DECLARATION BY THE CANDIDATE

I, "***Harsh Sharma***", certify that the work embodied in this thesis is my own bona fide work and carried out by me under the supervision of "***Dr. Milan Kumar***" from "*July 2016*" *to* "*September 2021*" at Rajiv Gandhi Institute of Petroleum Technology, Jais (India). The matter embodied in this thesis has not been submitted for the award of any other degree. I declare that I have faithfully acknowledged and given credits to the research workers wherever their works have been cited in my work in this thesis. I further declare that I have not willfully copied any other's work, paragraphs, text, data, results, etc., reported in journals, books, magazines, reports dissertations, theses, etc., or available at websites and have not included them in this thesis and have not cited as my own work.

Date:
Place:

Harsh Sharma
Roll No: PCH16002

CERTIFICATE BY THE SUPERVISOR

It is certified that the above statement made by the student is correct to the best of our knowledge.

(Dr. Milan Kumar)	**(Dr. Amit Ranjan)**
(Supervisor)	Head of Department
	(CE & BE)

CERTIFICATE

CERTIFIED that the work contained in the thesis titled "**Enhancing performance of a vanadium redox flow battery by employing modified serpentine channels**" by **Mr. Harsh Sharma** has been carried out under my supervision. It is also certified that he fulfilled the mandatory requirement of TWO quality publications arose out of his thesis work.

It is further certified that the two publications (copies enclosed) of the aforesaid **Mr. Harsh Sharma** have been published in the Journals indexed by –

(a) SCI

(b) SCI Extended

(c) SCOPUS

Supervisor & Convener, DPGC

(Dr. Milan Kumar)

COPYRIGHT TRANSFER CERTIFICATE

Title of the Thesis: Enhancing performance of a vanadium redox flow battery by employing modified serpentine channels

Name of the Student: Harsh Sharma

Copyright Transfer

The undersigned hereby assigns to the Rajiv Gandhi Institute of Petroleum Technology Jais all rights under copyright that may exist in and for the above thesis submitted for the award of the "Doctor of Philosophy".

Date: *Harsh Sharma*

Place: Roll No: PCH16002

Note: However, the author may reproduce or authorize others to reproduce material extracted verbatim from the thesis or derivative of the thesis for author's personal use provided that the source and the Institute's copyright notice are indicated.

Dedicated to my beloved parents, wife,
and my son Kishu

Acknowledgements

With god's blessings, finally, after a long journey of five years, I have reached the dissertation stage. For this journey, first and foremost, I would like to express my deep gratitude to my thesis supervisor, Dr. Milan Kumar, for his outstanding support and for showing confidence in me throughout this wonderful journey of five years. Without him, I would not have been able to reach at this stage. To accomplish my doctoral degree, he groomed me from scratch and made my entire journey simple and easy. He has given me full liberty to avail the research facility of the lab. I have gained a lot of knowledge under his guidance. He always encouraged me and keep me motivated even in the toughest situation. Whenever I had faced any problem, he never disappointed me, his door always remained open for me to solve my problems. My entire experimental work and deep understandings to analyze the things could not have been possible without him.

I would like to thank my RPEC member, Dr. Amit Ranjan for evaluating my research work and sharing the lab with us. I would also like to thank Dr. Arshad Aijaz (RPEC member) for his cordial support. I also want to Acknowledge Dr. Debashis Panda for availing his lab facility. Apart from I am also special thankful to Mr. Virendra Singh Jr. Tech. Superintendent, 4i lab IIT Kanpur who helped me in fabricating the flow channels, without his support the work did not seem to be easy.

I am also indebted to Rajiv Gandhi Institute of Petroleum Technology (RGIPT), Jais, for providing the financial assistance as well as research facility to carry out my research work without any hindrance. Additionally, I am grateful to DST-SERB, Government of India, for funding the research work.

I feel blessed to have wonderful parents and sister, and wholeheartedly thank them for their immense love, support, and encouragement. They gave me too much strength in overcoming the difficulties. I would like to thank my wife who stood with me in every situation and my child who made this journey completed with unforgettable moments. Finally, I would like to thank Dr. Shama Perween, Mr. Bijoy Kumar Purohit, Mr. Aash Mohammad, and Mr. Anil Verma for their valuable support and with whom I have shared several moments of happiness, excitement and anxiety as well as the friends of RGIPT, who directly or indirectly supported me in this whole journey made my Ph.D. journey, an unforgettable one. I am grateful to them for their support. You are fully deserving of all of my accolades for support.

….Harsh Sharma

Table of Contents

Chapter 5: Higher efficiency of a vanadium redox flow battery integrated with modified serpentine flow patterns..95

Chapter 6: Energy efficient flow path for improving electrolyte distribution in a vanadium redox flow battery..115

List of Figures

This page is intentionally kept blank

List of Tables

List of Abbreviations

ABBREVIATION	**MEANING**
AEM	Anion Exchange Membrane
CE	Coulombic Efficiency
CS	Conventional Serpentine
DI	Deionized Water
DoD	Depth of Discharge
DMFC	Direct Methanol Fuel Cell
EE	Energy Efficiency
EIS	Electrochemical Impedance Spectroscopy
ESS	Energy Storage System
HFR	High Frequency Response
IDFF	Interdigitated Flow Field
MEA	Membrane Electrode Assembly
OCP	Open Circuit Potential
PEM	Proton Exchange Membrane
PEMFC	Polymer Electrolyte Membrane Fuel Cell
PSB	Polysulfide-Bromine Battery
SMS	Split Merged Serpentine
SOC	State of Charge
SS	Split Serpentine
SWS	Sinusoidal Wave-type Serpentine
VE	Voltage Efficiency
VRFB	Vanadium Redox Flow Battery

ZBB	Zinc Bromine Battery

List of Symbols

SYMBOL	**PARAMETERS**	**UNIT**
C_{dl}	Double layer capacitance	farad or F
C_O^*	Concentration of species *O* in bulk solution	mol L^{-1}
C_R^*	Concentration of species *R* in bulk solution	mol L^{-1}
E	Reduction Potential	V
E^0	Standard reduction potential	V
E_{cell}^0	Standard cell potential	V
E_{eq}	Equilibrium cell potential	V
F	Faraday's constant	C/mol
ΔG	Gibb's free energy change	J
i	Current	A
i_0	Exchange current	A
j_o	Exchange current density	mA cm^{-2}
j_{peak}	Peak current density	mA cm^{-2}
M	Concentration	mol L^{-1}
n	Number of electrons	-
P_{peak}	Peak current density	mW cm^{-2}
Q_{th}	Theoretical capacity	Ah
R	Universal gas constant	J mol^{-1} K^{-1}
R_{ct}	Charge-transfer resistance	ohm or Ω
R_s	Ohmic resistance	ohm or Ω
t	Time	s or h varies
V_{peak}	Peak voltage	V
Z_{re}	Real Impedance	ohm or Ω
ω	Frequency	Hz
η_a	Activation overpotential	V
η_{iR}	Ohmic overpotential	V

η_{mt}	Mass-transfer overpotential	V
α	Charge-transfer coefficient	-
γ_i	Activity coefficient	-

Preface

Vanadium redox flow battery (VRFB) system is an electrochemical energy device that converts chemical energy into electrical energy. One of the major advantages of this energy device is that power and energy capacities can be independently scaled up. A VRFB consists of positive (VO_2^+/VO^{2+}) and negative (V^{3+}/V^{2+}) electrolyte tanks, a cell/cell-stack and two pumps. During charging, VO^{2+} is oxidized into VO_2^+ at positive electrode and V^{3+} is reduced into V^{2+} at negative electrode, whereas in discharging the reverse reactions take place at both electrodes. The cell is constructed by sandwiching membrane between two porous electrodes, placing a flow channel both sides. The role of a flow channel is to distribute electrolyte in the porous space of electrode which helps in its efficient utilization and in overcoming mass-transfer resistance of electroactive species. The non-uniform distribution of electrolyte hampers the performance and results in uneven current distribution in electrode.

The focus of current research work is to develop flow channels which will help in achieving better performance of the battery. Motivation came from closely similar systems, such as plate-type heat exchangers and micro reactors, where corrugated flow patterns are employed leading to intensified heat and mass-transfer. Three flow patterns, Split Serpentine (SS), Split-Merge Serpentine (SMS), and Sinusoidal Wave-type Serpentine (SWS), were designed and developed, and were fabricated on graphite plate; with an active area of ~10 cm^2. For comparison, a Conventional Serpentine (CS) channel of same area was also fabricated. The performance of the battery was analyzed through polarization curves – illustrating potential loss stemming from kinetic, ohmic and mass-transfer resistance – were obtained by varying flow rates (30, 50, 80, and 120 mL min^{-1}) of electrolyte.

Electrochemical Impedance Spectroscopy (EIS) was performed to quantify these resistances. High frequency response of EIS was used to obtain iR-free polarization curves and power density which eliminates the effect of ohmic resistances arising from membrane and electrolyte solutions. The Energy Efficiency (EE) of the battery employing these channels was calculated from discharge-charge cycles, measured at 20 and 40 mA cm^{-2} current densities. At each current density, two electrolyte flow rates of 50 and 100 mL min^{-1} were used. The detailed analysis of results show that the SS channel has a higher distribution ability of electrolyte over the electrode surface whereas the SWS channels shows higher stability of potentials even withdrawing higher current from the battery. Based on charge-transfer resistance, the kinetics is found slower with CS channel, while kinetics is very fast in SMS channel. The kinetics is almost same with SS and WS channels. Higher power density of the battery with designed flow patterns, in comparison to that with a CS channel, indicates larger area utilization of the electrode.

The longest discharge-charge time in SS channel suggests that the distribution of electrolytes is found better in the SS channel leading the battery will run longer with the SS channel compared to CS, SMS, and SWS channels. The SMS channel performed better in terms of achieving efficiency; CE and EE. Additionally, the battery integrated with the SMS channel is capable to achieve higher efficiency even at a lower flow rate which may reduce the surplus cost of pumping the electrolytes.

Thesis Organization

Chapter 1: This chapter presents a brief introduction of different types of energy storage devices, such as conventional batteries, supercapacitors, and flow batteries, along with their working principles, advantages-disadvantages, applications, technical features, and associated reactions. A comparison of technical advantages of vanadium redox flow battery (VRFB) over other batteries are explained. The various components of VRFB are discussed in details. Terminologies and performance measuring parameters used in assessment of battery are also discussed in brief. Technical challenges with VRFB such as high mass-transfer resistance and slow reaction kinetics leading to performance loss and how to overcome it using flow channels are explained. Motivation of this research work comes from plate heat exchanger and microreactors. At the end this chapter, conclusion are presented with objectives to carry out this reach work.

Chapter 2: This chapter covers the findings of the various research groups working in the areas of VRFB, polymer electrolyte membrane (PEM), and direct methanol fuel cells (DMFC). The reported literature work is mainly focused on types of flow channels employed in VRFB to improve its performance.

Chapter 3: This chapter is comprised of experimental setup of VRFB used in the current work along with details of materials used, working procedures, and different electrochemical measurement methods used to carry out experiments. A single-cell assembly of VRFB was integrated with fabricated channels to examine the performance. Experimental troubleshooting and electrochemical measurements are also discussed.

Chapter 4: This chapter presents the published research work. It comprises the performance of VRFB integrated with Split Serpentine (SS), Split-Merged Serpentine (SMS), and Conventional Serpentine (CS) channels, through polarization curves and EIS measurements with varying flow rates: 30, 50, 80, and 120 mL min^{-1} of electrolyte. The effect of increasing flow rates of electrolyte on peak power densities, peak current density, and limiting current peak densities are determined. Result shows that 2.5 and 5 times higher current density can be withdrawn using SMS and SS channels. The highest peak power density is achieved at 120 mL min^{-1} in SS channel followed by SMS channel and CS channel. EIS results shows that charge-transfer resistance is lowest in SMS and highest in CS channel.

Chapter 5: The chapter presents the research work of manuscript submitted for the publication and its extended work is presented in Chapter 4. Discharge and charge behavior of CS, SS, and SMS channels VRFB in each flow channels at two different flow rates of electrolyte (50 and 100 mL min^{-1}) and current densities (20 and 40 mA cm^{-2}) are determined and analyzed in this chapter. The effect of increasing flow rate of electrolyte on discharge-charge time, discharge-charge overpotential are compared and discussed in details. Coulombic efficiency (CE) and energy efficiency (EE) are calculated at above flow rates and current densities and are presented. The highest CE is achieved in SMS channel (95.2%) followed by SS (91.4%) and CS (82.2%) channels at 40 mA cm^{-2} and 100 mL min^{-1}. The highest EE values for respective channels are: 77.4%, 73.6% and 60.1% at 20 mA cm^{-2} and 100 mL min^{-1}.

Chapter 6: The chapter presents the research work of the publication. The performance of VRFB integrated with Sinusoidal Wave-type Serpentine (SWS) channel is examined with the help of obtained polarization curves, EIS measurements and discharge-charge cycles performed at varying flow rates of electrolyte. Results show that increasing flow rates lead to decrease in potential loss. Mass-transfer overpotential is low even at 30 mL min^{-1}, and at 120 mL min^{-1}, the overpotential is negligible even at very high current density of 500 mA cm^{-2}. EIS measurements show that charge-transfer resistance decreases with increasing flow rates and is lower than that for conventional serpentine flow pattern. These results indicate that better electrolyte distribution is achieved using SWS channels. The coulombic efficiency > 91%, and energy efficiency of ~73% were achieved.

At the end of thesis, overall conclusions and future scope of work are presented. Pressure drop across the VRFB integrated with fabricated channels are theoretically calculated using appropriate analytical expressions and is presented in Appendix.

Chapter 1: Introduction

1.1 Introduction to energy storage devices

The demand of energy is increasing sharply as compared to the production, harvesting and storage from renewable sources worldwide. The increasing gap between these two has now become a serious challenge for the world. For many decades, people have been utilizing conventional energy resources such as coal, oil, and natural gas to fulfill their basic needs [1]. The sharp rise in the price of these resources have become a big barrier for consumers. Moreover, these energy resources releases toxic gases: CO_2, SO_2, CO, NO_x on burning, leading to global warming and several health issues [2–4]. Now the world is aggressively looking for a better substitute that must be cost effective and environmentally benign by harvesting and storing energy from wind and solar sources. However, one of the barriers in deploying these energy resources is their intermittent nature [5–7]. The energy produced is strongly dependent on climate and weather conditions, energy production will be high when sunlight is intense and the wind is blowing [8]. This unpredictable nature is one of the major challenges in directly integrating with electrical power grids. If energy from wind energy is harvested far from the places, where continuous supply of electricity is necessary – this leads to transmission loss. Unpredictability and transmission losses are some of the reasons for limited production of energy from wind and solar power.

To increase energy harvestation effectively, storing energy, when available is more pertinent, viable option. In the present scenario, the technology worldwide emerging in the direction of storing energy and using it for future use, employing energy storage devices. The integration of such devices with electric grids is one of the key solutions to overcome the hindrance caused by weather conditions and geographical locations [9].

There are number of energy storage devices in existence ranging from commercially available conventional batteries, such as Pb-acid, Li-ion, and Ni-Cd, to the more advanced supercapacitors and flow batteries. A diagram indicating various types of energy storage devices is shown in Figure 1.1. The main difference between conventional batteries, flow batteries, and supercapacitors is how the energy is stored and used. The energy in conventional batteries is stored in electrodes and/or in electrolyte, all placed in a closed compartment. Flow batteries store energy similar to conventional one, but electrolytes are pushed into externally. The charging and discharging of conventional and flow batteries are accomplished by electrochemical conversion of chemical energy to electrical energy. Unlike batteries, the energy storage in supercapacitors or ultra-capacitors is based on electric charge separation at the electrode-electrolyte interface.

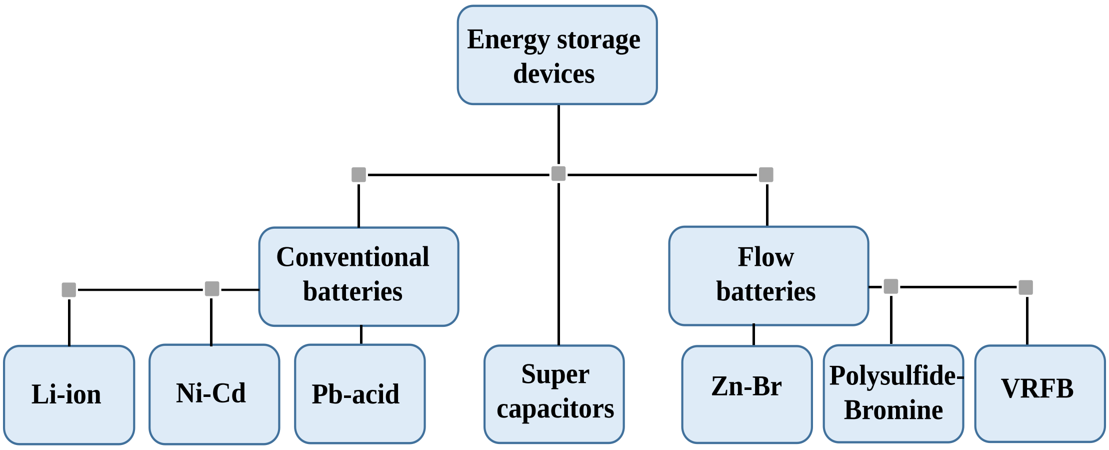

Figure 1.1. Types of energy storage devices: conventional batteries, supercapacitors, and flow batteries.

1.2 Conventional batteries

1.2.1 Lead-acid battery

The lead-acid battery is a low-cost device and is mostly used for small and medium-scale energy storage applications where power of good quality and uninterrupted power supply are required. It is generally used for small and medium-scale energy storage like for power quality and uninterruptable power supply. Lead-acid battery consists of electrodes/plates immersed in the H_2SO_4 electrolyte. Such as Lead oxide (PbO_2) is used as positive electrode and spongy lead (Pb) as negative electrode separated by a polyethylene microporous membrane. During discharging, PbO_2 reduces generating $PbSO_4$ and Pb oxidizes to generate $PbSO_4$ at positive and negative electrodes, respectively. The membrane allows sulfate ions to pass through during operations. The process continues until any of PbO_2, H_2SO_4, or Pb exhausts. During charging reverse reactions occur, regenerating them. The overall standard cell potential of the battery is around 2.0 V. The electrode reactions occurring at positive and negative electrodes are as follows:

Positive electrode:

$$PbO_2 + H_2SO_4 + 2H^+ + 2e \underset{\text{Charging}}{\overset{\text{Discharging}}{\rightleftarrows}} PbSO_4 + 2H_2O;\ E^0 = 1.68\text{ V} \tag{1.1}$$

Negative electrode:

$$Pb + H_2SO_4 \underset{\text{Charging}}{\overset{\text{Discharging}}{\rightleftarrows}} PbSO_4 + 2H^+ + 2e;\ E^0 = -0.35\text{ V} \tag{1.2}$$

The lead-acid battery has several advantages such as high efficiency of approximately 80–90%, low self-discharge and energy density of 20–35 Wh kg^{-1} [10,11]. It has service life of approximately 15 years [12]. The disadvantages of this battery include poor life cycle of ~1500, and low depth of discharge, up to 80% [10,13]. The battery uses Pb which is prone to corrosion when immersed in H_2SO_4 electrolyte. It generates explosive hydrogen gas and corrosive vapors through gassing reactions. Further, lead is a hazardous heavy metal and poses risk to human health and the environment.

1.2.2 Li-ion battery

The lithium-ion battery is the most prominent rechargeable battery since 1990s and is widely used in various portable applications, such as electric vehicles, electronic devices, mobile phones, etc. because of its high energy density. This battery employs positive and negative electrodes, the positive material is made of lithiated metal oxide ($LiCoO_2$) and negative electrode is made of carbon or graphite in a layer form, separated by lithium salt electrolyte ($LiPF_6$) dissolved in organic solvent to facilitate the movement of lithium ions during charge and discharge. The electrode reactions at both positive and negative electrode are:

Positive electrode:

$$Li_{1-x}CoO_2 + xLi^+ + xe \underset{\text{Charging}}{\overset{\text{Discharging}}{\rightleftarrows}} LiCoO_2;\ E^0 = 2.74\ \text{V} \tag{1.3}$$

Negative electrode:

$$Li_xC_6 \underset{\text{Charging}}{\overset{\text{Discharging}}{\rightleftarrows}} xLi^+ + 6C + xe;\ E^0 = -0.85\ \text{V} \tag{1.4}$$

where x varies from 0 to 0.45 for positive electrode and 0 to 1 for negative electrode [14]. During discharging, Li^+ reduces to $LiCoO_2$ at positive electrode, while at negative electrode, Li deposited over carbon oxidizes forming Li^+ ions which traverse to positive electrode. The advantages of this battery over other batteries are high round trip efficiency up to 95%, high life cycle of around ~5000 cycles, high energy density of about 100–200 Wh kg^{-1} and relatively low self-discharge [10,11,15]. This battery also has relatively higher cell potential of around 3.6 V. The higher manufacturing cost of more than $600/kWh is one of the main disadvantages of this battery. This derives from special packaging and internal overcharge protection circuits to avoid the deposition of metallic lithium at the negative electrode which may lead to explosion [13].

Other disadvantages include sensitivity towards high temperatures, such as overheating problems; overcharging of the battery may lead to form highly flammable metallic lithium. However, continual advancement in exploring cheaper electrode materials and electrolytes has made them feasible for future electrical grid applications.

1.2.3 Ni-Cd battery

The Ni-Cd alkaline battery was first introduced in the early 20th century. It utilizes nickel oxyhydroxide (*NiOOH*) as positive electrode and metallic cadmium (Cd) as negative electrode [11]. The battery has cell potential of 1.3 V. The chemical reactions taking place during discharging and charging are as follows [16]:

Positive electrode:

$$2NiO(OH) + 2H_2O + 2e \underset{\text{Charging}}{\overset{\text{Discharging}}{\rightleftarrows}} 2Ni(OH)_2 + 2OH^-;\ E^0 = 0.49\ \text{V} \qquad (1.5)$$

Negative electrode:

$$Cd + OH^- \underset{\text{Charging}}{\overset{\text{Discharging}}{\rightleftarrows}} Cd(OH)_2 + 2e;\ E^0 = -0.81\ \text{V} \qquad (1.6)$$

Advantages of this battery include longer life cycle of approximately 3500 cycles and high energy density of around 40–75 Wh kg^{-1}, which is more than lead-acid battery but lower than lithium-ion battery [11,17,18]. It has round trip efficiency of around 60–90%. The main drawback of this battery is the use of cadmium metal, which is a highly toxic heavy metal, hence disposable is not easier for this metal as compared to other batteries. This battery also suffers of memory effect problems.

1.3 Supercapacitors

Supercapacitors are also known as ultra-capacitors, which employ double-layer capacitor technology to store energy. The separation of charge takes place at electrode-electrolyte interface leading to double-layer formation. A supercapacitor is classified into two categories; electrochemical double layer capacitors (EDLC) and pseudocapacitors. In EDLC, electrical energy in the form of charge is stored in an double-layer formed at electrode-electrolyte interface [19]. A schematic of electrochemical double-layer formation taking place at interface is illustrated in Figure 1.2.

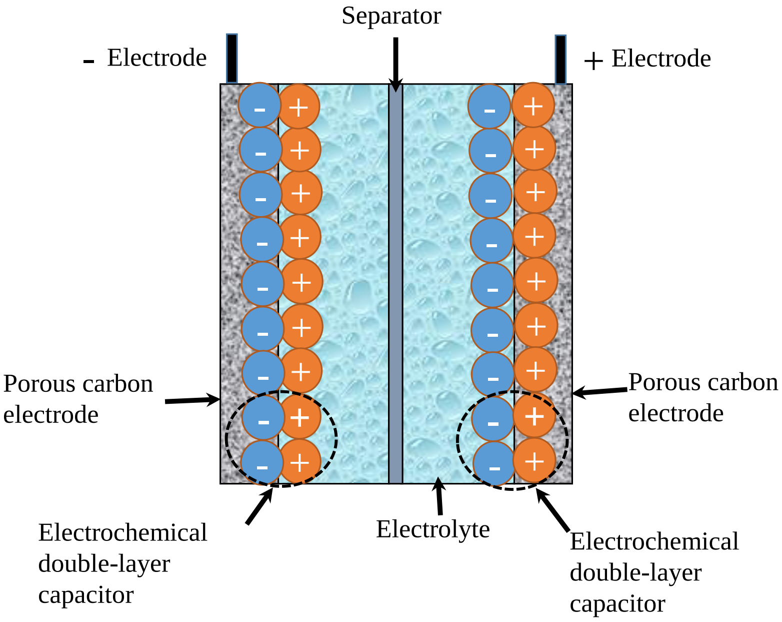

Figure 1.2. Schematic representation of charged capacitor illustrating formation of double-layer at both electrode-electrolyte interface.

Whereas in pseudocapacitor energy is stored in the form of redox couples, occurs at electrode-electrolyte interface through electrochemical reactions. A supercapacitor comprises of two activated carbon electrodes immersed in electrolyte of propylene carbonate which are separated by porous solid electrolyte such as polypropylene membrane [20,21]. The open circuit potential of the device is ~2.5 V. It attracts attention because of its several advantages over other energy storage devices such as rapid charge-discharge features, longer life cycle ranging from 100,000 to 1 million cycles, higher efficiency of over 95% and high power density of about 1500 W kg^{-1} [22,23]. But these devices have lower energy density and face very high self-discharge problems which makes them an inappropriate choice where a continuous supply of power is necessary [24]. Another disadvantage is relatively higher cost, around $100/Wh. However, their wide range of applications can be found in electric hybrid electric vehicles, portable electronics, and elevators.

In conclusion, conventional batteries are a primary choice for energy storage solutions owing to their high energy density, low self-discharge rate, and ease of portability. But these batteries have high manufacturing and maintenance cost. The battery utilizes heavy metals (Pb, Ni, Cd), which are highly toxic and difficult to recycle. Electrode material used in battery undergoes chemical changes which limits its overall performance. Moreover, overcharging of battery may lead to explosion or may catch fire, hence safety is a major concern with these batteries. Supercapacitors have very fast charge–discharge cycles, higher efficiency and longer charge-discharge cycles compared to batteries. But they are highly expensive, and have higher self-discharge rate, lower energy density and low voltage output per cell [13,15,22]. Batteries and supercapacitors are thermodynamically closed system which limits their power and energy densities. An alternative way to store energy is using flow batteries which are thermodynamically open system and are in the following sections.

1.4 Flow batteries

Flow batteries are an electrochemical energy device in which electrolytes are externally fed similar to fuel in fuel cells. A flow battery setup consists of a cell-stack, two storage tanks with electrolytes and two pumps as important components. Electrical energy is stored in liquid electrolytes in the form of chemical energy of two redox couples. The electrolytes are continuously pumped from the respective tanks to the cell-stack. The cell consists of two porous electrodes separated by an ion exchange membrane. During charging or discharging of battery, the oxidation and reduction of active species in electrolytes take place at electrode surface. There are numerous types of flow batteries are in existence such as Zn-Br, Polysulfide–Bromine, Vanadium redox flow battery, and Fe-Cr batteries.

1.4.1 Zn-Br battery (ZBB)

ZBB was first developed by Exxon Research and Engineering Corporation and successfully tested it in Austria, during year 1980 to 1990 [13]. This flow battery possesses energy density of 30–65 Wh L^{-1} [25]. It is also called a hybrid flow battery because some of the energy is stored in electrolyte and the rest is stored on anode plated with zinc metal [26]. The battery setup consists of two storage tanks in which the electrolyte solutions of zinc bromide with bromine complexing agents are present and are circulated from the storage tanks to the cell-stack with the help of pumps [27]. The cell-stack has two carbon–plastic composite electrodes separated by a microporous polyolefin membrane, which selectively allows passage of bromide and zinc ions but prevents polybromide ions and complex bromine to pass through. The schematic of battery is shown in Figure 1.3.

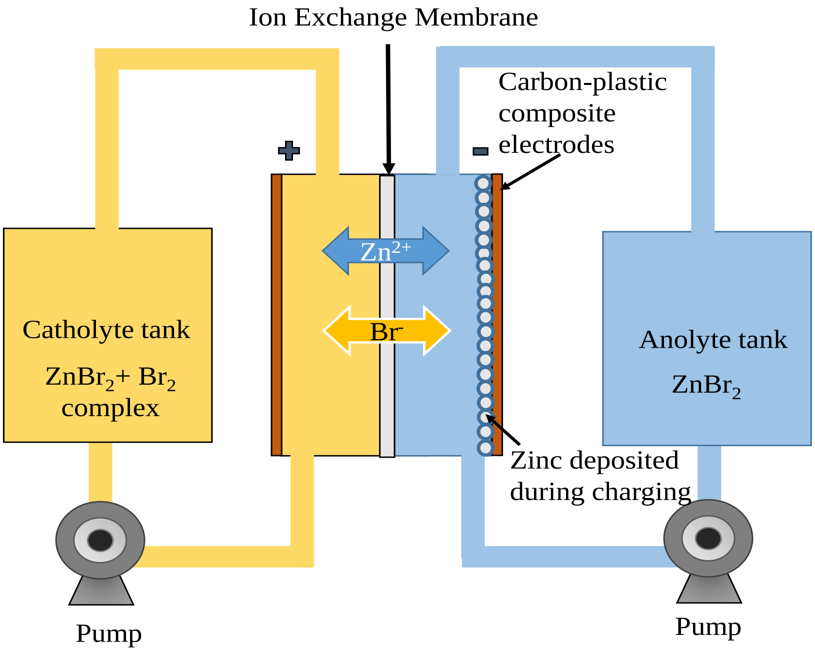

Figure 1.3. Schematic of a Zn-Br battery.

The electrode reactions taking place at the positive and negative electrode during discharging and charging are:

Positive electrode:

$$Br_2(complex) + 2e \underset{\text{Charging}}{\overset{\text{Discharging}}{\rightleftarrows}} 2Br^-;\ E^0 = 1.08\ \text{V} \tag{1.7}$$

Negative electrode:

$$Zn \underset{\text{Charging}}{\overset{\text{Discharging}}{\rightleftarrows}} Zn^{2+} + 2e;\ E^0 = -0.76\ \text{V} \tag{1.8}$$

During discharging, bromine complex converts into bromide ions at the positive electrode, and the reverse reaction takes place during charging. The formation of bromine gas is mitigated by using complexing agents because it is dangerous for health [28]. At the negative electrode, zinc plated over carbon–plastic composite electrodes oxidizes to form Zn^{2+}. The cell generates potential of 1.84 V and its overall efficiency is ~75% [13]. This flow battery is widely used in applications towards micro grids, UPS, and power quality managements. Major advantages of Zn-Br battery are its good reversibility, higher cell potential and deep discharge capability [29]. Drawbacks include corrosive nature of bromine, dendrite formation on Zn electrodes while charging, high self-discharge rates, short life cycle and low energy efficiency, which limit its use [30].

1.4.2 Polysulfide-Bromine battery (PSB)

This battery was first developed by Regenesys Technologies Limited [31]. It is a type of hybrid flow battery. The battery has energy density of 20–30 Wh L^{-1} which is lower than a ZBB battery. It has efficiency 75% [28,29]. The battery utilizes sodium bromide ($NaBr$) and sodium polysulfide (Na_2S_x) as positive electrolyte and negative electrolyte, respectively. Nickel foam, sulfide nickel, carbon felt, a carbon cloth are used as electrode materials, and proton exchange membrane (Nafion) is used as a separator. During charging, bromide ions oxidize to form tribromide ions at positive electrode, while at negative electrode, polysulfide ions reduce to sulfide ions. Reactions occurring during discharging and charging of a PSB battery are as follows:

Positive electrode:

$$Br_3^- + 2e \underset{\text{Charging}}{\overset{\text{Discharging}}{\rightleftarrows}} 3Br^-;\ E^0 = 1.09 \text{ V} \tag{1.9}$$

Negative electrode:

$$2S_2^{2-} \underset{\text{Charging}}{\overset{\text{Discharging}}{\rightleftarrows}} S_4^{2-} + 2e;\ E^0 = -0.26 \text{ V} \tag{1.10}$$

The battery generates a cell voltage of ~1.50 V [28]. It is widely used for frequency and voltage control, and for power backup applications because of its fast response time under 20 ms. Other advantage of this battery is the use of electrolyte materials which are found in abundance, has high solubility in aqueous electrolytes, and has low cost. Disadvantages include the use of bromine, which is strongly corrosive in nature, and formation of sodium sulfate crystals, which lead to environmental problems. Additionally, the crossover and mixing of electrolytes may cause precipitation of sulfur species and formation of toxic gases such as hydrogen sulfide (H_2S) and Br_2 [32].

1.4.3 Vanadium redox flow battery (VRFB)

This battery was first proposed by Skyllas-Kazacos and co-workers in 1980s at the University of New South Wales, in Sydney, Australia. This flow battery transforms chemical energy into electrical energy by interconversion of different oxidation states of vanadium. Unlike ZBB and PSB, VRFB uses electrolyte solutions of vanadium salts on both positive and negative side of the battery which eliminates the chance of cross-contamination. The electrolyte solution used in this battery is prepared by dissolving $VOSO_4$ in H_2SO_4. It employs V(V)/V(IV) as positive and V(III)/V(II) as negative electrolytes. These electrolytes are supplied from tanks to the cell with the help of two pumps. The cell consists of two electrodes using carbon felt, carbon cloth or carbon paper separated by a proton exchange membrane such as Nafion. The schematic of a VRFB is shown in Figure 1.4.

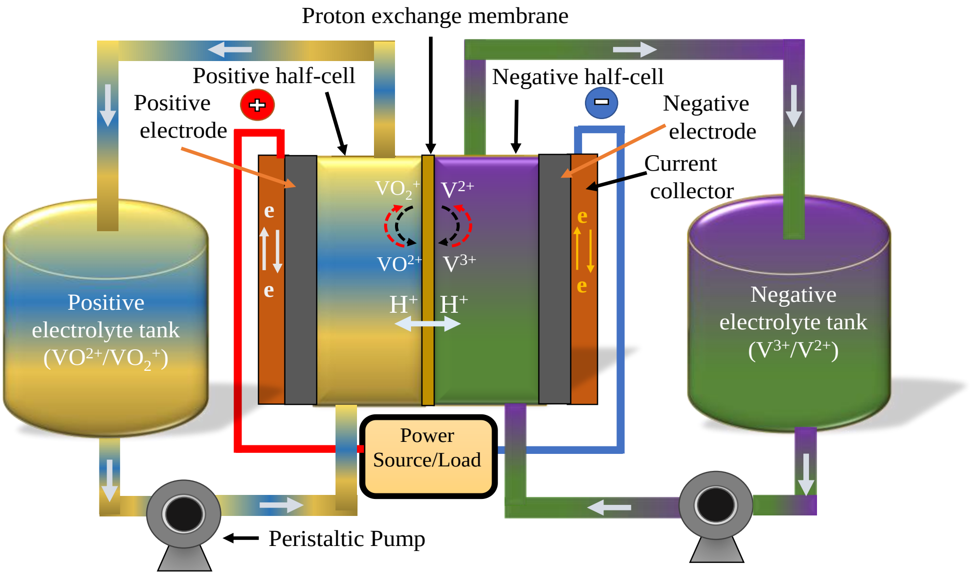

Figure 1.4. Schematic of a VRFB.

The membrane prevents from mixing of positive and negative half-cell electrolytes. During discharging *V*(V) reduces to *V*(IV) at positive electrode and *V*(II) oxidizes to *V*(III) at negative electrode. During charging, the opposite reactions occur. The corresponding reactions are:

Positive electrode:

$$VO_2^+ + 2H^+ + e \underset{\text{Charging}}{\overset{\text{Discharging}}{\rightleftarrows}} VO^{2+} + H_2O;\ E^0_{positive} = 1.00\text{ V} \tag{1.11}$$

Negative electrode:

$$V^{2+} \underset{\text{Charging}}{\overset{\text{Discharging}}{\rightleftarrows}} V^{3+} + e;\ E^0_{negative} = -0.26\text{ V} \tag{1.12}$$

Overall reaction:

$$VO_2^+ + 2H^+ + V^{2+} \underset{\text{Charging}}{\overset{\text{Discharging}}{\rightleftarrows}} VO^{2+} + H_2O + V^{3+};\ E^0_{cell} = 1.26\text{ V} \tag{1.13}$$

where $E^0_{positive}$ and $E^0_{negative}$ are the standard reduction potentials at positive and negative side, respectively, and E^0_{cell} is the overall cell potential. During discharging and charging process, it requires exchange of protons between two electrodes which is facilitated by the membrane. The membrane also prevents vanadium ions to pass through preventing mixing of electrolytes. This battery offers flexibility of independently scaling up its capacity and power. Its capacity can be increased or decreased by changing volume of electrolyte in tanks, whereas its power can be varied by the size and geometry of cell-stack. The VRFB generates cell potential in the range of 1.4–1.6 V, depending on concentration of vanadium in electrolyte solution.

1.4.4 Comparison of VRFB with other flow batteries

VRFB batteries have a lifetime of ~ 20 years with total number of ~15000 charge-discharge cycles at 100% depth of discharge [9]. The battery possesses higher efficiency of nearly 85%, low self-discharge, and high depth of discharge [10,15,22]. Unlike Fe-Cr and ZBB, and PSB batteries, VRFB utilizes same vanadium as both positive and negative electrolyte solutions resulting free from cross-contamination problems. Comparison of different technical features of VRFB with different redox flow batteries is also given in Table 1.1.

Table 1.1. Comparison of VRFB with other flow batteries in terms of their technical features [28,33,34].

Type of flow batteries/ Technical features	VRFB	PSB	ZBB
Energy density	20 – 30 Wh L^{-1}	20 – 30 Wh L^{-1}	30 – 65 Wh L^{-1}
Daily self-discharge	Very less	Small	Small
Overall cell potential	1.4 – 1.6 V	1.5 V	~1.8 V
Net Efficiency	85%	75%	70 – 75 %
Discharge time	24 h +	4–12 h	~2–5 h
Cycle life	>15000	~2000	~2000
Life time	20 years	10 – 15 years	5 – 10 years
Specific power	~166 W kg^{-1}	-	~100 W kg^{-1}

Vanadium electrolyte does not deteriorate for many years hence replacement cost of electrolyte will be less compared to other flow batteries. The main drawback of the battery is its lower energy density of 20 – 30 Wh L^{-1} [35]. This battery is useful in the applications of load leveling in power stations, electric grids attached with wind and solar energy, power backup such as UPS applications. In contrast to other flow batteries, VRFB can be easily recharged by replacing the discharged electrolyte from fresh electrolyte solution.

1.5 Terminologies used for batteries

1.5.1 Energy density and power density

Energy density is the amount of energy that is stored per unit mass or volume of the storage device and can be expressed as:

$$\text{Energy density} = \frac{\text{Voltage (V)} \times \text{Capacity (Ah)}}{\text{Volume (L)}} = \text{Wh L}^{-1} \tag{1.14}$$

A battery can store energy per litre volume of electrolyte for a specified rate of discharge [22]. Energy density of VRFB is mainly related to the total amount of active species and may change according to the types of energy storage devices. Power density is defined as power output per unit volume or mass, mathematically it is written as:

$$\text{Power density} = \frac{\text{Voltage (V)} \times \text{Current (A)}}{\text{Volume (L)}} = \text{W L}^{-1} \tag{1.15}$$

Power density of VRFB depends on area of the cell and number of cells used in the stack.

1.5.2 Capacity

The theoretical capacity of the battery is defined as the amount of charge stored in the battery. It is expressed in Coulomb or Ampere-hour. The capacity of VRFB depends on the concentration and volume of electrolyte solution and is expressed by Faraday’s law:

$$Q_{th} = xnF, \tag{1.16}$$

where Q_{th} is the theoretical capacity, x is the number of moles of vanadium ions involved in the reaction, n is the number of electrons transferred during the reaction, and F is the Faraday's constant (96485 C/mol.). In practice, 100% conversion of all vanadium ions is not possible during the charge and discharge process [36]. Thus the actual capacity of the battery is always lower than the theoretical capacity. There is always some amount of vanadium ions are unavailable or unapproachable for reactions at the electrode surface at the end of charge and discharge processes. The actual charge storage capacity varies between 60% of the theoretical value, and it is given by [37]:

$$Q_a = it, \tag{1.17}$$

where, Q_a the actual charge stored in battery, i is charge or discharge current in Ampere, and t is the time elapsed in hours.

1.5.3 Capacity fade

Capacity fade or capacity loss is a common phenomenon occurring in a rechargeable battery. With repeated use (charge-discharge cycles), the amount of charge a battery can hold decreases with time which is termed as capacity fade. Lesser is the loss in capacity, longer will be the lifespan of the device. In VRFB, it arises due to loss of vanadium ions diffusing through membrane [38,39].

1.5.4 Roundtrip efficiency

The round trip efficiency of the battery is calculated as the amount of energy consumed of the total energy input. It measures the energy lost during one charge/discharge cycle. The reported round trip efficiency of VRFB ranging 85–90% [5,40].

1.5.5 Lifetime and cycle life

Lifetime evaluation is one the important parameters of any storage device and it is defined as the time before it is replaced. The lifetime of VRFB can be up to approximately 20 years. Because of the non-degradation property of vanadium electrolytes with time, it can be further recycled and reused. The cycle life is defined as a number of times a battery can be charged and discharged, before losing its performance below a limit. When the capacity of the battery falls below 80%, its cycle life is considered finished [22]. Typically, it has approximately 15,000 charge-discharge cycles at 100% depth of discharge [15]. The depth of discharge is defined in Subsection 1.5.7.

1.5.6 Self-discharge

After complete charging, the battery discharges on its own without being used. The self-discharge in VRFB is very low, 0.1–0.4 % per day [41]. Self-discharge occur in VRFB is due to crossover of vanadium ions through the membrane from one half-cell to another one [42]. Another reason of it is the pumps consumes power from the battery [43].

1.5.7 Depth of discharge

Depth of discharge is defined as fraction or percentage of energy removed from the fully charged battery. A 100% depth of discharge is achieved when total energy of a charged battery is drained out. The full depth of discharge in VRFB can be reached up to 100%, whereas in lead-acid and lithium-ion battery, it is 50–80% [44].

1.5.8 Energy efficiency

Energy efficiency is the measure of amount of energy released during discharge to the amount of energy needed to charge the battery. The energy efficiency of VRFB is about 70-85% which is almost equal to lead-acid battery but lower than the Li-ion battery.

1.5.9 Open circuit potential (OCP) and state of charge (SOC)

Open circuit potential (OCP) or equilibrium potential is a measure of potential between the two terminals of the cell when no current flows through it. The equilibrium potential of the cell, E, can be determined from the following thermodynamics relation:

$$\Delta G = -nFE\,, \tag{1.18}$$

where ΔG is the Gibb's free energy change of an electrochemical reaction, n is the number of electrons transferred during reaction, and F is the Faraday's constant. For spontaneous reaction, ΔG is negative and E is positive. Consider an elementary reaction:

$$wA + xB \rightarrow yC + zD \tag{1.19}$$

The ΔG for the reaction can be written as,

$$\Delta G = \Delta G^0 + RT \ln Q\,, \tag{1.20}$$

with

$$Q = \text{Reaction quotient} = \frac{a_C{}^y a_D{}^z}{a_A{}^w a_B{}^x}\,,$$

where, a_i is the activity of species and $w, x, y,$ *and* z are the stoichiometric coefficients, ΔG^0 is the Gibb's free energy change at standard temperature (25°C) and pressure (1 atm), R is the universal gas constant (8.314 Joule/mol. K), and T is the temperature (K). Equation (1.20) can be rewritten, using Equation (1.18), as:

$$-nFE = -nFE^0 + RT \ln Q\,, \tag{1.21}$$

where E^0 is the standard cell potential, i.e. $\Delta G^0 = -nFE^0$. After rearranging the Equation (1.21), it gives the Nernst equation, which relates the cell potential to its standard value and reaction quotient,

$$E = E^0 - \frac{RT}{nF} \ln Q \tag{1.22}$$

For a cell, E or (E^0) is written as combination of potentials of two half-cells, i.e.

$$E = E_{cathode} - E_{anode}\,, \tag{1.23}$$

where $E_{cathode}$ is the reduction potential of cathodic half-cell, and E_{anode} is the reduction potential of anodic half-cell.

Consider an example of a galvanic cell, provided in Figure. 1.5, which has half-cells comprised of *Zn* and *Cu* electrodes immersed in their respective salt solutions of $ZnSO_4$ and $CuSO_4$ solutions, and placed separately in two tanks.

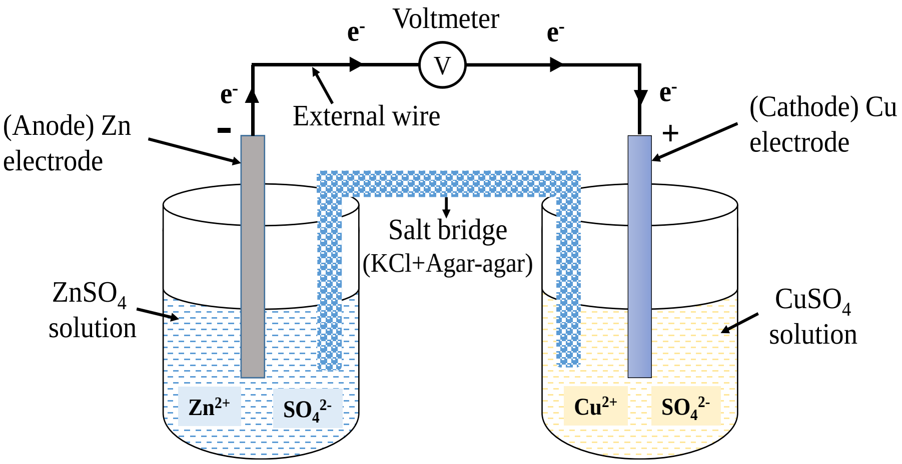

Figure 1.5. A schematic of galvanic cell.

A salt bridge filled with *KCl* and agar-agar solution is used to electrically connect these two half-cells. It balances the charge by facilitating the flow of ions through it. Since *Zn* electrode has more tendency to lose electrons than *Cu* electrode, the former forms anodic half-cell, and the latter forms cathodic half-cell. The oxidation and reduction reactions of both half-cells are:

$$\text{Anode: } Zn(s) \rightarrow Zn^{2+}(aq) + 2e;\ E^0_{Zn^{2+}/Zn} = -0.76 \text{ V} \tag{1.24}$$

$$\text{Cathode: } Cu^{2+}(aq) + 2e \rightarrow Cu(s);\ E^0_{Cu^{2+}/Cu} = +0.34 \text{ V} \tag{1.25}$$

$$\text{Overall reaction: } Zn(s) + Cu^{2+}(aq) \rightarrow Zn^{2+}(aq) + Cu(s);\ E^0_{cell} = 1.10 \text{ V} \tag{1.26}$$

The Nernst equations for Equation (1.24) can be written with the help of Equation (1.21) as:

$$E_{(Zn/Zn^{2+})} = E^0_{(Zn/Zn^{2+})} - \frac{RT}{2F}\ln a_{Zn^{2+}}(aq) \tag{1.27}$$

where $E_{(Zn/Zn^{2+})}$ is oxidation potential, which can be converted to reduction potential by: $E_{(Zn/Zn^{2+})} = -E_{(Zn/Zn^{2+})}$ Thus,

$$E_{(Zn^{2+}/Zn)} = E^0_{(Zn^{2+}/Zn)} - \frac{RT}{2F}\ln\frac{1}{a_{Zn^{2+}}} \tag{1.28}$$

Similarly for cathodic reaction,

$$E_{(Cu^{2+}/Cu)} = E^0_{(Cu^{2+}/Cu)} - \frac{RT}{2F}\ln\frac{1}{a_{Cu^{2+}}} \tag{1.29}$$

And for overall reaction,

$$E_{cell} = E^0_{(Cu^{2+}/Cu)} - E^0_{(Zn^{2+}/Zn)} = E^0 - \frac{RT}{nF}\ln\frac{a_{Zn^{2+}}}{a_{Cu^{2+}}} \tag{1.30}$$

where $E^0 = E^0_{(Cu^{2+}/Cu)} - E^0_{(Zn^{2+}/Zn)} = 1.10\ \text{V}$. Activity, a_i, and concentration, c_i, of a species, i, in concentrated solution are related by following relation [37]:

$$a_i = \gamma_i c_i \tag{1.31}$$

where γ_i is a activity coefficient of a species, i, which varies with the concentration of solution. For dilute solution, $\gamma \approx 1$. Thus, the Equation (1.30) can be written in terms of activity coefficient as:

$$E_{cell} = E^0 - \frac{RT}{2F}\ln\left(\frac{c_{Zn^{2+}}\gamma_{Zn^{2+}}}{c_{Cu^{2+}}\gamma_{Cu^{2+}}}\right) \tag{1.32}$$

After rearranging the Equation (1.32) is:

$$E_{cell} = E^{0'} - \frac{RT}{2F}\ln\left(\frac{c_{Zn^{2+}}}{c_{Cu^{2+}}}\right) \qquad (1.33)$$

where $E^{0'}$ = Standard formal potential = $E^{0} - \frac{RT}{2F}\ln\left(\frac{\gamma_{Zn^{2+}}}{\gamma_{Cu^{2+}}}\right)$

Employing above derivation, open circuit potential of VRFB can be estimated. The electrode reactions occurring at positive and negative side in VRFB are given in the Section (1.4.3) and are presented here for better illustration:

$$\text{Positive electrode}: VO_2^+ + 2H^+ + e \underset{\text{Charging}}{\overset{\text{Discharging}}{\rightleftarrows}} VO^{2+} + H_2O;\ E^0_{positive} = 1.0\ \text{V} \qquad (1.11)$$

$$\text{Negative electrode}: V^{2+} \underset{\text{Charging}}{\overset{\text{Discharging}}{\rightleftarrows}} V^{3+} + e;\ E^0_{negative} = -0.26\ \text{V} \qquad (1.12)$$

By following the Equations (1.22) and (1.31), the electrode potential at positive side, $E_{positive}$ is:

$$E_{positive} = E^0_{positive} - \frac{RT}{F}\ln\left(\frac{c_{VO^{2+}}c_{H_2O}}{c_{VO_2^+}c^2_{H^+}}\right) - \frac{RT}{F}\ln\left(\frac{\gamma_{VO^{2+}}\gamma_{H_2O}}{\gamma_{VO_2^+}\gamma^2_{H^+}}\right) \qquad (1.34)$$

where $E^0_{positive}$ is the standard reduction potential of the positive half-cell. Solutions are made in water, and concentration of acid is higher than that of vanadium ion, concentration of H_2O and H^+ can be assumed constant. Thus, Equation (1.34) reduces to:

$$E_{positive} = E^{0'}_{positive} - \frac{RT}{F}\ln\left(\frac{c_{VO^{2+}}}{c_{VO_2^+}}\right) \qquad (1.35)$$

with

$$E^{0'}_{positive} = E^0_{positive} - \frac{RT}{F}\ln\left(\frac{\gamma_{VO^{2+}}\gamma_{H_2O}}{\gamma_{VO_2^+}\gamma^2_{H^+}}\right) - \frac{RT}{F}\ln\left(\frac{c_{H_2O}}{c^2_{H^+}}\right)$$

where $E^{0'}_{positive}$ is the formal potential of positive half-cell. Similarly for negative half-cell,

$$E_{negative} = E_{negative}^{0'} - \frac{RT}{F}\ln\left(\frac{c_{V^{2+}}}{c_{V^{3+}}}\right), \tag{1.36}$$

with

$$E_{negative}^{0'} = E_{negative}^{0} - \frac{RT}{F}\ln\left(\frac{\gamma_{V^{2+}}}{\gamma_{V^{3+}}}\right)$$

where $E_{negative}^{0'}$ is the formal potential of negative half-cell. Thus, the cell potential of a VRFB can be written as:

$$E_{cell} = E_{cell}^{0'} - \frac{RT}{F}\ln\left(\frac{c_{VO_2^+}c_{V^{2+}}}{c_{VO^{2+}}c_{V^{3+}}}\right) \tag{1.37}$$

where $E_{cell}^{0'}$ = formal cell potential = $E_{positive}^{0} - E_{negative}^{0}$. The concentration of vanadium ions at positive and negative side can be related to the state of charge (SOC) as [45]:

$$c_{VO_2{}^+} = c_{V^{2+}} = c_V.SOC \tag{1.38}$$

$$c_{VO^{2+}} = c_{V^{3+}} = c_V.(1-SOC) \tag{1.39}$$

where c_v is the total concentration of vanadium and *SOC* is state of charge (%). The SOC indicates the status of the battery at a given charge or discharge state. Generally a VRFB is operated between SOC values: 20 and 80% [36]. Employing Equations (1.38) and (1.39) in Equation (1.37) leads to:

$$E_{cell} = E_{cell}^{0'} - \frac{RT}{F}\ln\left[\frac{(SOC)^2}{(1-SOC)^2}\right] \tag{1.40}$$

1.6 Components of VRFB

1.6.1 Electrodes

Electrode is the heart of any electrochemical devices where anodic and cathodic reactions occur. During reactions in a VRFB, it helps in the exchange of electrons with electrolytes containing vanadium ions. It does not directly participate in the electrochemical reaction itself but provides reaction sites to the vanadium ions [1,46].

An electrode for a VRFB requires following properties:

a. Hydrophilic in nature to provide intimate contact with aqueous electrolytes [47].
b. Porous material which provides higher surface area for reactions.
c. Providing reaction sites for conversion of V(II) ↔ V(III) and V(IV) ↔ V(V).
d. Electron conductive in nature to facilitate transport of electrons to current collectors.

Extensive research has been carried out to explore the suitable materials for electrodes, including, carbon and non-carbon materials. Of all, carbon materials emerged as the most suitable for employing in VRFB, and numerous studies have been performed to analyze its applications. The carbon electrodes are highly porous which provide homogenous reaction sites for the electrochemical conversion of vanadium ions. They are of low cost and light weight, possess three-dimensional network, are non-corrosive towards acids, and have very high electronic conductivity [48]. Commercial VRFBs employ carbon felt electrodes made from rayon or polyacrylonitrile material. The felt is chemically and thermally treated to increase the number of reaction sites at its surface and to increase its crystallinity and conductivity [30]. The carbon felt electrodes are capable to operate at a wide range of potentials and are used on both positive and negative sides of the cell. Notwithstanding these properties also have limitations including side reactions such as oxygen and hydrogen evolution reactions occurring at positive and negative electrodes. Carbon felt has limited wettability in aqueous electrolytes due its hydrophobic nature. The performance of the cell hampers due to this and leads to incomplete utilization of electrode. Therefore, treatment of electrodes is required to achieve their hydrophilic nature and enhanced utilization.

1.6.2 Membrane

Membrane is one of the indispensable component of VRFBs. It helps in exchanging the protons between two electrodes and also helps to physically separate the two half-cells [46]. Thus, the membrane prevents the mixing of positive and negative electrolyte solutions, it allows only protons to pass through and inhibits vanadium species [49]. The Nafion® by DuPonts widely used as a separator in VRFB [30]. It is a class of perfluorosulfonic acid polymer, which possess excellent proton conductivity, higher chemical stability, and good mechanical strength.

1.6.3 Electrolyte

Electrolyte is a key component of VRFB. Electrolyte solution consists of vanadium salt as active species dissolved in supporting electrolyte such as H_2SO_4 [1]. $VOSO_4$ and V_2O_5 salts are commonly used to prepare the starting electrolyte solution, but $VOSO_4$ is preferred because its solubility in acidic medium is 10 times higher than V_2O_5 [50,51]. Vanadium element has an electronic configuration of $3d^3$ $4S^2$. Its salts exist in four different oxidation state identified by characteristic colors in solutions V(II) (violet), V(III) (green), V(IV) (blue), and V(V) (yellow). The solubility of a vanadium salt strongly depends on its concentration in supporting electrolyte solution. The maximum concentration of vanadium up to 2 M in 2 M H_2SO_4 solution is used over wide range of temperatures in electrolytes [52–54]. The most air stable oxidation state of vanadium is V(IV) [36]. If present in aqueous acidic solution and exists as hydrated vanadyl ion (VO^{2+}), i.e. $[VO(H_2O)_5]^{2+}$. The V(II) is present as $[V(H_2O)_6]^{2+}$, which is the least stable oxidation state and easily oxidizes to form V^{3+} [55,56]. The V^{5+} ion is stable in presence of air [36,46]. The solubility of ions is also temperature dependent, their solubility limit ranging from 10 – 40 °C [57].

Acidic supporting electrolyte is frequently used in VRFB which helps to dissolve active species of vanadium ions. Roles and properties of supporting electrolyte are:

- It provides H^+ ions to maintain good electrical conductivity in the electrolyte solution. It also helps to decrease the solution resistance [2].
- Increasing the concentration of supporting electrolyte lessen the effect of migration. The most commonly used supporting electrolyte is sulfuric acid, H_2SO_4.
- The concentration of supporting electrolyte must be higher than the concentration of active species for dissolving it in the solution.
- Supporting electrolyte must be chemically inert and it has tendency to dissolve active species in the electrolyte solution [58].
- It must be highly soluble in the solvent.

1.6.4 Current collectors

Current collectors in VRFB are used to apply or withdraw current during charging and discharging process. During charging, the current supplied from external power source is received by current collectors and transferred to the electrodes for the electrochemical conversion of vanadium ions. During discharging, the current generated through electrochemical reactions reaches to the current collector plates, which is used by external load resistance. Thus the direction of the current flow depends on whether the system is in charging or discharging mode. The materials for current collectors in VRFB must be non-corrosive towards acidic environment and possess good electrical conductivity.

Commonly used current collectors are made of carbon/graphite, Au, Cu or Pt [5,59–62].

1.6.5 Flow channel plates

The flow channel plates are one of the most important parts of VRFB, which helps to distribute electrolyte in porous electrodes. Essential properties of the plate include: electron conductivity due to which it generated electrons at electrode to pass to current collectors, and mechanical support for porous electrodes and membrane. It has engraved flow paths. A schematic of serpentine flow path on a plate is shown in Figure 1.6.

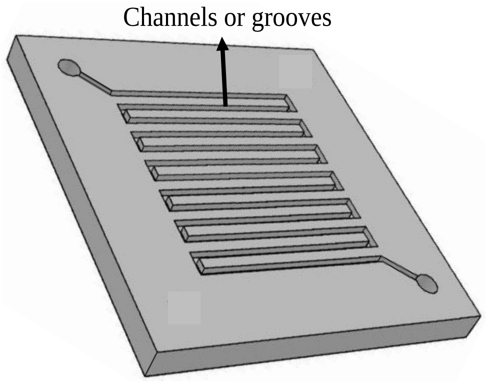

Figure 1.6. Schematic of flow channel plate used in VRFB.

Different designs of flow channel patterns are being used to improve performance of the VRFB [63–65]. Graphite material is generally used as flow channel plate because of its excellent electrical conductive nature, good mechanical strength, and lightweight. It also has a non-corrosive property against acids. Hence, continuous flow of acidic liquid electrolytes does not deteriorate the material.

1.6.6 Pumps and pipes

Pumps are the only movable part of the VRFB and are connected to both positive and negative sides of the battery by pipes. They supply electrolytes from the storage tanks to the cell stack. Centrifugal pumps and peristaltic pumps are the perfect candidate to serve this purpose at large scale and at laboratory scale, respectively. For VRFB, pipes made of PTFE, Tygon, or Viton are generally used because of their non-corrosive and acidic resistant properties.

1.7 Performance measuring parameters of VRFB

1.7.1 Polarization curve

Polarization curve is a performance characteristic curve of the battery used to measure the performance of any electrochemical energy storage system. This provides variation of output potential of the battery at a given current density and helps in determining the sources of potential losses occurring in the battery. A polarization curve depicting the losses in different current density regions is shown in Figure 1.7. Because of potential loss, the performance of the battery deviates from ideality.

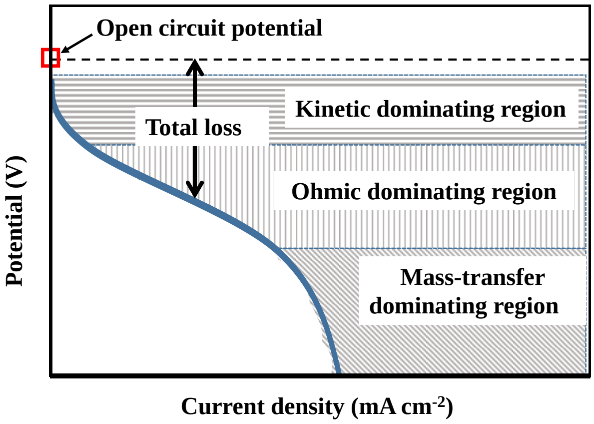

Figure 1.7. Polarization curve showing total potential loss, and kinetic, ohmic or *iR* and mass-transfer loss dominating regions in different range of current density.

The deviation stems from the cumulative effect of kinetic, ohmic (*iR*), and mass-transfer overpotentials. The figure show that losses occur in lower current density regions, and ohmic and mass-transfer losses occur in mid and high current density regions, respectively. These losses are also referred as overpotential and indicated by η. Thus the relation between cell potential in terms of open circuit potential (OCP), E_{OCP} and can be expressed as:

$$E_{cell}(j) = E_{OCP} \pm \eta_t(j) \tag{1.41}$$

$$\eta_t(j) = \eta_a(j) + \eta_{iR}(j) + \eta_{mt}(j) \tag{1.42}$$

where E_{cell}: potential of the battery at j current density, potential of the battery at zero current density, η_a: kinetic or activation overpotential, η_{iR}: ohmic overpotential, η_{mt}: mass-transfer overpotential, η_t: total overpotential during charge or discharge. Positive sign indicates that losses are additive during charging, and are accounted as potential drop from OCP during discharging, indicated by the negative sign. Thus the expression in Equations (1.41) and (1.42) state that during charging external power source applies extra potential (or overpotential) above E_{OCP} to overcome internal resistances of the battery to force j current density. During discharging, the battery expend potential, η, to provide j current density, resulting in reduced cell potential. Terminologies used in above equations are described in following subsections.

1.7.2 Kinetic overpotential

Kinetic overpotential is dominant at low current density. The overpotential stems from slow reaction kinetics. With increasing overpotential, accumulation of charges occurs on electrode and electrode-electrolyte interface, but active species do not cross the interface frequently which may lead to their electrochemical conversion. In other words, the activation energy for reaction is too high to respond to change in electrode potential. A schematic representation of energy profile at equilibrium is shown in Figure 1.8.

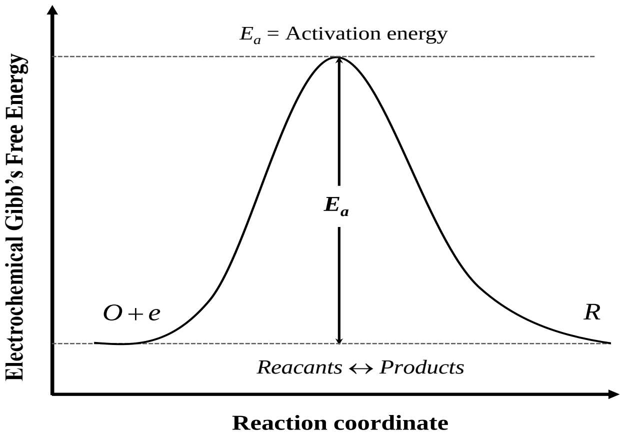

Figure 1.8. Profile of Gibb's free energy at equilibrium.

1.7.3 Butler-Volmer equation [66]

Consider single electron transfer reversible reaction:

$$O + e \leftrightarrow R \tag{1.43}$$

taking place at electrode surface in contact with the electrolyte. The schematic of the electrochemical phenomena is shown in Figure 1.9.

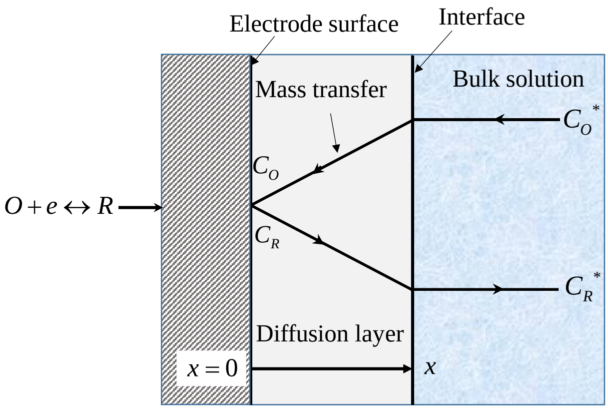

Figure 1.9. Schematic of processes occurring during electrochemical reactions.

Figure 1.9 shows three regions: (i) bulk solution, where concentrations of *O* and *R* are uniform everywhere and are C_O^* and C_R^*, respectively; (ii) diffusion layer, in which these exists concentration gradient for species *O* and *R*; (iii) electrode surface, where electrochemical reaction occur. Assume thickness of diffusion layer is *x*. The concentration of *O* and *R* at distance *x* from the surface at time t is $C_O(x,\ t) = C_O^*$ and $C_R(x,\ t) = C_R^*$, and the corresponding concentrations at surface are $C_O(0,\ t)$ and $C_R(0,\ t)$. Since the forward reaction is reduction reaction, a reduction current or cathodic current, i_c, flows. Rate of forward reaction, υ_f, is linked with i_c by Faraday's law:

$$\upsilon_f = k_f C_O(0,\ t) = \frac{i_c}{nFA}, \tag{1.44}$$

where k_f is a forward reaction rate constant, *A* is the area of electrode, and *n* is number of electrons involved in the reaction which is equal to 1 in this case. Similarly, for the backward reaction, the reaction rate and oxidation current or anodic current, i_a, can be related as:

$$\upsilon_b = k_b C_R(0,\ t) = \frac{i_a}{nFA}, \tag{1.45}$$

where k_b is a backward reaction rate constant. Thus, the net reaction rate is related by net current, i, as:

$$\upsilon_{net} = \upsilon_f - \upsilon_b = k_f C_O(0,\ t) - k_b C_R(0,\ t) = \frac{i}{nFA} \tag{1.46}$$

$$i = i_c - i_a = nFA\left[k_f C_O(0,\ t) - k_b C_R(0,\ t)\right] \tag{1.47}$$

At equilibrium, $\upsilon_{net} = 0 \Rightarrow i = 0$ and $C_O(0,\ t) = C_O^*$, $C_R(0,\ t) = C_R^*$. Assume that initially, $C_O^* = C_R^*$ and thus electrode is at equilibrium potential, $E^{0'}$. The free energy along with change in activation energy by applying potential E, away from $E^{0'}$, is shown in Figure 1.10.

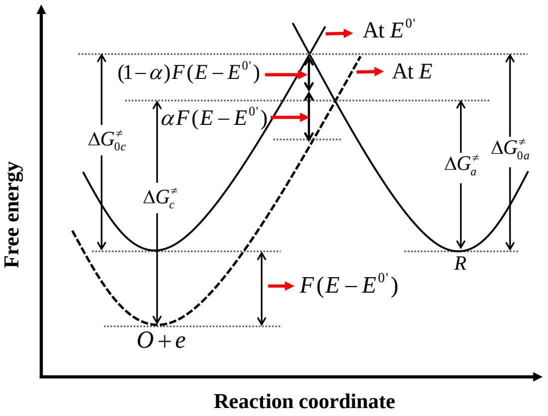

Figure 1.10. Change in electrochemical free energy for $O + e \leftrightarrow R$ with change in electrode potential from $E^{0'}$ to E. Change in free energy of 1 mol of electrons is: $-F(E-E^{0'})$. $\Delta G_c^{\neq}$ and $\Delta G_a^{\neq}$ are the cathodic and anodic activation energy barriers, respectively, at applied potential, E; $\Delta G_{0c}^{\neq}$ and $\Delta G_{0a}^{\neq}$ are the cathodic and anodic activation energy barriers, respectively, at $E^{0'}$; and α is a charge-transfer coefficient.

If electrode potential is changed to *E*, the equilibrium shifts due to change in energy of electrons, and reaction in Equation (1.43) proceeds. The solid lines in figure represent change in free energy along with reaction coordinate. At potential $E^{0'}$ at dotted line represents to potential, *E*. By applying potential, *E*, the energy of electrons changes by $F(E-E^{0'})$. Thus, the free energy of *O* + *e* shifts by that amount denoted by dotted line. Nomenclature of the parameters mentioned in the figure is as follows:

$\Delta G_{0c}^{\neq}$ = Cathodic activation energy barrier at electrode potential, $E^{0'}$.

$\Delta G_{0a}^{\neq}$ = Anodic activation energy barrier at electrode potential, $E^{0'}$.

$\Delta G_{c}^{\neq}$ = Cathodic activation energy barrier at electrode potential, *E*.

$\Delta G_{a}^{\neq}$ = Anodic activation energy barrier at electrode potential, *E*.

α = Charge-transfer coefficient. Its value lies between 0 to 1.

The activation energy barriers mentioned above can be related as:

$$\Delta G_{c}^{\neq} = \Delta G_{0c}^{\neq} + \alpha F(E-E^{0'}) \qquad (1.48)$$

$$\Delta G_{a}^{\neq} = \Delta G_{0a}^{\neq} - (1-\alpha)F(E-E^{0'}) \qquad (1.49)$$

Thus, the Arrhenius expression for reaction rate constants for forward and backward reactions are:

$$k_f = A_f e^{-\Delta G_{c}^{\neq}/RT} \qquad (1.50)$$

$$k_b = A_b e^{-\Delta G_{a}^{\neq}/RT} \qquad (1.51)$$

Employing expressions in Equations (1.48) and (1.49) in reaction rate constants leads to:

$$k_f = A_f e^{-\Delta G_{0c}^{\neq}/RT} e^{-\alpha F(E-E^{0'})/RT} \qquad (1.52)$$

$$k_b = A_b e^{-\Delta G_{0a}^{\neq}/RT} e^{(1-\alpha)F(E-E^{0'})/RT} \qquad (1.53)$$

For, $C_O^* = C_R^*$, $E = E^{0'}$, and $k_f = k_b = k^0 =$ standard reaction rate constant. Thus, $E^{0'}$ is the potential at which the forward and backward reaction rate constants are same and are referred as standard rate constant.

After putting the expression of k_f and k_b in Equation (1.47), it reduces to:

$$i = i_c - i_a = FAk^0\left[C_O(0,t)e^{-\alpha f(E-E^{0'})} - C_R(0,t)e^{(1-\alpha)f(E-E^{0'})}\right] \tag{1.54}$$

where $f = F/RT$ and *A* is the area of electrode. The above expression is a Butler-Volmer (B-V) formulation of single electron, electrode kinetics which is very important expression used in electrochemical studies. The above B-V equation shows the effect of overpotential applied over $E^{0'}$. To obtain a general form of the equation, $E - E^{0'}$ in Equation (1.54) can be replaced by:

$$E - E^{0'} = E - E_{eq} + E - E^{0'} = \eta + \frac{RT}{F}\ln\frac{C_O^*}{C_R^*}, \tag{1.55}$$

where $\eta = E - E_{eq}$ is the overpotential which accounts the deviation of *E* from equilibrium potential, E_{eq}. After inserting the expression of E-$E^{0'}$ in Equation (1.54), it simplifies to:

$$i = i_0\left[\frac{C_O(0,t)e^{-\alpha f\eta}}{C_O^*} - \frac{C_R(0,t)e^{(1-\alpha)f\eta}}{C_R^*}\right] \tag{1.56}$$

with

$$i_0 = FAk^0 C_O^{*(1-\alpha)} C_R^{*\alpha}, \tag{1.57}$$

where i_0 is defined as the exchange current, and is an intensive parameter. The related extensive parameter is exchange current density, j_0, and is defined as:

$$j_0 = \frac{i_0}{A} = Fk^0 C_O^{*(1-\alpha)} C_R^{*\alpha} \tag{1.58}$$

The Equation (1.56) is known as current-overpotential equation. The first term in the equation is cathodic component of total current at any overpotential, η and second is the contribution of anodic current. The exchange current, i_0 is the magnitude of anodic or cathodic current under equilibrium condition [32,37]. It reflects the intrinsic rate of electron transfer for the reactions. The lower the exchange current more sluggish is the kinetics and larger will be the overpotential to withdraw net current [67]. The standard reaction rate constant, k^0, shows the capability of kinetics. If the value of k^0 is very large, equilibrium will be attained very fast because both forward and backward reactions are very fast. A smaller value of rate constant indicating slower kinetics; equilibrium will be reached very slowly. The charge-transfer coefficient, α, determine the geometry of the energy barrier and indicates whether the reaction favors the cathodic or anodic direction on an applied potential [37].

Thus, the exchange current densities at positive and negative electrodes of a VRFB can be written as:

$$i_{o,p} = Fk_p^0 C_{VO_2^+}^{*(1-\alpha_p)} C_{VO^{2+}}^{*\alpha_p} \tag{1.59}$$

$$i_{o,n} = Fk_n^0 C_{V^{3+}}^{*(1-\alpha_n)} C_{V^{2+}}^{*\alpha_n} \tag{1.60}$$

where

$i_{0,p}$ and $i_{0,n}$ = Exchange currents at positive and negative electrode,

k_p^0 and k_n^0 = Standard reaction rate constants at positive and negative electrode,

α_p and α_n = Charge-transfer coefficients of positive and negative electrode,

$C^*_{VO_2^+}$ and $C^*_{VO^{2+}}$ = Concentration of VO_2^+ and VO^{2+} in bulk solution, at positive side,

$C^*_{V^{3+}}$ and $C^*_{V^{2+}}$ = Concentration of V^{3+} and V^{2+} in bulk solution at negative side,

By following the B-V expression and Equation (1.56), the net current from a VRFB can be written as [68]:

$$i = i_{0,p}\left[\frac{C_{VO_2^+}(0,\ t)e^{-\alpha_p f\eta_p}}{C^*_{VO_2^+}} - \frac{C_{VO^{2+}}(0,\ t)e^{(1-\alpha_p)f\eta_p}}{C^*_{VO^{2+}}}\right] \tag{1.61}$$

$$i = i_{0,n}\left[\frac{C_{V^{3+}}(0,\ t)e^{-\alpha_n f\eta_n}}{C^*_{V^{3+}}} - \frac{C_{V^{2+}}(0,\ t)e^{(1-\alpha_n)f\eta_n}}{C^*_{V^{2+}}}\right] \tag{1.62}$$

where

$C_{VO_2^+}(0,\ t)$ and $C_{VO^{2+}}(0,\ t)$ = Concentrations of VO_2^+ and VO^{2+} at surface of positive electrode.

$C_{V^{3+}}(0,\ t)$ and $C_{V^{2+}}(0,\ t)$ = Concentrations of V^{3+} and V^{2+} at surface of negative electrode.

η_p and η_n = Overpotentials at positive and negative electrode.

1.7.4 Mass-transfer overpotential [66]

Mass-transfer also termed as concentration overpotential, results due to the existence of concentration gradient of reactants or products between bulk solution and at the electrode surface. The concentration gradient exists because of the slow mass-transfer rate than the reaction rate. In the B-V equation, presence of C^*_O and C^*_R reflects mass-transfer effect. The effect is also presented in Figure 1.9. Mass-transfer of species in an electrochemical process occurs by three modes: (i) Migration: involves the movement of charged particles under the influence of the electric field; (ii) Diffusion: movement of reactants or active species from bulk electrolyte to the electrode surface due to the concentration gradient;

(iii) Convection: movement of reactants to the electrode surface under the influence of bulk motion of electrolyte.

The effect of migration appears in the bulk electrolyte whereas the effect of diffusion and convection is observed near the electrode surface. Mass-transfer of an active species during the process can be expressed by Nernst-Planck equation in one dimension, along *x* axis is:

$$J_i(x) = \underbrace{-D_i \frac{\partial C_i(x)}{\partial(x)}}_{\text{Diffussion}} \underbrace{- D_i C_i \frac{z_i F}{RT} \frac{\partial \phi(x)}{\partial(x)}}_{\text{Migration}} \underbrace{+ C_i v(x)}_{\text{Convection}} \tag{1.63}$$

where

$J_i(x)$ = flux of species *i* at distance *x* from the electrode surface,

D_i = Diffusion coefficient of species *i*,

C_i = Concentration of species *i*,

$\frac{\partial C_i(x)}{\partial(x)}$ = Concentration gradient of species *i* at distance *x*,

$\frac{\partial \phi(x)}{\partial(x)}$ = Potential gradient of species *i*,

z_i and $v(x)$ = Charge on species *i*, and velocity of species *i*,

For the reduction of species *O* at the electrode surface, *O* is transferred from bulk electrolyte to the electrode surface (Figure 1.9). Its concentration in bulk electrolyte at distance *x* from the electrode surface is C_O^*, and at $x = 0$, the concentration is C_O. In presence of excess supporting electrolyte, the effect of migration of active species is insignificant. The rate of mass-transfer of *O* is the combined effect of diffusion and convection which is represented by mass-transfer coefficient as:

$$\upsilon_{mt} = m_O(C_O^* - C_O) \tag{1.64}$$

where υ_{mt} is the rate of mass-transfer of species *O*, m_O is mass-transfer coefficient. At steady state, the rate of reaction, υ_{rxn} is equal to the rate of mass-transfer, υ_{mt}, the net rate of reaction for cathodic direction using Faraday's law is expressed as:

$$\upsilon_{rxn} = i_c / nFA = \upsilon_{mt}\,, \tag{1.65}$$

where i_c is the cathodic current, combining Equation (1.64) and (1.65), the net cathodic current and mass-transfer rate relate:

$$i_c / nFA = m_O(C_O^* - C_O) \tag{1.66}$$

During reverse reaction, the net anodic current is:

$$i_a / nFA = m_O(C_R - C_R^*) \tag{1.67}$$

The highest rate of mass-transfer of *O* occurs when $C_O \rightarrow 0$, or $C_O^* >> C_O$. The value of current under these conditions is called the limiting cathodic current , $i_{l,\,c}$, and it is and expressed as:

$$i_{l,\,c} = nFAm_OC_O^* \tag{1.68}$$

Using Equations (1.66) and (1.68), the ratio of concentration reduces to:

$$\frac{C_O}{C_O^*} = 1 - \frac{i_c}{i_{l,\,c}} \tag{1.69}$$

Similarly, for anodic direction, when, $C_R \rightarrow 0$ or $C_R << C_R^*$ the current is called limiting anodic current, $i_{l,\,a}$, and ratio of concentration reduces to:

$$\frac{C_R}{C_R^*} = 1 + \frac{i_a}{i_{l,\,a}} \tag{1.70}$$

By substituting the concentration ratios, C_O/C_O^* and C_R/C_R^*, in current-overpotential Equation (1.56), and recognizing $i = i_c = -i_a$, the required expression arrives at:

$$\eta = i\,\frac{RT}{F}\left(\frac{1}{i_0} + \frac{1}{i_{l,\,c}} - \frac{1}{i_{l,\,a}}\right) \tag{1.71}$$

For small overpotential, $\alpha f \eta << 1$, employing Taylor series expansion in B-V Equation (1.56), the equation reduces to:

$$\frac{i}{i_0} = \frac{C_O(0,t)}{C_O^*} - \frac{C_R(0,t)}{C_R^*} - \frac{F\eta}{RT} \tag{1.72}$$

In terms of charge-transfer and mass-transfer resistances, the Equation (1.72) is written as:

$$\eta = -i\,(R_{ct} + R_{mt,\,c} + R_{mt,\,a}) \tag{1.73}$$

where R_{ct} is a charge-transfer resistance, $R_{mt,\,c}$ and $R_{mt,\,a}$ are the mass-transfer resistances for cathodic and anodic sides. It is clear from the above equation that if i_0 is much greater than limiting currents, $R_{ct} << R_{mt,\,c} + R_{mt,\,a}$, and the overpotential even near, E_{eq} is due to mass-transfer or concentration overpotential. In contrast with i_0 is much less than limiting currents, $R_{mt,\,c} + R_{mt,\,a} << R_{ct}$, and the overpotential even near E_{eq} is a activation or charge-transfer overpotential.

1.7.5 Ohmic or *iR* overpotential

The ohmic or *iR* loss in a VRFB originates due to several internal resistances (ionic and electronic) from its components which include current collectors, electrodes, electrolyte, membrane, and contact resistances between the cell components. A schematic diagram representing contributions of several resistances is shown in Figure 1.11.

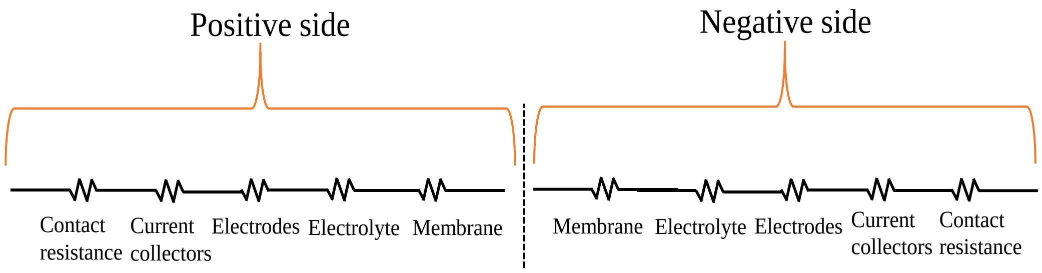

Figure 1.11. Contribution of internal resistances at positive and negative sides of the cell: current collectors, electrodes, membrane, and contact resistances between cell components.

The relation between the resultant ohmic overpotential, η_{iR} and applied current, *i* during charging or discharging is given as:

$$\eta_{iR} = \pm iR \tag{1.74}$$

where ' + ' sign is for charging and ' –' sign for discharging. It is clear from the equation that $|\eta_{iR}|$ increases with increasing current. Charging potential is higher and discharging potential is lower. If higher charging potential is applied in the cell to overcome *iR* loss, it may promote such as H_2 and O_2 evolution at negative and positive side.

Equation (1.74) states that the ohmic potential loss varies linearly with applied current. There are two major factors that influence the internal resistances of battery; electronic resistance and ionic resistance. The electronic resistance stems from resistivity of materials such as electrodes, current collectors and contact resistances between electrode and current collector, and current collector and lead from power supply. The ionic resistance stems from hindrance to movement of hydrated protons in the pores of the membrane used in the battery. Electronic conduction of a material depends on the availability of free electrons and their mobility, whereas ionic conductivity depends on concentration of free hydrated protons in the membrane and their mobility. Under normal operations, ionic resistance is higher than the electronic and contact resistances. These resistances follow ohmic law hence the name ‘ohmic resistance’.

1.7.6 Coulombic efficiency

The coulombic efficiency (CE) measures the efficiency of electrons transferred in and out of the system. It is calculated by following equation [69]:

$$CE = \frac{\int_0^{t_d} i_d dt}{\int_0^{t_c} i_c dt} \tag{1.75}$$

where i_d and i_c are discharging and charging currents, t_d and t_c are discharging and charging time. If i_d and i_c are equal and constants, the above expression will reduce to:

$$CE = \frac{t_d}{t_c} \tag{1.76}$$

From Equations (1.75) and (1.76), CE indicates the efficiency of harvesting the stored charge in the electrolyte using VRFB, and is calculated by the ratio of discharge time to the charge time. For an ideal system, efficiency should be equal to 1. For VRFB, coulombic efficiency is measured at a constant current density with a fixed range of minimum and maximum potential during discharging and charging.

1.7.7 Voltage efficiency

Voltage efficiency (VE) is the ratio of average discharging voltage to the average charging voltage. It can be calculated by the following expression [70]:

$$VE = \frac{\int_0^{t_d} V_d dt}{\int_0^{t_c} V_c dt}, \tag{1.77}$$

where V_d and V_c are discharging and charging voltages, respectively.

1.7.8 Energy efficiency

Energy efficiency (EE) is defined as the amount of energy used out of the total stored energy during the discharge-charge cycles and can be calculated as [69]:

$$EE = \frac{\int_0^{t_d} V_d i_d dt}{\int_0^{t_c} V_c i_c dt} \tag{1.78}$$

If i_d and i_c are equal and constants then Equation (1.78) will be reduce to:

$$EE = \frac{\int_0^{t_d} V_d dt}{\int_0^{t_c} V_c dt}$$

which is same as VE.

1.7.9 Electrochemical impedance spectroscopy (EIS)

EIS is an electrochemical characterization technique used to determine the losses due to kinetic, ohmic or iR, and mass-transfer resistances occurring in the cell. In the EIS technique, impedance is measured over a wide range of frequencies, where ω_c is a characteristic frequency and is presented in the form of Nyquist plot. The high frequency intercept of semicircle gives the value of ohmic resistance, R_s, which comprises of resistances of current collectors, electrodes, membrane, and contact resistances. The diameter of the semicircle gives the value of charge-transfer resistances, R_{ct}. A typical Nyquist plot is shown in Figure 1.12. The Warburg impedance, Z_w obtained at lower frequency region shows that the electrochemical reaction is controlled by diffusion process in a porous electrode. The C_{dl} value accounts for double layer capacitance. The equivalent circuit, combining all the resistances, capacitance, and impedance, is also shown in above Figure 1.12.

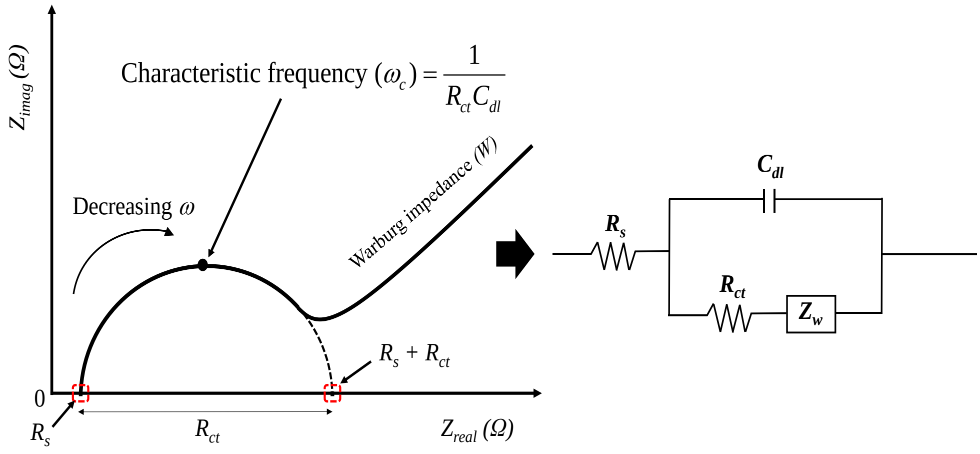

Figure 1.12. Nyquist plot and equivalent circuit diagram of a fuel cell indicating ohmic resistance, R_s; charge-transfer resistance, R_{ct}; and double layer capacitance, C_{dl}, with a Warburg impedance Z_w, which depicts the effect of mass-transfer in a porous medium, and ω_c is a characteristic frequency.

1.8 Technical challenges: performance loss due to electrolyte maldistribution

The polarization curve of an energy device shows that its performance deteriorates due to kinetic, ohmic, and mass-transfer losses, which vary with current density. Of these, kinetic and mass-transfer losses occur due to poor electrode kinetics, or due to poor distribution of electrolyte on porous electrode leading to its under utilization. As presented in Section (1.6.5) distribution of electrolyte in a VRFB is accomplished by using flow channels. The liquid electrolyte flows inside the engraved channels of plates, and it transfers to the porous electrode and distributes in the vacant spaces. The electrochemical reaction takes place at the electrode surface which provide reaction sites for the oxidation or reduction of vanadium ions [63,71]. However, the non-uniform distribution of liquid electrolyte at the electrode surface results reduced capacity and efficiency of VRFB. The electrolyte maldistribution is usually observed at its low flow rate. A schematic of flow of electrolyte inside channels attached with porous electrode is shown in Figure 1.13.

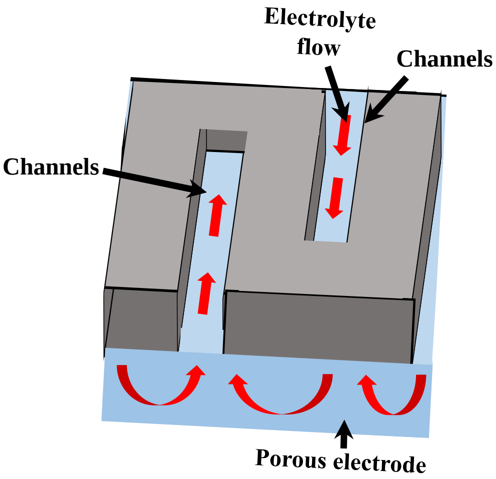

Figure 1.13. A schematic of electrolyte flow distribution from channels to the porous electrode. Red arrow indicates the direction of flow of electrolyte.

Since, the electrolyte cannot penetrate deeper to the pores of the electrode because of lower velocity, resulting most of the areas of the electrode remain unutilized. A schematic representation of non-uniform and uniform distribution of electrolyte in porous electrodes is shown in Figure 1.14. However, the uniform distribution of electrolytes can be achieved at a high flow rate but it increases the pressure drop leading to higher pumping cost [72,73]. Therefore, to address this issue one approach is the designing of

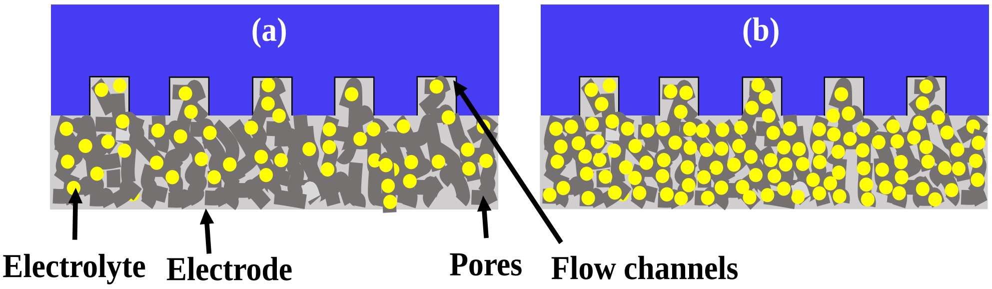

Figure 1.14. (a) Non-uniform and (b) uniform distribution of electrolyte inside the pores of electrode.

flow channels in such manner which can allow electrolyte to cover maximum surface area of electrodes at lower flow rates and at low pumping cost [74].

1.9 Motivation

1.9.1 Channels in plate type heat exchangers

Plate heat exchangers (PHEs) are type of heat exchanger which consists of metal plates with multiple channels, assembled by using gaskets (Figure 1.15). A gap is between two plates is provided for hot and cold fluids. The hot and cold fluids are spread over plates by engraved channels over them which increase the heat transfer area and induce turbulence, leading to a high heat transfer rate [75]. These heat exchangers are extensively used in food, dairy, power, nuclear reactors, and pharmaceutical industries where high heat transfer rate is desirable with a compact unit [76]. Different types of PHEs and various types of geometries of flow patterns have been reported in literatures, and some are shown in Figure 1.15 [75,77,78].

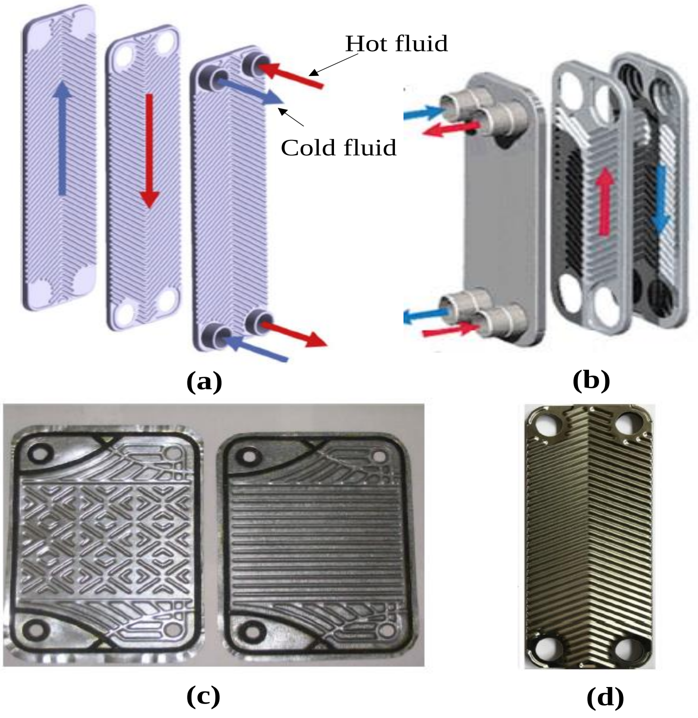

Figure 1.15. Different geometries of corrugated plates in plate heat exchangers.

The performance of a PHE is severely influenced by flow maldistribution or non-uniform distribution, causing poor heat transfer rate and higher pressure drop [79]. In several cases, non-uniform velocity distribution in channels have direct impact on hydrodynamic behavior as well as thermal performance of the system.

The problem of maldistribution in a PHE is mitigated by using following approaches:

- Designing the suitable corrugated flow patterns on plate, which provides high surface area to exchange the heat,
- Optimizing width and depth ratio of channels,
- Increasing or decreasing the number of channels engraved on plates.

1.9.2 Microchannels used in micro reactors

A micro reactor is a device in which certain chemical reactions are conducted in its microchannels (less than 1 mm) [80]. It is a powerful device to intensifying the process using micro scale processing. It offers excellent heat and mass-transfer phenomena [81]. Figure 1.16. shows engraved channels in microreactors. These reactors are used over wide range of applications like electronics, biotechnology, chemical industry, and pharmaceutical industries. The reactor helps in achieving high selectivity of product through high heat and mass-transfer rate.

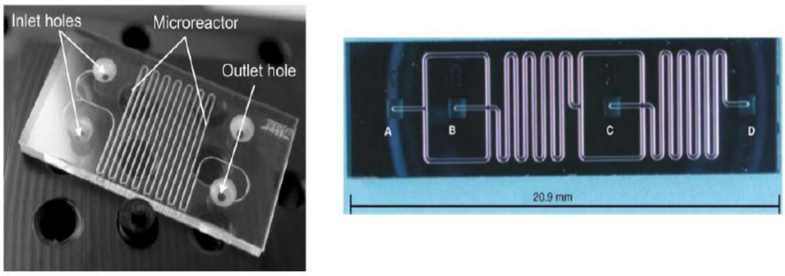

Figure 1.16. Pictures of micro channels reactors used in micro reactors for esterification reaction [81,82].

The design of flow channels for VRFB employing in this work is inspired from flow channel patterns used in PHEs and microreactors. It helps in achieving better, uniform distribution of electrolytes to the porous electrodes for the maximum utilization of porous electrodes leading to the higher electrochemical conversion of vanadium ions.

1.9.3 Objectives of current work

- Design and fabrication of different patterns of channels which would help in overcoming the maldistribution of electrolyte in porous electrodes for better utilization of electrodes.
- Performance characteristics of VRFB integrated with designed flow channels using polarization curves, and comparison with conventional channels.
- Analysis of the sources of potential losses: kinetic, ohmic (iR), and mass-transfer overpotential.
- Effect of increasing the flow rates of electrolyte on the performance of battery.
- Effect of increasing the flow rates of electrolyte on the power densities of battery.
- Determining the charge-transfer resistances and ohmic resistances using EIS technique at different flow rates of electrolyte and modeling through electrical circuit.
- Examine the effect of current densities and flow rates on discharge-charge cycles.
- Estimation of coulombic efficiency and energy efficiency of the battery.

This page is intentionally kept blank

Chapter 2: Literature review

Different types of flow channels are being used in flow based energy devices. [83–87]. Most common flow field designs that have been used in applications of commercially are serpentine, interdigitated, parallel, and spiral [71,88–91]. In some applications conventional flow field (no flow fields) designs are also used. In this design, fuel or liquid electrolyte is directly supplied to the electrode without using flow channels [63,89]. The schematic of these flow field designs are shown in Figure 2.1. The direction of electrolyte flow in flow channels are represented by the yellow and red solid arrows.

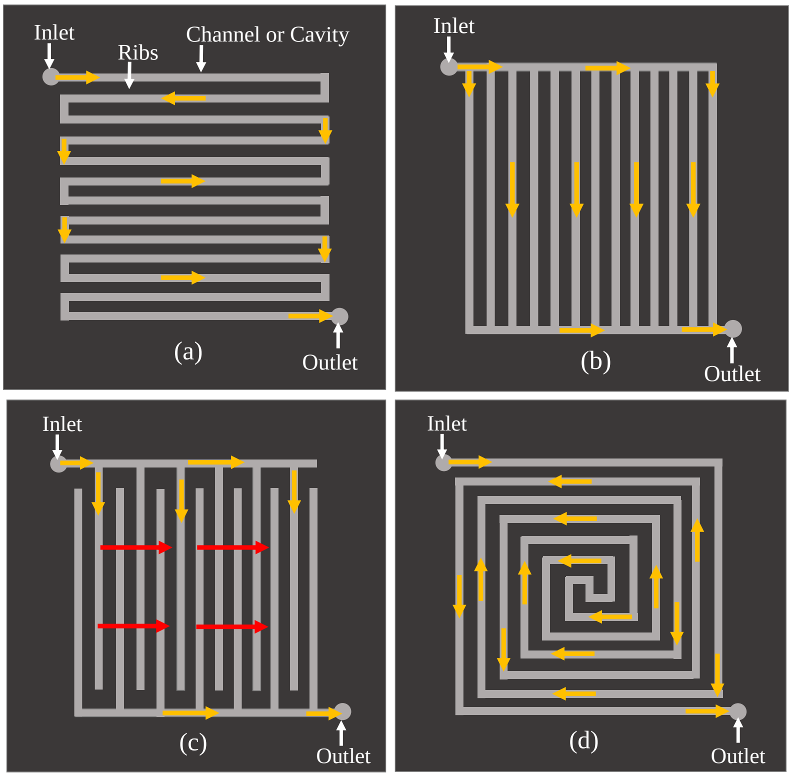

Figure 2.1. Schematic of four different flow field designs: (a) Serpentine, (b) Parallel, (c) Interdigitated, and (d) Spiral. Direction of flow of electrolyte is indicated by yellow and red color arrows.

A detailed literature review of flow channels used in energy devices is presented here:

- Maharudrayya *et al*. investigated pressure drop across parallel flow configurations for their application in planar fuel cells, and they observed that the parallel flow fields lead to severe maldistribution of fuel [92].
- Li and Sabir reviewed different flow field layouts such as pin type flow field, interdigitated, serpentine, integrated, and series-parallel flow field for the application of PEM fuel cells. They observed that the weight, cost , and volume of the fuel cell stack can be lessened significantly by improving layout configuration of flow field and using lightweight materials [83].
- Yan *et al*. numerically examined the effect of different flow field designs (conventional, parallel, and interdigitated) for the application in PEM fuel cells [90]. They also examined the effect of number of flow channels, the number of corners, channel length and baffle on the performance. PEM fuel cells coupled with interdigitated flow field show better performance than with conventional flow field which is due to the presence of baffles. At a lower consumption rate of fuel, interdigitated flow field gives similar performance to the conventional flow field, and at the optimal flow rate, the parallel flow field performed best among five flow field designs.
- Tian *et al*. studied several designs of flow fields with a multiple inlet and outlet ports, and flow paths in carbon felt aiming to reduce the pumping power and to increase the active surface area of electrodes [93]. For the laboratory application of a single electrode, they found that the pressure drop can be reduced using channels in the flow cell and electrode designs. Through numerical modeling, they showed that the pumping can be minimized by appropriate inlet and outlet ports designs and carbon felt with the flow channel. The proposed designs were applicable for single cells as well as for multiple cell stacks.

- Prasad *et al*. performed computational fluid dynamics simulation of flow in interdigitated channels to examine the effect of the channel, the header, and the electrode dimensions for the application in PEM fuel cells [94]. Their results reflect that flow is uniform across the porous electrode of lower permeabilities in between 10^{-11}– 10^{-10} m^2.
- Wang *et al*. developed two phase flow channel model, using multicomponent transport in a single channel for PEM fuel and implemented it for three dimensional numerical simulations [95]. Three critical issues are discussed for optimization of channel designs and reducing channel flooding are: liquid water buildup towards the fuel cell outlet, saturation spike in the vicinity of flow cross-sectional heterogeneity, and two-phase pressure drop.
- Tang *et al*. modelled concentration overpotential as a function of flow rate which can yield high system efficiency, along with analysis of pressure losses and pumping energy [69]. The results showed that the strategy of variable flow rate instead of constant flow rate turned out to be very effective in achieving high system efficiency, since the concentration overpotential and pumping losses are closely related to the flow rate.
- Kee and Zhu developed a model for redox flow battery applications to determine the uniformity of flow distribution and pressure drop in interdigitated flow channels, the flow was assumed to be incompressible and isothermal with constant properties [96]. The outcomes are presented in the form of dimensionless groups including fluid properties, channel geometry, porous-media configuration, properties, and operating conditions.
- Alyasiri and Park developed a 3-D model and validated with their experimental results to unearth a relationship between efficiency of the battery, employed with a

serpentine channel, with electrolyte flow rate, state of charge, current density, and channel height [89]. Results show that increasing flow rate improves the EE of the battery, and lower channel height provides better EE but at a higher pumping cost.

- Tang *et al*. modelled mass-transfer overpotential as a function of flow rate to determine the suitable variable flow rate which can produce high system efficiency besides pressure losses and total pumping energy [69]. Simulation results demonstrate that overall higher system efficiencies can be achieved with varying flow rate in comparison to the constant flow rate.
- Lee *et al*. numerically calculated the power-based efficiency of VRFB [97]. They developed a 3-D model by considering different sizes of serpentine channels and electrolyte flow rates. Their results exhibit that the performance of VRFB increases by combined effect of reducing the channel size and increasing flow rate. However, reduction of channel size and increased flow electrolyte rate increases the pressure drop at both positive and negative sides. The results show that the maximum power-based efficiency (96.6%) is obtained with a channel size of 1.9 mm at 60 mL min^{-1}, for 9.6 mm channel size it is 95.5% at 100 mL min^{-1}.
- Xu *et al*. numerically simulated the performance of three different flow field designs including serpentine, parallel, and without no flow fields, in the VRFB system [63]. They found that the pumping power varies with the selection of flow field at a given flow rates. The overpotential depends on the uniform distribution of electrolyte, in both in-plane and through-plane directions. Results indicate that there is an optimal flow rate for each flow field at which maximum efficiency is achieved. The maximum energy efficiency and round trip efficiency are achieved at the optimal flow rate in the serpentine flow field.

- Through experimental findings, Xu *et al*. compared the performance of VRFB with flow-through (without flow field) to with flow fields [73]. The results showed that the higher discharge voltage can be achieved at higher flow rates with flow fields, but at the expense of higher pressure drop. Battery with flow fields shows 5% higher energy efficiency compared to without flow fields. They concluded that at higher flow rates, the battery performed better with flow fields because of increased convective mass transport of reactants.
- Ali *et al*. carried out a numerical study on the number of serpentine design flow channel configurations in determining the performance of VRFB [98]. Their results showed that the higher flow rate and less number of channels significantly improve the distribution of electrolyte in porous electrodes. During discharging, the cell voltages increases by reducing the number of channels and increasing the electrolyte flow rate. The pressure drop decreases with increasing the number of channels in VRFB cell. Furthermore, the electrolyte disruption and flow resistance reduces on increasing number of flow channels, which lead to a smaller pressure drop. The pumping power decreases with the increase of number of flow channels. The maximum power-based efficiency of 97.18% was obtained for the quadruple serpentine flow channel at 60 mL min^{-1}. The lowest pumping power and power efficiency were achieved with the serpentine channel.
- Chen *et al*. examined liquid flow distribution over parallel flow fields using numerical simulations and experimental study [99]. Their results showed extremely high uneven distribution of electrolytes over the whole surface area, with concentrated distribution in the central region of the parallel flow field and vortex flow in the inlet and outlet regions.

- Yang *et al*. experimentally analyzed the performance of single serpentine and parallel flow fields for direct methanol fuel cell (DMFC) [100]. Their results showed that for single serpentine flow fields the open ratio had a significant effect on pressure drop and cell performance. Open ratio (50%) gave the best performance at moderate and low flow rates. Whereas, at low flow rates of methanol, a large open ratio leads to higher power density at the higher current density, corresponding to the mass-transfer limitation region.
- Hamilton and Pollet reviewed materials and designs of flow field plates such as pin type, single serpentine, multiple serpentine flow field designs for their application of PEM fuel cells [87]. Their review study showed that flow field plates of graphite are not as much of popular at this time owing to its high cost and are primarily used for applications of prototypes. Flow field plates of metal struggle to provide a economically effective and corrosion resistant substitute. Composite flow field plate polymer/carbon growing popularity due to its good strength, low-cost, and good conductivity.
- Lu and Reddy measured the performance of micro-DMFCs with four different flow fields: double channel serpentine flow field (DSFF), single-channel serpentine flow field (SSFF), mixed multichannel serpentine with wide channels (MMFW), and mixed multichannel serpentine with narrow channels (MMFN) flow field [101]. Results shows that the power density in the range of 11–23 mW cm^{-2} can be produced by utilizing the active area of 2.25 cm^{2} of the cell. The performance of micro DMFCs with different flow fields is found in the order: double-channel serpentine > single-channel serpentine > mixed multichannel serpentine with wide channels > mixed multichannel serpentine with narrow channels.
- Sudaroli and Kolar experimentally studied the performance of DMFC employs with

single, double, and triple serpentine flow field configurations with an active area of 25 cm^2 of MEA [102]. Three-dimension models were also developed to predict the methanol concentration and current density. Their results showed that with a single serpentine flow field, higher peak power density is achieved at low methanol concentration, ranging 0.25–0.5M. The double-channel serpentine flow field provides higher peak power density at high methanol concentration (1–2M).

- Zhu *et al*. examined the effect of two different flow fields in VRFB, flow-pass and flow-through patterns [103]. Their experimental results showed that using the flow-through pattern increases the active surface area of the electrode and improves also flow distribution of electrolyte, resulting in increase in efficiency up to 5%.
- Suresh *et al*. experimentally and numerically (CFD simulations) determined the enhanced cross-flow in the split serpentine flow field for the fuel cell applications [84]. From their investigation, they found higher cross-flow in the oxygen-depleted region of the adjacent channel in a split serpentine flow field having more than one channels. This flow channel arrangement allows a lower pressure drop resulting in lower the parasitic power losses and more oxygen refilling in the oxygen-deficient regions of the channel.
- Tsushima *et al*. investigated the effect of channel geometry and operating parameters on the performance of VRFB coupled with serpentine and interdigitated flow fields, and found its better performance with interdigitated flow fields [104].
- Darling and Perry compared the flow-through (no channel) porous electrodes with porous electrodes combined with parallel or interdigitated flow field designs (IDFF) [105]. The IDFF designs with thinner electrodes provide better kinetics, lowering ohmic losses, and the flow-through configuration requires thicker electrodes to

produce manageable, acceptable pressure drop, due to which higher ohmic losses occur.

- Dennison *et al*. investigated the mass-transfer effect of various flow fields such as serpentine, parallel, interdigitated, and spiral attached with raw and laser perforated carbon paper electrodes in redox flow batteries [85]. The pressure drop in each flow field configuration was determined. With each flow field, these perforated electrodes are found to be associated with a reduction in pressure drop from 4 to 18 % resulting decreases in pumping losses. The continuous flow path from inlet to outlet in the channels (serpentine, parallel and spiral) exhibits improved performance by 31% when it paired with perforated electrodes, it indicates the fast reactant supply and greater utilization of electrode area. On the other hand, flow fields with discontinuous paths as in interdigitated channel, electrolyte is forced to travel through the electrode, and is adversely affected due to perforations of electrode. The results suggested that mass-transfer can significantly limit the performance with carbon paper electrodes.
- Houser *et al*. experimentally studied the performance of the VRFB system with serpentine, and interdigitated designs, and compared the experimental results with the findings of numerical simulation [71]. Their results showed that interdigitated flow field performed better than the serpentine one, at low flow rates. However, the serpentine and interdigitated, both performed well with thicker electrodes. In later work, they have measured the electrochemical performance and parasitic losses in VRFB and found that high current discharge improves system efficiency [106]. Their results show higher performance of the battery. The pumping energy requirements are reduced due to the high ratio of the cell power to the pumping power while operating the cell at a higher current density.

- Latha and Jayanti performed a comparative hydrodynamics study of serpentine and interdigitated flow fields [65]. Their ex-situ experimental results show that interdigitated flow fields show smaller pressure drop than serpentine flow fields for the same flow rate. The CFD analysis showed strong under the rib convection of electrolyte in both flow fields but at the smaller residence time in case of interdigitated flow fields. In later investigations, they reported an ex-situ experimental study [72]. In this study, they determined the permeability of carbon felt electrodes, which is in the range of $5-8\times10^{-11}$ m^2, varying with compression ratio for redox flow battery applications. The pressure drop across the battery was measured in two serpentine flow fields of different geometrical characteristics over a range of Reynold numbers. Results revealed that importance of under rib convection and differential compression of the porous electrodes as surplus parameter in determining the pressure drop and flow distribution for redox flow battery.
- Kumar and Jayanti experimentally carried out the comparative study of VRFB (active area 100 cm^2) fitted with serpentine, interdigitated, and conventional flow fields (no flow fields) [74]. The effect of electrolyte flow rate in each flow channel was examined. The pressure drop was measured through ex-situ measurements using water over a range of Reynolds numbers, 0 – 1750. They also determined the charge-discharge curve, coulombic efficiency voltage, and round trip efficiency of battery, using each flow field. Their results showed that the highest energy efficiency and the lowest pressure drop can be achieved with serpentine flow fields. The high round trip efficiency of 80% was achieved at the highest flow rate with the serpentine flow field. The performance was stable in each flow field for at least 40 charge-discharge cycles.
- Aaron *et al*. employed a zero gap architecture with serpentine flow fields in order to

improve the performance of VRFB [60]. In zero gap architecture, the stacked sheets of carbon paper as an electrode was employed to achieve a better contact between the cell components with systematic variation of electrode thickness. The peak power density of 557 mW cm^{-2} was achieved with this modified cell architecture. In their another work, the polarization curves analysis has been conducted with two different type of batteries [61]. One is a simple battery using flow-through (no flow fields) with thicker carbon felt electrodes, and another one is fuel cell battery, based on modified DMFC, with electrodes and serpentine flow field. The kinetic polarization was not present in simple battery, but it was significant in the case of fuel cell battery.

- Maurya *et al*. evaluated the performance of three different flow fields; interdigitated, serpentine, and conventional (without flow fields), combined with felt electrodes in a VRFB [107]. The performance was compared with serpentine flow field employing carbon paper electrodes at same experimental conditions. Their results reflect that the interdigitated flow fields show the best performance at low current density, and with the lowest pressure drop. However, the significant mass transport losses occurred at higher current densities in the interdigitated flow fields. The energy efficiency evaluated in conventional, serpentine, and interdigitated are 75%, 64%, and 55%, respectively, which show that the no-flow field provides the highest efficiency owing to its better electrolyte distribution ability.
- Alyasiri and Park developed a novel cell design for enhancing the energy and power of VRFB [108]. The new design eliminates the use of endplates and gaskets, for better safety and long life and convenience of use of lesser components than conventional VRFB cells. Electrochemical measurements, like cycling and polarization measurements, were performed over a wide range of flow rates and current densities. Analysis of internal resistance was also performed using EIS

method for the comparison between new and conventional designs. The results showed that the new designs give better charge-discharge cycling with better stability and energy efficiency than conventional VRFB.

- Akuzum *et al*. investigated the effect of varying depth of flow channel along with creating various channel hindrances on the performance and pumping power requirement of VRFB [109]. A 3D-printed ramps and prismatic obstructions were inserted into the channels of interdigitated and parallel flow field designs to determine the effect of non-uniform depth on mass transport properties. Results showed that integrated ramps in the flow field designs resulted 15% increase in peak power density and 40% drop in pumping pressure.
- Ma *et al*. developed a kilo-watt VRFB system to investigate the effect of electrolyte flow rate on the performance of VRFB [110]. Their experimental results showed that increasing the electrolyte flow rate causes increasing the capacity but decreasing the system efficiency. The system efficiency can be improved by as high as 8%, while also keeping capacity high by using optimal strategy of flow rate of electrolyte for charge/discharge cycles.
- Gundlapalli and Jayanti experimentally studied the influence of channel dimension of serpentine flow field in VRFB [111]. The study is based on three different factors: the effect of felt intrusion inside the flow channel, the effect of electrolyte flow rate on pressure drop, and the effect on electrochemical performance characterized by the number of parameters. The serpentine flow fields with two cells of active areas 400 cm^2 and 900 cm^2 were studied using eight variations of channels and rib dimensions. The results showed that the pressure drop, power density, and discharge energy density improved in the larger cell area.

Distribution of electrolyte in the porous electrode is one of key research areas for flow batteries such as a VRFB. Non-uniform distribution of electrolyte limits the performance of the device, and lowers its efficiency. It causes underutilization of some part of electrode, and overutilization of the rest part. This results in mass transfer limitation leading to slow reaction kinetics. Most of the studies have been conducted to solve this issue by using heat treatment and chemical treatment of electrodes. Another approach to overcome this issue is through better distribution of electrolyte in the porous spaces of electrodes. It can be achieved at higher flow rates, i.e., at increased pressure losses, leading to higher pumping cost which is not a suitable solution in economic aspect. A well-designed flow channel is a key solution for providing uniform distribution of electrolytes and higher utilization of electrodes even at a low flow rate. Commonly used flow patterns are: Serpentine, Interdigitated, and parallel. This thesis presents three different types of flow channel: Split Serpentine, Split-Merged Serpentine, and Sinusoidal Wave-Type Serpentine, which were designed and fabricated. For comparison purposes, a Conventional Serpentine channel, which is widely used, is also fabricated. Results show that designed channels are superior in all aspects of performance evaluation criteria of a VRFB.

Chapter 3: Experimental methods and materials used

3.1 Experimental setup

Figure 3.1 shows a schematic of experimental setup of VRFB which consists of positive and negative electrolyte tanks, a single-cell of active area 10 cm^2, two peristaltic pumps, a redox flow battery test station, and a computer. The tanks are filled with respective electrolyte solutions of vanadium which are circulated through the cell by connecting pipes using peristaltic pumps. The cell is connected to the test station through working and counter electrode clips to apply/withdraw current to/from it. A N_2 gas cylinder is connected to the both electrolyte tanks through pipes to create an inert environment. Figure 3.2 shows the actual experimental setup of VRFB along with subsystems installed in laboratory for electrochemical measurements.

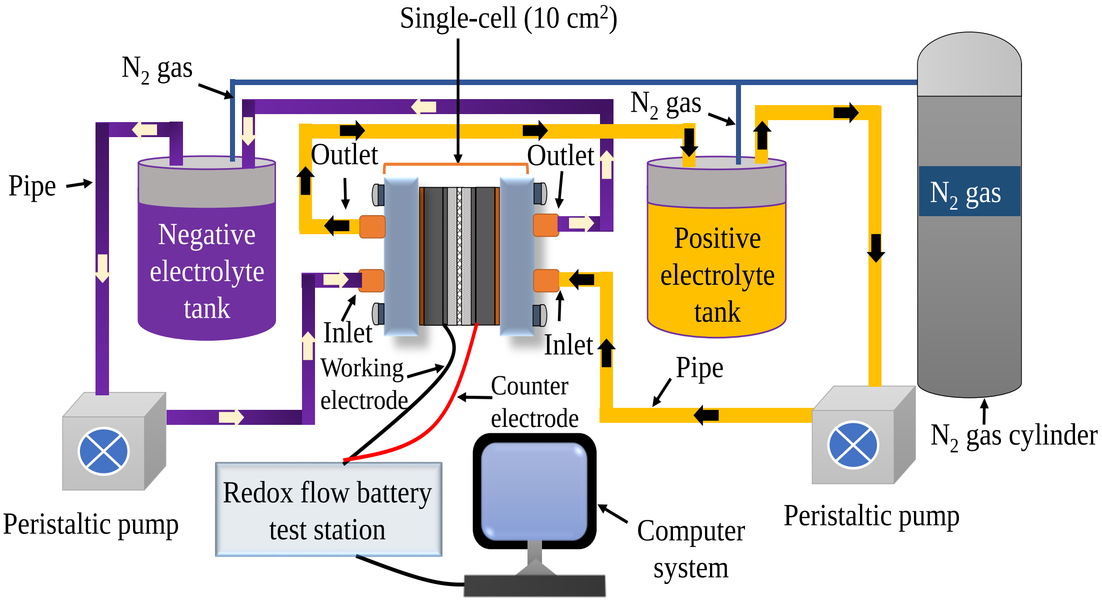

Figure 3.1. A schematic of experimental setup of VRFB. It consists of positive and negative electrolyte tanks, two peristaltic pumps, single-cell, a redox flow cell test system, N_2 gas cylinder, and a computer system.

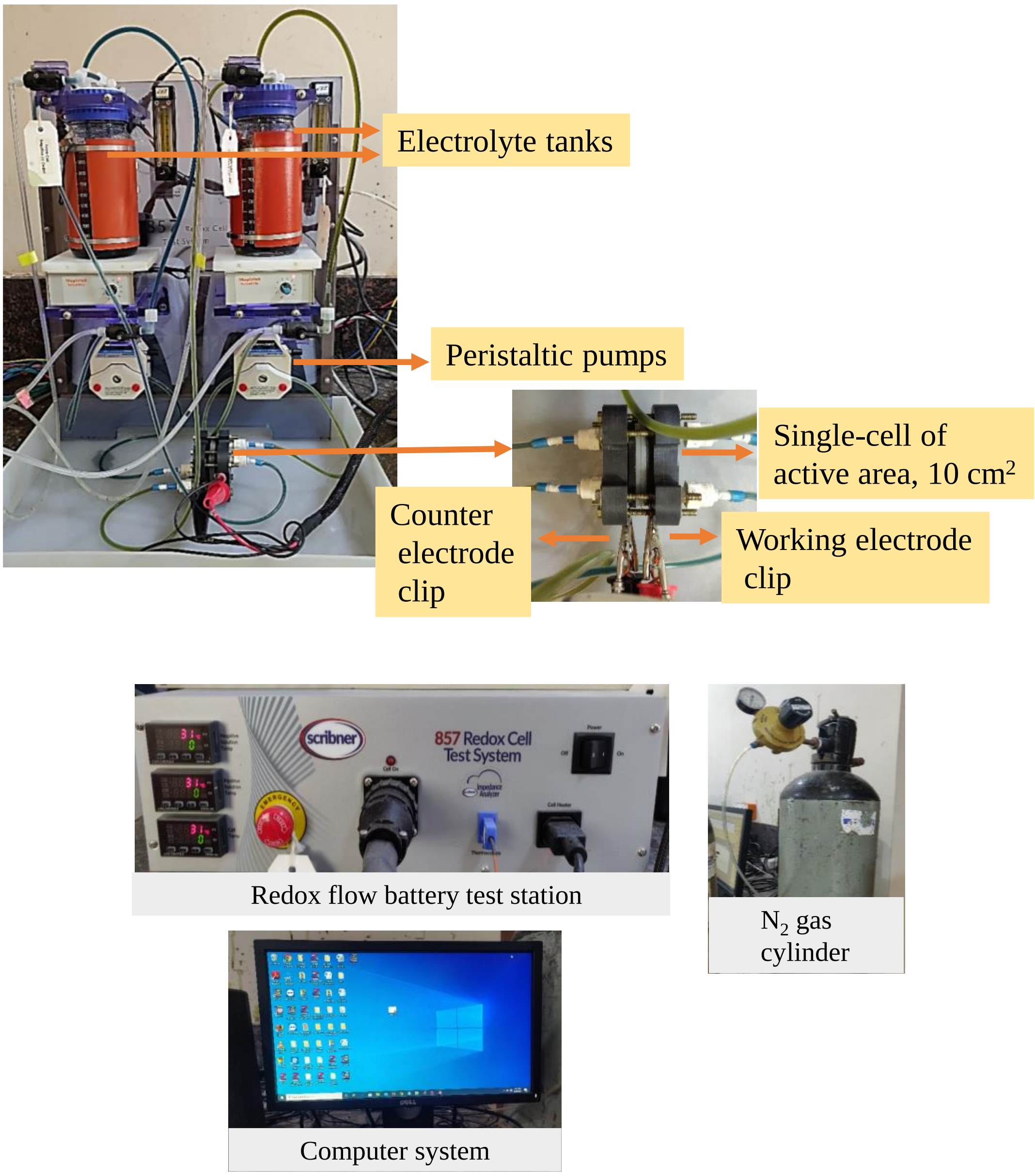

Figure 3.2. Experimental setup of VRFB installed in laboratory used for electrochemical measurements.

3.2 Single-cell assembly

A single-cell of VRFB of active area 10 cm^2 procured from Fuel Cell Store, USA, was employed for all experiments. The cell comprised of a Nafion-117 membrane (Alfa Aesar), which was treated by heating in DI water, H_2O_2, and H_2SO_4. Detailed treatment procedure is discussed in later Chapters. Picture of the membrane before and after treatment is shown in Figure 3.3. The treated membrane with a pair carbon felt electrodes

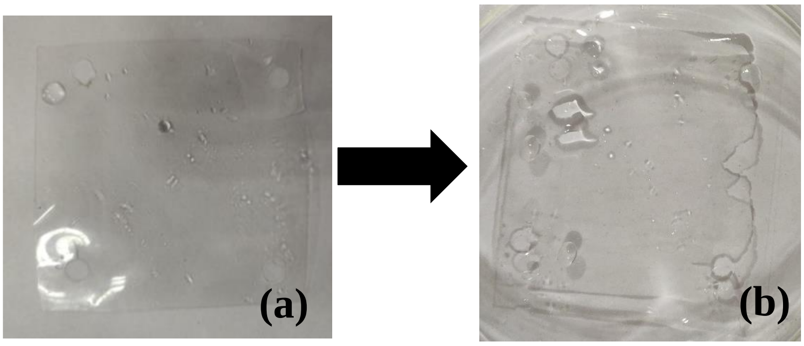

Figure 3.3. Images (a) and (b) shows the Nafion-117 membrane before treatment and after treatment.

(43200 Carbon felt, 6.35mm (0.25in) thick, 99.0%, Alfa Aesar), two gaskets of silicon, two fabricated flow channel plates of graphite, two copper-current collectors is placed between the two end-plates. The schematic of cell components is shown in Figure 3.4.

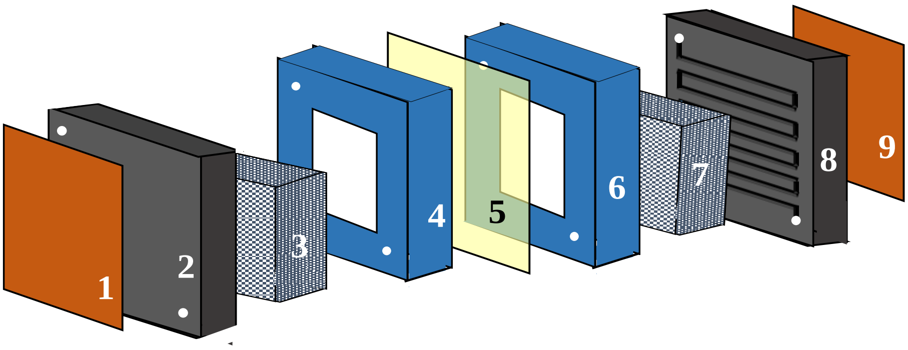

Figure 3.4. Schematic of VRFB cell assembly consist of (1, 9) copper current collectors; (2, 8) graphite flow channel plates; (3, 7) carbon felt electrodes; (4, 6) silicon gaskets; (5) Nafion-117 membrane. Figure not to scale.

Dimensions of each component are given in Table 3.1. All these components are assembled, leading to 32% compression, by following procedures:

- Thickness of each component of cell before assembling was measured using a vernier caliper. Total thickness = one membrane + two electrodes + two gaskets + two flow channel plates = 30.88 mm. Thickness of current collectors are not considered here because they were kept inside the cavity of end plates.

- All components were tightened using wrench by applying weight of 100 g followed by 200 g in a star cross pattern. Since electrodes are the only compressible parts, effect of compression translates to them only. The final thickness after compression was 21.00 mm which corresponds to 32 % compression.

Table 3.1. Thickness and dimensions of the components of cell assembly.

Components	**Size**	**Thickness**
Membrane	53 mm × 53 mm	0.18 mm
Electrodes	3.18 mm × 3.18 mm	6.35 mm
Gaskets	53 mm × 53 mm with square opening of same size of electrodes	5.0 mm
Flow channel plates	53 mm × 53 mm	4.0 mm
Current collectors	3.18 mm × 3.18 mm	0.4 mm

The cell assembly of VRFB used in experiments is shown in Figure 3.5. After assembling cell components, resistance between the cell components was measured using digital multimeter. After the resistance test, leakage test of cell was performed at varying flow rates of DI water and 4.0 M H_2SO_4 solutions. The detailed leakage testing procedure is given in later Chapters.

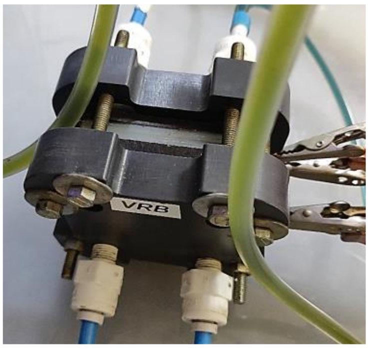

Figure 3.5. VRFB: Single-cell assembly.

3.3 Preparation of electrolyte solutions and charging procedures

Initial electrolyte solution for charging was prepared by dissolving 1.0 M $VOSO_4.\ x\ H_2O$, $x = 2$, (97%, Sisco Research Laboratories Pvt. Ltd., India) in 4.0 M H_2SO_4. Both positive and negative electrolyte tanks were filled with 100 mL of electrolyte solution of *V*(IV) and were kept at constant stirring under an inert atmosphere created by continuous flow of N_2 gas. The solutions were charged using two step charging procedure with a constant current density of 40 mA cm^{-2}. A schematic of charging procedure is shown in Figure 3.6.

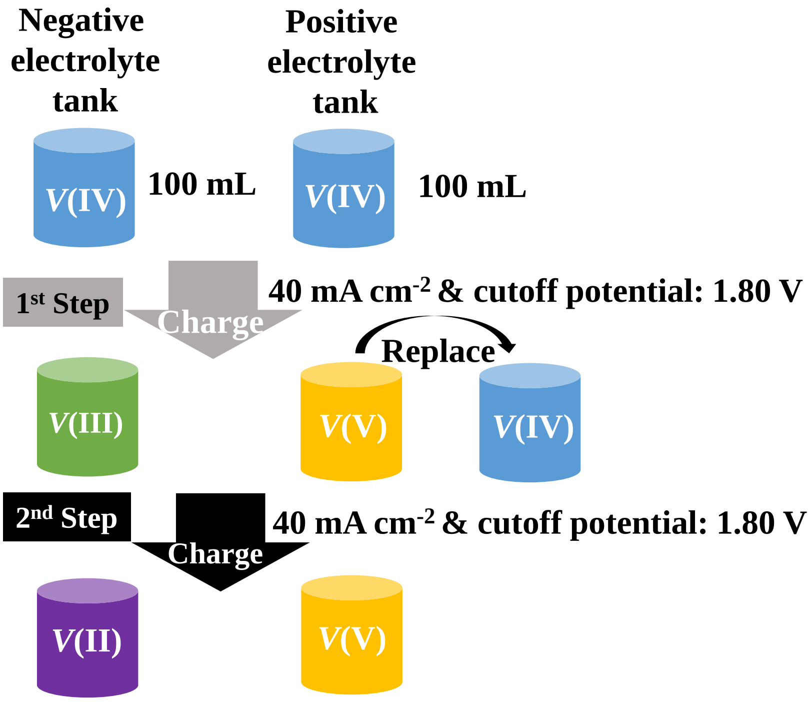

Figure 3.6. A schematic showing change of oxidation states of vanadium ions during first step and second step charging.

A cutoff potential of 1.80 V was set at each charging step. First step charging converts *V*(IV) to *V*(V) in positive and *V*(III) in the negative tanks, respectively. In the second step of charging, the solution of positive tank containing *V*(V) is replaced with 100 mL of *V*(IV). The subsequent charging converts *V*(IV) to *V*(V), and *V*(III) to *V*(II) in the respective tank. Figure 3.7 shows change of color of solution during first and second charging step, indicating change in oxidation state of vanadium. Each oxidation state of vanadium ions possess different color. The colors of *V*(II) to *V*(V) solutions are shown in Figure 3.8.

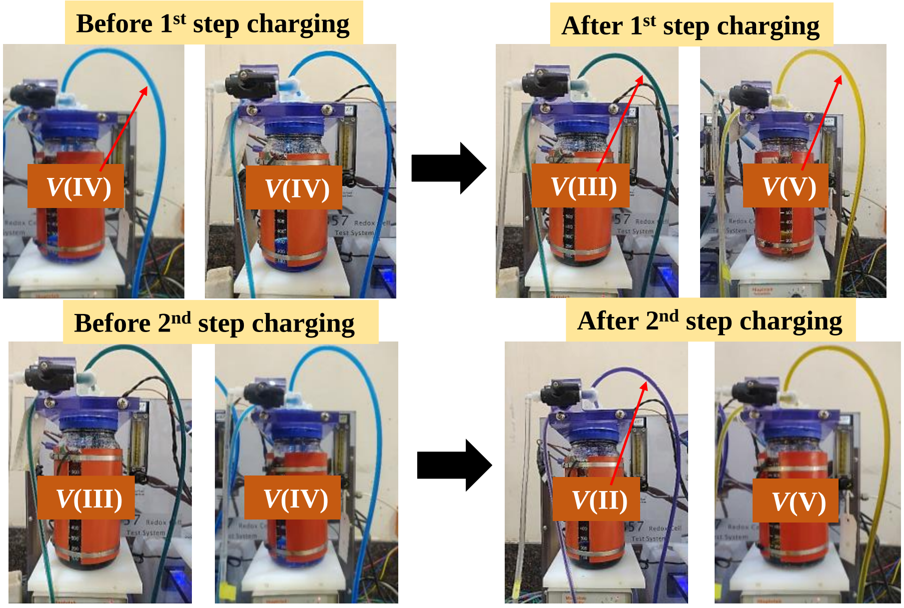

Figure 3.7. The change of oxidation states of vanadium ions during first step charging, showing conversion: *V*(IV) to *V*(V) and *V*(IV) to *V*(III), and the second step charging, reflecting: *V*(IV) to *V*(V), and *V*(III) to *V*(II) conversion at positive and negative side, respectively.

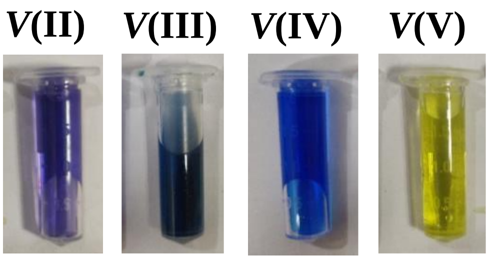

Figure 3.8. Colors of transformed oxidations states of vanadium ions: violet-*V*(II), green-*V*(III), blue-*V*(IV), yellow-*V*(V).

The temporal change in cell potential during first and second charging steps is shown in Figure 3.9. During first step charging, on applying current density of 40 mA cm^{-2}, the potential increases slowly and steadily from initial value of 1.37 V before it shoots up abruptly to 1.80 V. The abrupt potential change might be due to mass transfer limitation on anodic side, where V(IV) converts to V(V) and concentration drops to a very low value, or complete conversion of V(IV) occurs. The total time for charging in first step is 4.78 h. In the second step charging, the initial potential of charging is 1.42 V, and reaches 1.80 V in 4.58 h. After second step charging, the battery shows OCP of ~1.52 V representing stability of potential with time, as illustrated in Figure 3.9 (b).

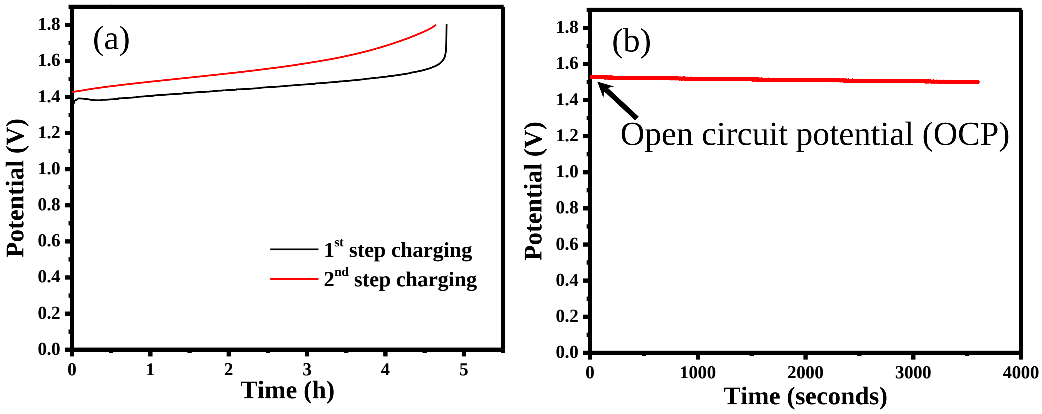

Figure 3.9. (a) Potential vs. time plot during first and second step of charging. (b) Battery showing stable OCP of ~1.52 V after second step charging.

3.4 UV-Vis measurement

Presence of vanadium with different oxidation state is characterized by its distinct color which was already discussed earlier. Chemistry of vanadium is very versatile with distinct species presents at various potentials and pH values [36]. Because electrolyte employed in VRFB is a mixture of vanadium ions and H_2SO_4, as supporting electrolyte, UV-Vis spectroscopy is used to reveal the presence of vanadium species. It gives fingerprints of different vanadium ions by providing different absorbance peaks at different wavelengths. Reported absorbance peak of *V*(IV) is obtained at wavelength of 765 nm. For *V*(II) and *V*(V), it falls at 855 nm and 390 nm, as shown in Figure 3.10 [46]. *V*(III) shows two distinct peaks at two different wavelength, one at 610 nm [46], another at 400 nm [112]. The working principle of UV-Vis spectroscopy is based on Beer's law which relates the concentration of a substance in a solution to the absorbance:

$$A = \varepsilon . b . c \, , \tag{3.1}$$

where A is the absorbance of a liquid substance, ε is a molar absorptivity, b is the length of a cuboid cuvette, and c is the concentration of the liquid sample.

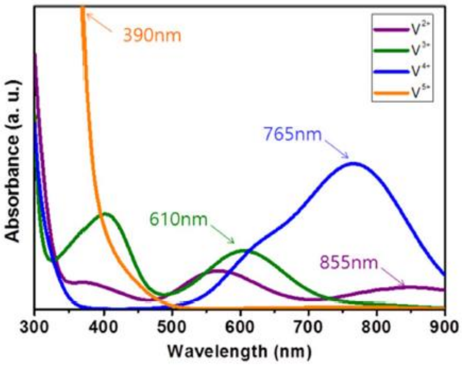

Figure 3.10. UV-Vis spectra of *V*(II), *V*(III), *V*(IV), and *V*(V) at different wavelength [46].

UV-Vis spectroscopy of positive and negative electrolyte solutions was performed in this work to determine the presence of oxidation states of vanadium species. The samples of electrolyte solutions were diluted ten times before the measurements. Dilution of electrolyte solution is necessary to allow significant amount of light to pass through it. The UV-visible spectrophotometer used for UV-Vis measurements is shown in Figure 3.11.

Figure 3.11. UV- visible spectrophotometer used for determining vanadium peaks.

A quartz cuvette of 1 cm was rinsed with DI water and acetone, and is subsequently dried in an oven at 50°C to remove excess water. The measurement was performed in the visible range of 300 to 1000 nm wavelength. Absorbance peak of the initial electrolyte solution of *V*(IV) is obtained at 765 nm as shown in Figure 3.12. Peak of *V*(V) in the positive electrolyte solution after second step charging was obtained at 390 nm as shown in Figure 3.13(a), indicating presence of *V*(V).

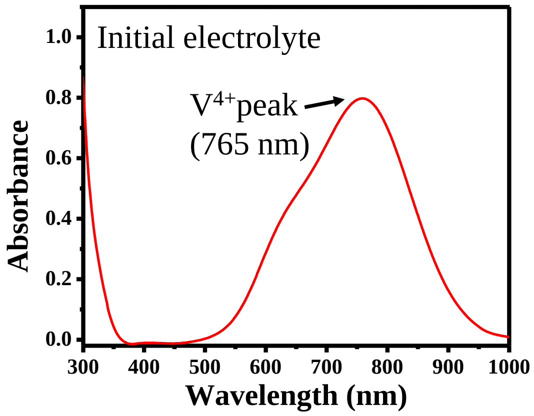

Figure 3.12. UV-Vis of the initial electrolyte solution of *V*(IV).

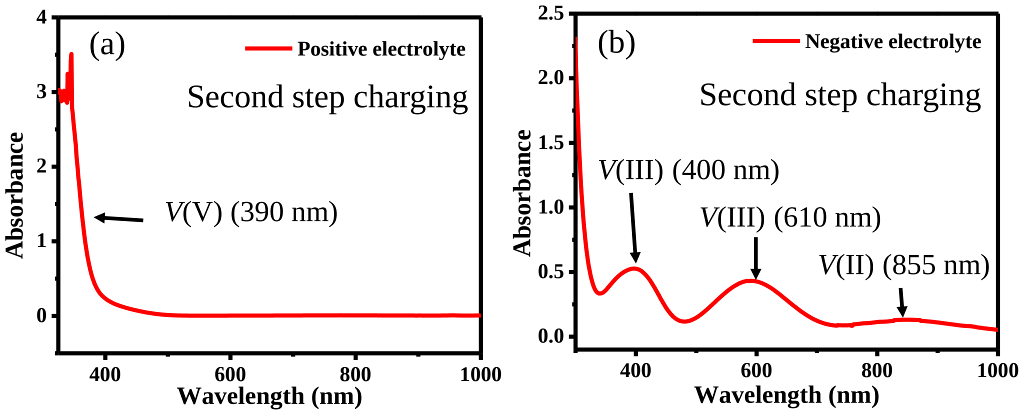

Figure 3.13. (a) Absorbance peak of *V*(V) present in positive electrolyte solution, and (b) Peak of *V*(III) and *V*(II) in negative electrolyte solution after second step charging.

Since, the absorbance of *V*(V) is very high as compared to *V*(II), *V*(III), and *V*(IV), the concentration of negative electrolyte solution was reduced to less than 1 mM to ascertain the presence of other vanadium ions in the scale range. The presence of *V*(III) in the negative electrolyte solution was evident by two characteristic peaks observed at different wavelengths as shown in Figure 3.13 (b). The peaks were also matched with literatures [112,113]. A small peak was obtained at 855 nm, confirming the presence of *V*(II) alongwith *V*(III) in the negative electrolyte solution. Peak of *V*(II) is found smaller than *V*(III), indicating oxidation of *V*(II) to *V*(III) due to exposure in air. Results show no trace of *V*(IV) and *V*(V) ions.

3.5 Experimental Troubleshooting

3.5.1 Corrosion of copper current collectors

On performing multiple experiments, the corrosion of copper current collector plates was observed. This might be due to plates come in contact with leaked acidic solution or environmental exposure. A corroded current collector with layering is shown in Figure 3.14. This leads to increase in ohmic losses in the cell, indicated by higher overpotential.

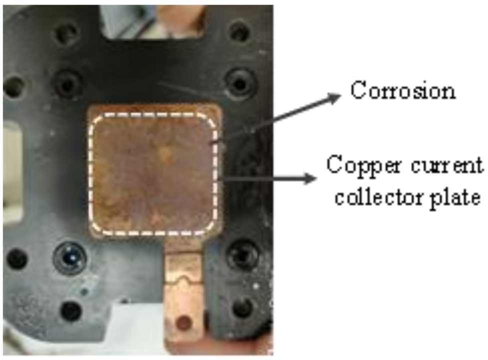

Figure 3.14. Corrosion over copper current collector plates during experiments.

For instance, when the cell is initiated charging by applying a constant current density, the initial potential shows more than 1.80 V, higher than the cutoff potential. This problem was resolved by disassembling the cell, and cleaning the copper current collector plates. Leakage issue was frequently encountered while performing the experiments. During testing of the cell, leakage of solution occurs due to improper alignment of inlet and outlet holes of gaskets and flow channel plates. Due to which, the liquid electrolyte could not pass from the flow channel plate to the carbon felt electrodes through gaskets, leading to increased pressure at inlet and, thus, to leakage. Another reason for leakage is non-uniform compression of gaskets and carbon felt electrodes, resulting in uneven distribution of liquid pressure inside the cell. This problem was resolved by aligning the holes of gaskets and flow channel plates for the smooth transfer of liquid electrolyte and by adjusting tightness of nuts and bolts.

3.6 Electrochemical measurements: Polarization curve, EIS, and discharge-charge behavior

Polarization curves of VRFB were performed by measuring the potential across the cell while discharging the electrolytes at varying current densities and flow rates. A scheme of polarization measurements with chosen flow channels and flow rates is shown in Figure 3.15.

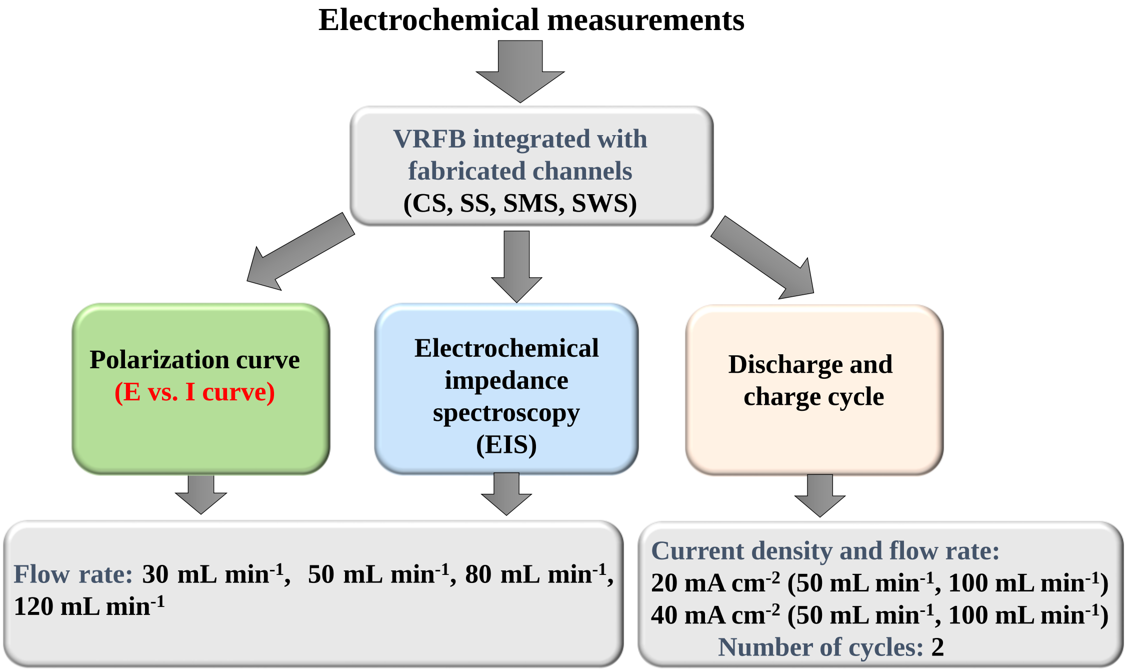

Figure 3.15. Schematic representation of different types of electrochemical measurements performed in VRFB employed with fabricated channels.

Potential was measured for 30 s at a fixed current density, followed by 2 minute of rest given before discharging at the next higher current density value. The average potential of the last 20 s was taken to neglect the contribution of charging of double layer capacitance. This capacitance develops at the electrode-electrolyte interface due to accumulation of charges. No electrochemical reactions occur during the process. The resultant current is called the non-faradaic current. The *iR*-losses occurred in cell were determined using high-frequency response (HFR) of the cell. Subsequently, the obtained polarization curve was corrected by omitting the *iR*-losses. The detailed measurement of polarization curve is discussed in later Chapters. EIS of VRFB was performed at four different flow rates as shown in Figure 3.15. A sinusoidal voltage of amplitude 10 mV was applied, and the frequency was varied from 10 kHz to 1 mHz. Two discharge-charge cycles of VRFB coupled with fabricated channels were performed by varying current densities and flow rates, as shown in Figure 3.15. The cutoff potential was set at 0.80 V and 1.80 V. Discharge-charge experiments in details are given in the following Chapters.

Chapter 4: Enhancing power density of a vanadium redox flow battery using modified serpentine channels

Abstract

The performance of two modified serpentine flow patterns: Split Serpentine (SS) and Spilt-Merge Serpentine (SMS), was compared to that of a conventional serpentine (CS) through polarization curves. The charge-transfer resistance (R_{ct}) was evaluated using electrochemical impedance spectroscopy measurements. Results show that ~2.5 and ~5 times higher current can be withdrawn employing SMS and SS channels, respectively, with graphite felt electrodes in a vanadium redox flow battery (VRFB), in comparison to using a CS channel. Power density increases with increasing electrolyte flow rate, and the peak densities at 120 mL min^{-1} are: 552 mW cm^{-2} (SS), 363 mW cm^{-2} (SMS), and 154 mW cm^{-2} (CS). On contrast, the electrode with SMS channel shows lower R_{ct} than with SS channel. Resistance is maximum with CS channel. These results suggest that the SS flow pattern has highest electrolyte distribution ability, resulting in increased contact with the porous electrode, followed by SMS and CS patterns.

4.1 Introduction

Growing environmental concerns arising from the use of fossil fuels have led many countries to look for ways and means for harvesting renewable energy such as wind and solar energy to fulfill their energy basket. The intermittent nature of these energy sources and their availability at remote places obstruct their direct use in different applications. However, the energy from these sources can be stored and used employing a vanadium redox flow battery (VRFB) [114–117]. It is an electrochemical energy conversion setup consisting of two electrolyte tanks (positive electrolyte tank has VO_2^+/ VO^{2+} redox couple and negative electrolyte tank has V^{3+}/V^{2+} couple), two pumps and a membrane electrode assembly (MEA). The electrolyte solutions are pumped through the MEA, where following electrochemical reactions occur during charging (storing energy) and discharging (using stored energy) processes:

$$\text{Positive side: } VO^{2+} + H_2O \underset{\text{Discharging}}{\overset{\text{Charging}}{\rightleftarrows}} VO_2^{+} + 2H^{+} + e;\ E^0 = 1.00\ \text{V} \tag{4.1}$$

$$\text{Negative side: } V^{3+} + e \underset{\text{Discharging}}{\overset{\text{Charging}}{\rightleftarrows}} V^{2+};\ E^0 = -0.26\ \text{V} \tag{4.2}$$

One of the major advantages of this system is that the energy and power capacities can be independently scaled up [32]. Energy capacity is determined by concentration and volume of electrolytes in the respective tank, and power capacity depends on the size of an MEA. The assembly consists of a proton exchange membrane sandwiched between two porous electrodes, two current collectors engraved with flow patterns, and two end plates. Schematic diagram of a typical VRFB can be found elsewhere [36,116]. As electrochemical reactions occur at the surface of an electrode in contact with liquid electrolyte, managing its uniform distribution is a great challenge, hence requires serious attention. The performance of the battery deteriorates with the electrolyte maldistribution stemming from channeling and uneven wetting of electrode [32,99,110,118]. Overutilization of some part of electrode and underutilization of other part lead to uneven current density and shorter life cycle of the battery. A flow pattern helps in even distribution of electrolyte in the porous electrode [65,72,74,84].

The transport of electroactive species from electrolyte to and fro the reaction sites occurs by convection and their diffusion through the porous electrodes [32]. The flow rate of electrolyte through channel contributes to the convective mass transport of species. The pressure in the channel and diffusion of electroactive species arising from concentration gradient contribute to the distribution of electrolyte on the porous electrode. At low flow rate, the liquid electrolyte is not able to reach in the sufficient amount to the electrode surface. The uniform distribution can be achieved at higher flow rates [65,74], at the expense of increased pumping cost to overcome viscous drag and head loss from flow channel and electrode. A properly designed flow pattern enhances mass transport even at lower flow rates, minimizes the pumping cost for electrolyte circulation and thus improves the performance of the battery. Rudolph et al. [119] measured the efficiency of a VRFB employed with different flow configurations. They optimized the parameters and flow configuration at inlet and outlet of the flow plate leading to uniform distribution of the electrolyte.

Transport of electroactive species plays a crucial role in power output and charge-discharge cycle. A very limited design of flow channels have been reported in the literature. Of all, very common and frequently used channel patterns are: serpentine, interdigitated, parallel and spiral, and their variants. There are also some work reported for the battery without any flow field [63,73,74]. A VRFB with flow fields shows higher efficiency than without no fields, even including the cost towards larger pressure drop. The performance of a flow pattern is cumulative effect of its design, properties of electrode and electrolyte, and operating conditions [71]. At lower electrolyte flow rates, interdigitated flow fields with the thin electrodes perform better than serpentine, showing increased discharge capacity. At higher flow rates, both perform equally well. A hydrodynamics study performed on both channels shows that a lower pressure drop incurs with interdigitated flow field at same flow rate resulting from shorter residence time [65,72]. Denninson et al. [85] investigated the mass transport effects of flow fields with continuous path from inlet to outlet, such as serpentine, parallel and spiral, and with discontinuous path, such as interdigitated, along with carbon paper electrodes. Their results show that the continuous path flow fields show up to 31% improved performance in comparison to the latter. Experimental findings of Kumar and Jayanti [74] show that the performance of a VRFB employed with serpentine flow field improves its energy efficiency in comparison to interdigitated and conventional (no pattern) flow fields. A round trip efficiency of approximately 80% was achieved with serpentine flow field at high flow rate. Results extracted from a 3D numerical model of a VRFB by Xu et al. [73] illustrated that the serpentine flow field outperforms parallel and conventional flow fields, and highest energy efficiency and round-trip efficiency were achieved. Maurya et al. [107] through experimental and computational fluid dynamic studies evaluated the performance of above three flow field designs fitted with carbon felt electrodes. The highest energy efficiency was achieved using conventional flow field followed by serpentine and interdigitated flow fields, attributed to their respective electrolyte distribution ability. Tsushima et al. [120] investigated the performance of the battery employing serpentine and interdigitated flow channels and showed that the latter performs better with both carbon felt and carbon paper electrodes. These findings are in contrast with those of Kumar and Jayanti [74]. Houser et al. [106] proposed equal path length (EPL) and aspect ratio (AR) flow designs; EPL shows enhanced mass transport characteristics, but at increased pressure drop, if compared with serpentine and interdigitated flow fields. Employing AR design reduces pressure loss and improves system efficiency. The flow fields have also been employed in the liquid based fuel cell, aiming its even distribution over electrode surface. Lu et al. [101] proposed four variants of serpentine flow field: single-channel serpentine (SSFF), double-channel serpentine (DSFF), mixed multichannel serpentine with narrow channels (MMFN), and mixed multichannel serpentine with wide channels (MMFN), for direct methanol fuel cell (DMFC). Of all, DSFF provides highest peak power density. A similar work of Sudaroli et al. [102] on DMFC employing SSFF, DSFF and TSFF (triple-channel serpentine) shows that the performance of the flow field is concentration dependent; SSFF outperforms at low methanol concentration, and DSFF at higher concentration.

The dimension of a flow channel and electrolyte flow rate also influence the performance of a VRFB. Employing wide channels helps reducing pressure drop without losing the electrochemical activities [111]. A 3D electrochemical steady-state model of a VRFB with varying channel height shows that the battery has better energy efficiency at low height of the channel, owing to better electrolyte distribution, but at higher pumping cost [89]. The coulombic, voltage and energy efficiencies increase, but system efficiency decreases, with increasing electrolyte flow rate [110].

As the geometry of a flow channel plays an important role in electrolyte distribution over the porous electrode leading to enhanced mass-transfer of electroactive species, we modified serpentine flow pattern creating split serpentine (SS) and split-merged serpentine (SMS) flow channels. These channels were engraved on 10 cm^2 area of a graphite plate. The performance of a VRFB employed with designed channels and graphite felt electrodes was evaluated by polarization curves and was compared to that with a conventional serpentine (CS) channel of same area and at same operating conditions. Kinetic, ohmic and mass-transfer resistances of the battery were determined using electrochemical impedance spectroscopy (EIS). Results show that these designed channels outperform CS channel. Highest current and power densities were achieved using a SS channel followed by SMS and CS channels at same conditions. EIS studies show that designed channels reduce kinetic overpotential resulting from better distribution of electrolyte and penetrating larger depth of the porous electrode.

4.2 Experimental

4.2.1 Design and fabrication of flow channels

Three flow patterns were designed: (a) Conventional Serpentine (CS), (b) Split Serpentine (SS), and Split-Merged Serpentine (SMS), using AUTOCAD and are respectively shown in Figure 4.1(a)-(c).

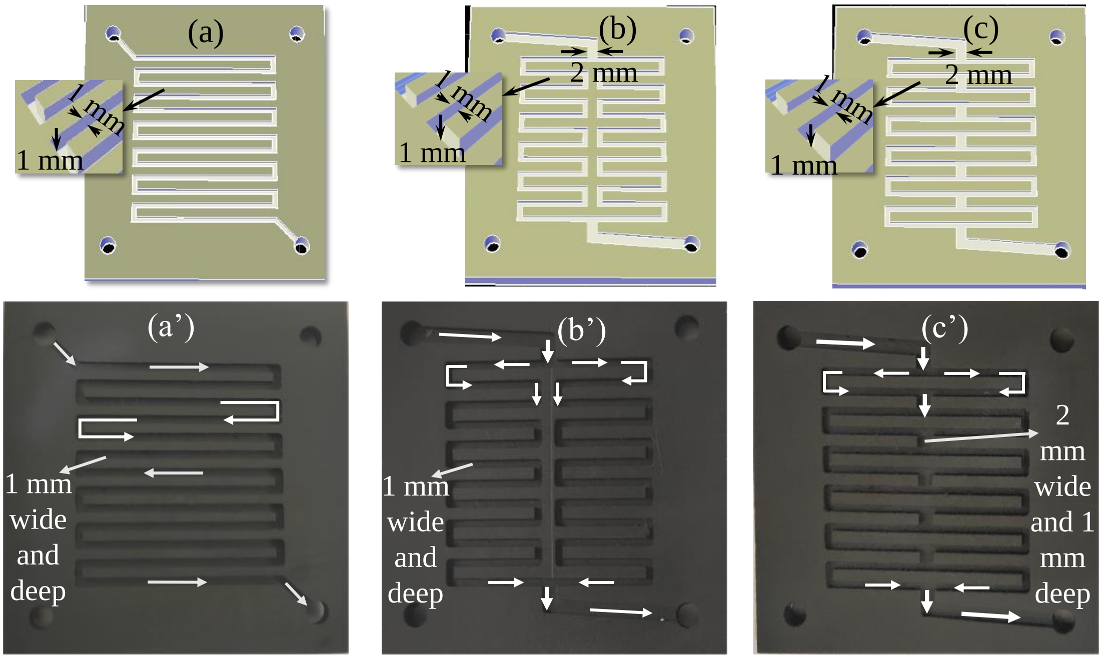

Figure 4.1. AUTOCAD designs of flow patterns: (a) CS (b) SS and (c) SMS. Pictures of corresponding flow channels are shown in (a'), (b'), and (c'). Channels were engraved on 4-mm-thick graphite plate with channel dimensions: 1 mm wide and 1 mm deep. White solid arrows indicate the direction of electrolyte flow inside channels.

These flow patterns were engraved on 10 cm^2 area of 4-mm-thick graphite plate using CNC machine, and pictures of corresponding fabricated channels are shown in Figure 4.1(a')-(c'). The CS channel is fabricated to comparatively analyze performance of SS and SMS channels. The width and depth of a flow path are 1 mm, and the distance between the two paths is accordingly adjusted. The electrolyte flow direction in all channels is also indicated in Figure 4.1(a')-(c'). The flow in the CS channel follows a single path, from inlet to outlet. The inlet and outlet lines of SS and SMS channels are 2-

mm wide and split into two 1-mm-wide flow paths. The split flows in SS channel follow their own, separate path, but the SMS channel allows electrolyte to alternatively mix and split. Parameters, such as engraved volume, surface area, open area and path length of flow pattern, of these fabricated channels are presented in Table 4.1. Surface area includes area three surfaces of a channel, and the area of fourth surface (open surface) is referred as open area. The values presented in table indicate that volume and areas are almost same, but the path length of SMS and SS channels is nearly half of the CS channel.

Table 4.1. Parameters, such as engraved volume, surface area, open area and path length of flow pattern, of three fabricated channels: CS, SS and SMS, on 4-mm thick graphite plate as shown in Figure 4.1(a')-(c'). Surface area includes area of three surfaces of a channel and the area of fourth surface (open surface) is referred as open area.

Channel type	Engraved volume (mm^3)	Total surface area (mm^2)	Open area (mm^2)	Path length (mm)
CS	416	1245	416	416
SS	373	1084	392	206
SMS	393	1193	412	206

4.2.2 Membrane pretreatment for VRFB

Nafion® 117 membrane (Alfa Aesar) was employed as an electrolyte in the VRFB. A piece of 10 cm^2 area similar to engraved section of fabricated channels was treated as mentioned in the literature [3,121,122]. The treatment process comprises of four steps: (i) heating in 3.0% H_2O_2, (ii) heating in deionized water, (iii) heating in 0.5 M H_2SO_4 (99.0%, SD Fine-Chem Limited, India), and (iv) heating again in deionized water to remove excess acid. The temperature at each step is kept at 80°C. The thus treated membrane was dipped in deionized water for future use.

4.2.3 Assembly and testing of the single-cell VRFB

A single-cell VRFB hardware of area 10 cm^2 was procured from Fuel Cell Store, USA. It was assembled comprising of the treated Nafion membrane, two 6.35-mm-thick, uncompressed carbon felt electrodes (Alfa Aesar), two fabricated channel plates of same pattern, two current collectors (copper), two end-plates and two 5mm thick gaskets. The electrodes were used as received. All cell components were assembled as mentioned in the literature [74] following standard criss-cross tightening sequence. Only compressible component in the assembly is carbon felt electrode inserted in the hole of gasket. The thickness of components measured before assembling and final thickness of the cell show that a compression of approximately 32% was achieved. The assembly was tested for contact resistances using a digital multimeter (Fluke) followed by its leakage test. Distilled water was pumped through both sides of the cell assembly at varying flow rates: 30, 50, 80, 110, 150 and 180 mL min^{-1}. The leakage test was also performed by pumping 4.0 M H_2SO_4 solution at above flow rates. These steps also help in washing out impurities from the cell and in hydrating membrane.

4.2.4 Preparation of electrolyte solution

An electrolyte solution of volume 300 ml was prepared by dissolving 1.0 M $VOSO_4.xH_2O$ (97%, Sisco Research Laboratories Pvt. Ltd., India) in 4.0 M H_2SO_4 (Sulfuric acid, 96%, Sigma- Aldrich). The negative (containing V(II) ions) and positive electrolyte (containing V(V) ions) solutions were prepared through electrochemical conversion of the prepared solution by two-step charging method [61] employing 857 Redox Flow Cell Test System, Scribner Associates, Inc. The two tanks of the test system were filled with 100 ml of the prepared V(IV) electrolyte solution. The solutions were pumped through the cell assembly at 50 mL min^{-1} and were charged by applying a constant current density of 40 mA cm^{-2}. The cutoff potential was set at 1.80 V. In the first step charging, the oxidation state of vanadium ions changes, converting V^{4+} to V^{5+} in the positive tank and from V^{4+} to V^{3+} in the negative tank. Before proceeding for the second step charging, the solution in the positive tank is replaced by remaining 100 ml of V(IV) solution. This charging step converts V^{4+} to V^{5+} and V^{3+} to V^{2+} in the respective tanks. The change in oxidation state of vanadium ions was also confirmed by altering color of the electrolyte solution: violet (V^{2+}), green (V^{3+}), blue (V^{4+}), and yellow (V^{5+}). The measured open circuit potential (OCP) of the fully charged electrolyte solutions was 1.51 V. During the charging process, both tanks were continuously purged with nitrogen gas preventing oxidation of solution in presence of environmental oxygen.

4.2.5 Electrochemical measurements

Polarization curves were obtained by pumping prepared positive and negative electrolyte solutions at respective side of the cell assembly integrated with two same-type (CS, SS or SMS) fabricated flow channels. Four electrolyte flow rates were chosen: 30, 50, 80 and 120 mL min^{-1}. The flow rate was kept same on both sides. The potential across the cell was measured while discharging the electrolytes for 30 s at a constant current density. The average potential of last 20 s was taken, eliminating the capacitive effect arising due to charge accumulation near the electrode surface. The applied current density was increased by a step of 5 mA cm^{-2} until the measured potential shows a zero value, indicating maximum limiting withdrawn current. The *iR*-loss stemming from ionic resistance of membrane was evaluated using high frequency response (HFR) of the cell. The obtained polarization curves were corrected by subtracting the *iR*-loss.

The electrochemical impedance spectroscopy (EIS) of the VRFB employing fabricated channels was also performed by circulating the fully charged electrolyte solutions at above four flow rates. A sinusoidal fluctuation of 10 mV in potential (the potential corresponding to withdrawn current density of 0.01A cm^{-2}) was applied in the EIS measurements. The frequency was varied from a higher value of 10 kHz to as low as

0.001 Hz. All electrochemical measurements were carried out at room temperature employing 857 Redox Flow Test Station.

4.3 Results and discussion

4.3.1 Performance analysis of VRFB employed with fabricated channels through polarization curves

The performance of an electrochemical energy storage system is best analyzed by polarization curves. It helps in truncating the performance deviation of an energy storage system from ideality because of three inherent overpotentials: kinetic, ohmic or *iR*, and mass-transfer or concentration overpotentials. Ohmic overpotential arises from combined ionic resistivity of supporting electrolyte and membrane, and from electrical resistivity of electrodes. Total ohmic resistance was estimated by HFR measurements of the VRFB and was used to obtain *iR*-free polarization curves.

Figure 4.2 shows *iR*-free polarization curves of the cell assembly integrated with three channels: (a) CS, (b) SS and (c) SMS at varying electrolyte flow rates. The figure also shows variation of evaluated *iR*-free power density of the VRFB. The obtained results employing the CS channel are nearly same as reported in the literature [74] at similar flow rates. As *iR*-loss arising from ohmic resistances (membrane, electrolyte and electrodes) is excluded, the deviation of polarization curves from ideality (OCP = 1.51 V) arises from kinetic and mass-transfer overpotentials. At lower current densities, the deviation emanates from the slow electrode kinetics and the potential loss (kinetic overpotential) increases with increasing current density. The loss of potential at higher current densities is also contributed by mass-transfer overpotential resulting from transport of species from bulk electrolyte to the reaction sites.

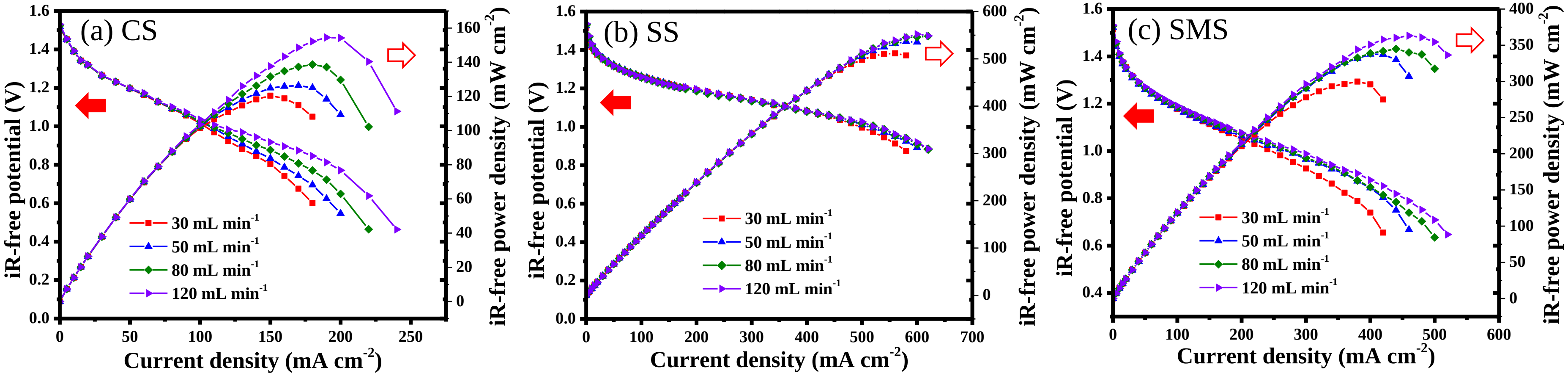

Figure 4.2. *iR*-free polarization curves and power density of VRFB at varying electrolyte flow rates in (a) CS, (b) SS and (c) SMS channels.

Suppose, j_{mtl} is the current density value at polarization curve where slope sharply increases, leading to mass-transfer control. The results presented in the figure illustrate that increasing flow rate increases j_{mtl}. For example, Figure 4.2(a) shows that in the VRFB with a CS channel, j_{mtl} is ~150 mA cm^{-2} at 30 mL min^{-1} and increases to ~200 mA cm^{-2} at 120 mL min^{-1}. The increased current density is achieved because of the enhanced convective mass-transfer occurring at higher flow rate or flow with higher Reynolds number. The corresponding values employing SS and SMS channels are ~500 and ~350 mA cm^{-2} at 30 mL min^{-1}, and ~500 and ~400 mA cm^{-2} at 120 mL min^{-1}, as evident from Figure 4.2(b) and 4.2(c). Figure 4.2(b) also shows that the obtained polarization curves at all flow rates of electrolyte in an SS channel closely follow each other indicating increasing flow rate has very little effect on the performance of the VRFB. The value of j_{mtl} is same at all flow rates. The highest current density of 620 mA cm^{-2} (where cell potential is zero) is achieved using the SS flow channel followed by SMS (520 mA cm^{-2}) and CS channels (240 mA cm^{-2}). Figure 4.2 also shows the effect of increasing flow rate of electrolyte on the power density of the VRFB. The power density increases with increasing flow rate. The effect is more evident for CS and SMS channels than a SS channel. The similar performance of VRFB in terms of j_{mtl} and peak power density, employing a SS channel, at increasing flow rates indicates that high mass-transfer and uniform electrolyte distribution can be achieved even at low flow rate. The polarization curves and power density, including *iR*-loss, of the cell assembly using these channels are shown in **Figure 4.3**. As *iR*-loss adds to the loss in potential, and thus lower power density is achieved. Here too, the effect of flow rate is not significant for the SS flow channel. **Figure 4.4** shows the effect of flow pattern on *iR*-free polarization curves and power density of the VRFB at same flow rate of electrolyte. The potential of the cell

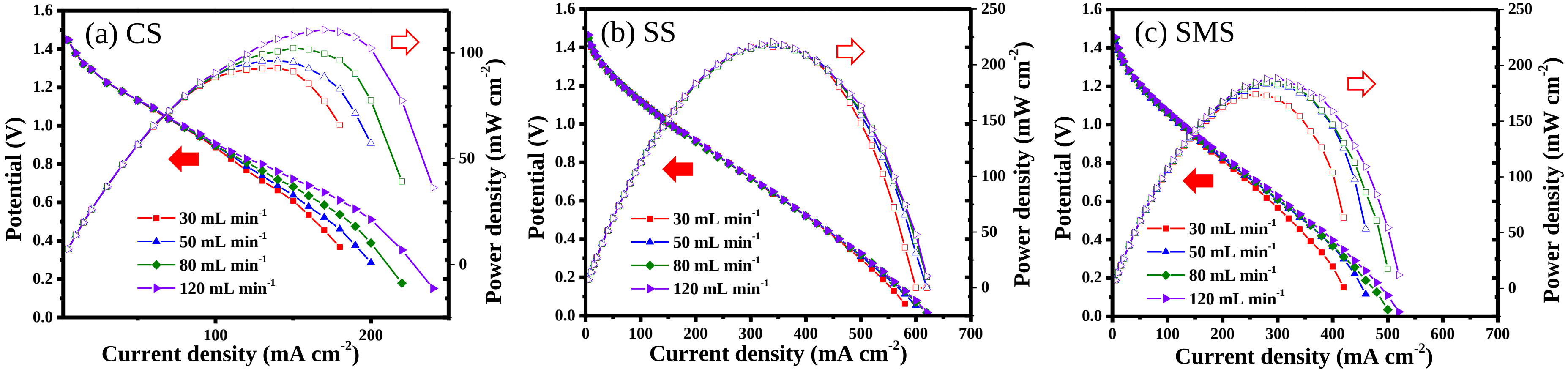

Figure 4.3. Polarization curves and power density, including *iR*-loss, of VRFB at varying electrolyte flow rates in (a) CS, (b) SS and (c) SMS channels.

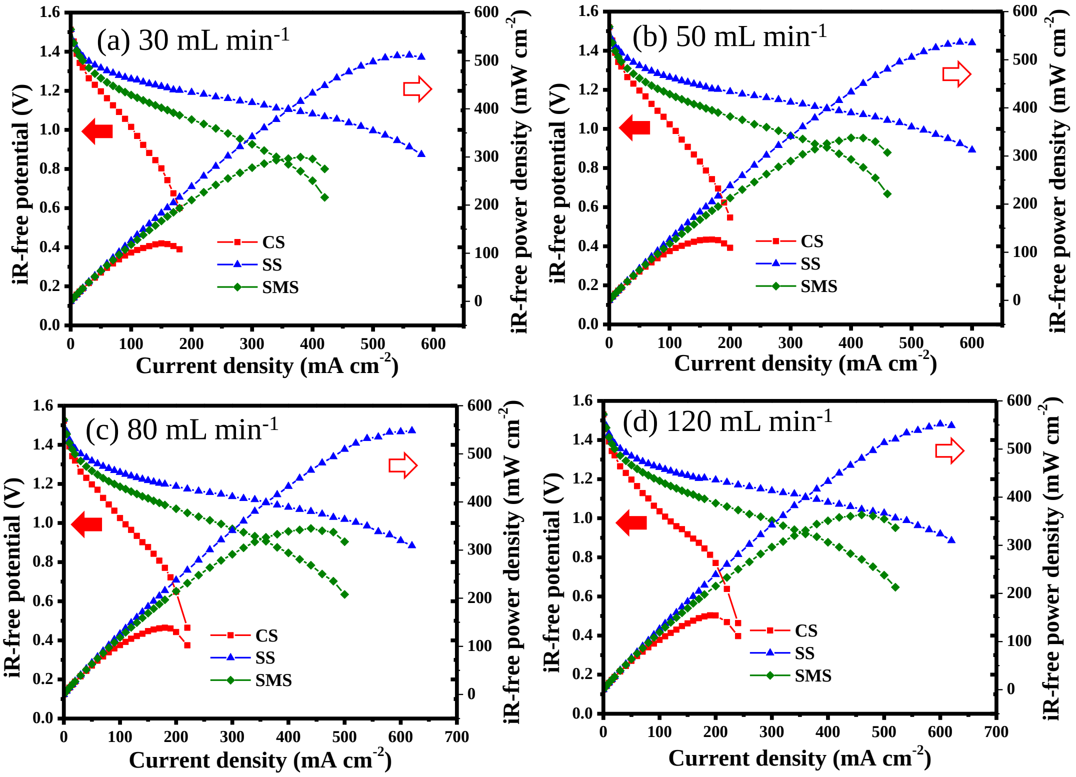

Figure 4.4. Comparison of *iR*-free polarization curves and power density obtained using three flow channels at same flow rate.

employed with the CS flow channel sharply decreases with increasing current density and the battery stops operation at ~200 mA cm^{-2}. The loss in potential is due to the kinetic and mass-transfer overpotentials is lower if SS and SMS channels are used. The SS channel causes lowest potential loss at all flow rates. Results presented in the figure show that 2 to 5 times higher current density can be withdrawn using SMS and SS channels at the same cell potential. For an example, at 1.0 V, current densities at 30 mL min^{-1} are: ~100, ~250, and ~500 mA cm^{-2}, respectively for CS, SMS and SS channels. Increasing flow rates improves the performance and values increase to: ~110, ~285, ~525 mA cm^{-2}, respectively, at 120 mL min^{-1}. The SS channel outperforms all, and potential loss across the battery does not deteriorate even after 500 mA cm^{-2}. The **Figure 4.5** also shows the comparison of obtained *iR*-free power density of VRFB using these channels at the same

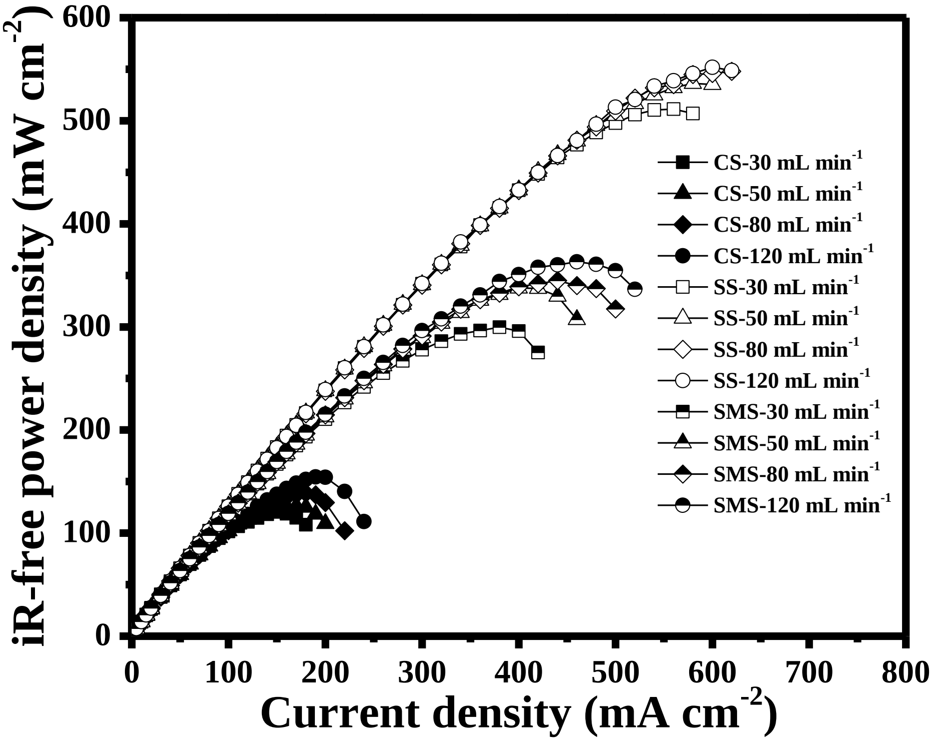

Figure 4.5. *iR*-free Power density of VRFB with (a) CS, (b) SS and (c) SMS channels at varying flow rates of electrolyte.

electrolyte flow rate. The extracted values of *iR*-free peak power density (P_{peak}), and corresponding current density (j_{peak}) and *iR*-free potential (V_{peak}) are presented in **Table 4.2**. The results illustrate that P_{peak} increases with increasing flow rate of electrolyte, and

Table 4.2. *iR*-free peak power density (P_{peak}), and corresponding peak current density (j_{peak}) and *iR*-free potential (V_{peak}) obtained at varying electrolyte flow in CS, SS and SMS flow channels. The data are extracted from Figure 4.4.

Flow rate (mL min^{-1}) / Peak Parameters	P_{peak} (mW cm^{-2})			j_{peak} (mA cm^{-2})			V_{peak} (V)		
	CS	SS	SMS	CS	SS	SMS	CS	SS	SMS
30	120	511	300	150	560	380	0.80	0.91	0.79
50	126	536	338	170	580	400	0.74	0.92	0.84
80	139	548	345	180	620	440	0.77	0.88	0.78
120	154	552	363	190	600	460	0.81	0.92	0.79

is highest (511 – 552 mW cm^{-2}) for SS channel followed by SMS (300 – 363 mW cm^{-2}) and CS (120 – 154 mW cm^{-2}) channels. The corresponding V_{peak} across the cell assembly with CS and SMS channels varies in the same range of 0.74 - 0.84 V (average value is ~0.80 V) while j_{peak} varies between [150, 190] mA cm^{-2} with the CS channel and between [380, 460] mA cm^{-2} for the SMS channel, which are ~2.5 times higher than for the former. With the SS channel, average V_{peak} value is ~0.91 V and j_{peak} varies between [560 – 600] mA cm^{-2}, highest of all the channels. Results show that the potential loss is the lowest and withdrawn current density is ~ 3.2 times higher compared to the CS channel. The values of P_{peak}, j_{peak} and V_{peak} including *iR*-loss were also extracted and are shown in **Figure 4.6**

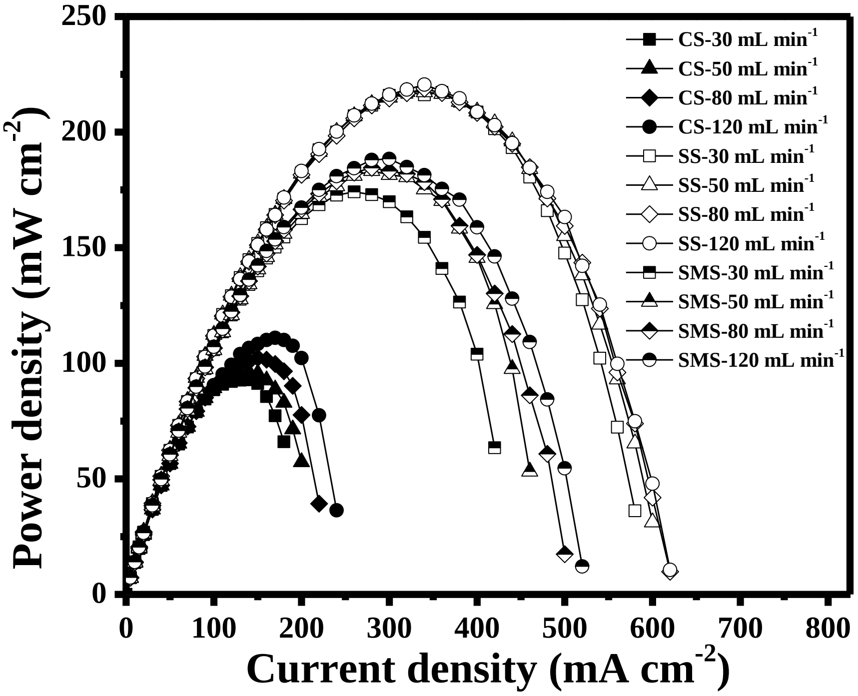

Figure 4.6. Power density of VRFB, including *iR*-loss term, with (a) CS, (b) SS and (c) SMS channels at varying flow rates of electrolyte.

and the results are presented in **Table 4.3**. The P_{peak} value decreases significantly with increasing *iR*-losses, still it is ~1.8 and ~2.2 times higher for SMS and SS channels, respectively, in comparison to the CS channel. The results also show that *iR*-loss inclusive

Table 4.3. Peak power density (P_{peak}, mW cm^{-2}), and corresponding peak current density (j_{peak}, mA cm^{-2}) and potential (V_{peak}, V) obtained at varying electrolyte flow in CS, SS and SMS flow channels. The data are fetched from Figure 4.3. All experiments were performed using 1 M $VOSO_4$/4 M H_2SO_4.

Flow rate (mL min^{-1}) / Peak Parameters	P_{peak} (mW cm^{-2})			j_{peak} (mA cm^{-2})			V_{peak} (V)		
	CS	SS	SMS	CS	SS	SMS	CS	SS	SMS
30	92.4	214	174	140	320	260	0.66	0.67	0.67
50	96.6	218	182	140	320	280	0.69	0.68	0.65
80	102	218	185	150	340	280	0.68	0.64	0.66
120	111	221	189	170	340	300	0.65	0.65	0.63

P_{peak} and V_{peak} are comparatively invariant with increasing flow rate. In conclusion, kinetics and mass-transfer losses are significantly lower in VRFB employed with newly designed, modified serpentine channels than the conventionally used channel. These findings are further investigated by performing EIS of the cell assembly.

4.3.2 EIS analysis of VRFB employed with fabricated channels

EIS is a powerful tool used in estimating kinetic, ohmic and mass-transfer resistances of an energy system. The kinetic resistance of the system stems from its resistive and capacitive nature which can be easily decoupled by EIS. This resistance dominates over ohmic and mass-transfer resistances when small current is withdrawn, and depends on the distribution of electrolyte in the porous structure of graphite felt. The EIS of the VRFB employing fabricated channels was performed by circulating electrolyte solutions at 30, 50, 80, and 120 mL min^{-1}. The voltage fluctuation is applied at low current value (0.1A, current density = 0.01A cm^{-2}) in all cases, indicating kinetic resistance will dominate. The obtained results of the VRFB employing CS, SS and SMS are presented respectively through **Figure 4.7(a)-4.7(c)** as Nyquist plots, which are depressed semicircles. The left intercept on the Z'-axis is HFR stemming from the combined effect of ohmic resistances

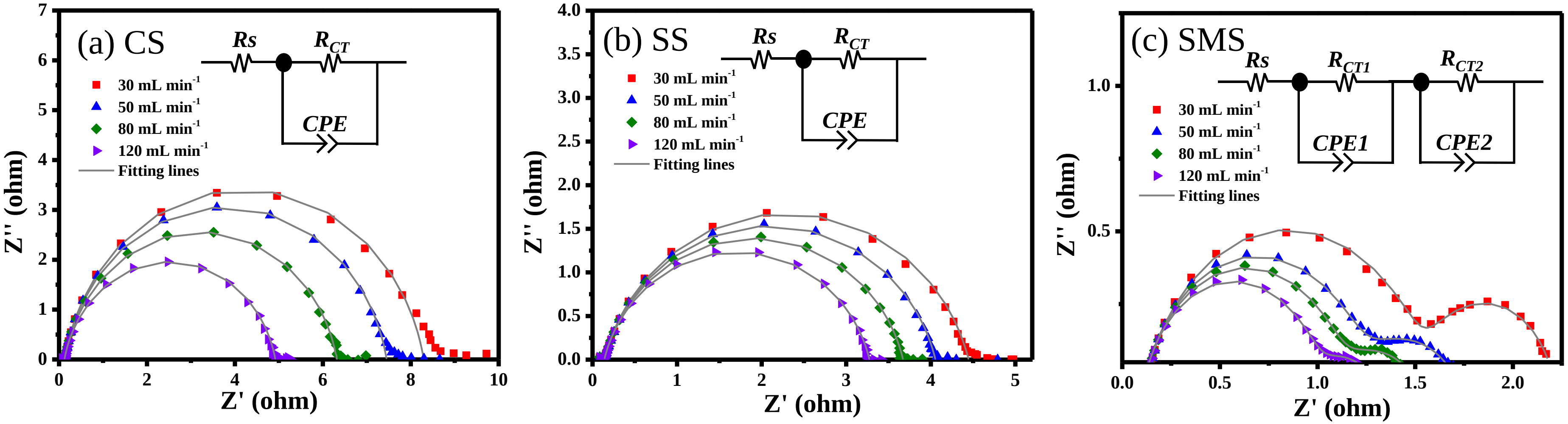

Figure 4.7. Electrochemical impedance spectroscopy of VRFB employed with (a) CS, (b) SS and (c) SMS channels at varying electrolyte flow rates. The equivalent electrical circuit is also shown. Its frequency response is presented by a fitting line.

of membrane, electrolyte solutions and electrodes. With decreasing frequency, the Nyquist plots obtained using CS and SS channels are depressed-semicircles and intercept the axis again. Small tails are observed at lower frequencies. The semi-circle characteristic represents capacitive nature and charge-transfer resistance of electrodes on both sides of the VRFB. These results indicate that the charge-transfer resistance of one of electrodes overwhelms the resistance of other. **Figure 4.7(c)** shows Nyquist plots obtained using the SMS channel and are two partially overlapping semicircles indicating comparable charge-transfer resistances of two electrodes. An equivalent circuit consisting of resistances and constant phase element for a porous electrode was modelled at each flow rate using inbuilt Zview software of the test station. The frequency response of the circuit was fitted with the experimental data. The fitting lines and the equivalent circuit are shown in the figures. The circuit parameters, R_s, R_{ct} and CPE, are ohmic resistance of electrolytes, charge-transfer resistance and constant phase element of porous electrode, respectively, and their values are provided in **Table 4.4**. Results presented in the table show that R_s values of the VRFB obtained from HFR are almost same (0.12 – 0.14 Ω): stemming from same material for electrodes and flow channels, from same electrolyte compositions and from same operating conditions; and showing no effect of flow pattern and electrolyte flow rate.

The plots presented in **Figure 4.7** show that the size of the semicircle decreases with increasing electrolyte flow rate in the channels indicating better charge-transfer kinetics. The estimated R_{ct} values presented in the table illustrate that the charge-transfer resistance decreases from 8.17 to 4.80 Ω for CS channel with increasing flow rate from 30 to 120 mL min^{-1}, and for SS channel it decreases from 4.45 to 3.26 Ω. In case of SMS channel, R_{ct} values, R_{ct1} and R_{ct2}, decrease from 1.43 to 0.87 Ω, and from 0.69 to 0.28 Ω, respectively.

Table 4.4. Equivalent circuit parameters, R_s, R_{ct}, *CPE-T* and *CPE-P*, of three flow channels estimated by fitting experimental EIS data. Circuits are shows in Figure 4.7.

Flow rate/ Circuit Parameters	30 mL min^{-1}			50 mL min^{-1}			80 mL min^{-1}			120 mL min^{-1}		
	CS	SS	SMS	CS	SS	SMS	CS	SS	SMS	CS	SS	SMS
R_s (Ω)	0.13	0.14	0.12	0.13	0.14	0.12	0.12	0.14	0.12	0.12	0.14	0.12
R_{ct}/R_{ct1} (Ω)	8.17	4.45	1.43	7.32	4.05	1.09	6.20	3.65	0.98	4.80	3.26	0.87
CPE-T/*CPE*1-*T*	0.01	0.01	0.02	0.01	0.01	0.02	0.01	0.01	0.02	0.01	0.01	0.02
CPE-P/*CPE*1-*P*	0.88	0.84	0.78	0.88	0.85	0.81	0.88	0.85	0.81	0.87	0.85	0.80
R_{ct2} (Ω)			0.69			0.49			0.39			0.28
*CPE*2-*T*			4.56			3.25			4.15			5.06
*CPE*2-*P*			0.80			0.57			0.51			0.52

The electrochemical behavior of a porous electrode is pseudo-capacitive and is characterized by constant phase element (CPE). The *CPE* values accounts for double layer capacitance. Double layer capacitance is also called non-faradaic current or double layer current. It does not involve any electrochemical reactions, it only occurs due to accumulation of charges at electrode-electrolyte interface which acts as a barrier to the flow of current. At lower currents, the potential losses occur in cell due to double layer capacitance. It consists of *CPE-T* and *CPE-P*, and corresponding impedance, Z_{CPE}, is defined as:

$$Z_{CPE} = \frac{1}{T(j\omega)^{1/P}} \tag{4.3}$$

The impedance is pure resistance if $P = 0$, is pure capacitance if $P = 1$, and is a CPE otherwise which shows depressed-semicircle characteristics on Nyquist plot. The magnitude of depression depends on the value of *P*. Results presented in **Table 4.4** show that its value (*CPE-P*/*CPE*1-*P*) lies between [0.78, 0.88] for all channels indicating CPE is more of a capacitive nature; there is a double layer formation at the electrode pore surface. The second semicircle appearing in low frequency zone for SMS channel is more depressed at higher electrolyte flow rates; illustrated by *CPE*2-*P* = 0.80 at 30 mL min^{-1}, and ~0.5 at higher flow rates. The increasing flow rate influence the pore-diffusion of electrolyte affecting the double layer. The impedance behavior is mixed, i.e. resistive and capacitive.

Table 4.4 also shows the effect flow pattern on the circuit parameters at same flow rate. The effect is also presented through varying size of semicircles of Nyquist plots in **Figure 4.8** for clarity. At all flow rates, the battery employed with CS channel shows highest charge-transfer resistance followed by SS and SMS channels. The results clearly indicate that better electrochemical kinetics can be achieved using SMS channel. On contrary, the polarization curves in **Figures 4.2** and **4.4** show that SS performs best among all channels followed by SMS and CS channels. For example, at same conditions, 5 times higher current density, compared to using the CS channel, can be withdrawn employing SS channel, and it is 2.5 times higher for SMS channel. These contrasting results point to the fact that these flow patterns have differences in their ability for allowing electrolyte to penetrate the porous electrode and for its distribution on electrode surface.

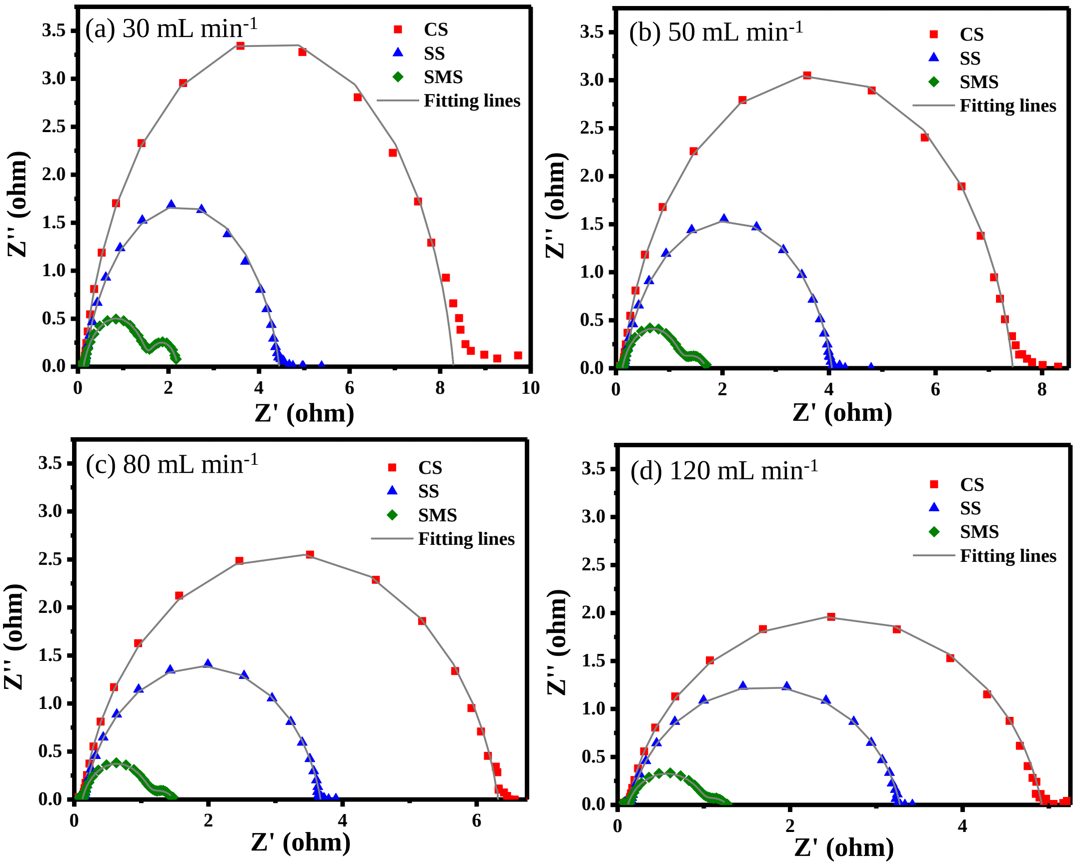

Figure 4.8. Electrochemical impedance spectroscopy of VRFB at (a) 30 mL min^{-1}, (b) 50 mL min^{-1}, (c) 80 mL min^{-1}, and (d) 120 mL min^{-1} showing effect of flow channels on resistance. Frequency response of an equivalent electrical circuits is presented by a fitting line.

The current density from the battery depends on cumulative effect of concentration of vanadium ions in channel and at electrode surface, convective mass-transfer coefficient, electrochemical reaction rate and area of electroactive surface in contact with the electrolyte. The path length for the electrolyte flow is nearly half for SS and SMS channels in comparison to CS channel (see Table 4.1). The flow volume splits at the entrance of the former channels and divided flows travel nearly half the distance of CS channel. This implies that the residence time of electrolyte in all channels is nearly the same. The electrochemical reactions occur on the surface of graphite plate in contact with electrolyte and in the pores of graphite felt. The active area of graphite plate (three surfaces of channel and surface of rib in contact with the electrolyte) is 18.29 cm^2, 17.81 cm^2 and 16.92 cm^2 for CS, SMS and SS channels, respectively; the lowest for the SS channel. Electrochemical reactions in the porous spaces of graphite felt electrodes occur where vanadium ions could reach via convective mass-transfer and diffusion. Thus the cumulative active area includes both, the area of graphite plate in contact with the electrolyte and the electrolyte-wetted porous area of the graphite felt. The apparent area of the electrode for the calculation of current density is taken as 10 cm^2. The corresponding current density (j_0) can be written as: $j_0 = j_0 ' A'/A$, where A is the apparent area, A' is the active surface area (graphite plate + felt) and $j_0 '$ is the corresponding current density (The value of $j_0 '$ for graphite plate and felt would be different, hence it can assumed as an area-averaged value. Further, it will depend on the electrochemical properties of electrode and electrolyte materials only, hence would be same for all channels.). Assume: $j_{0,CS}$, $j_{0,SMS}$, and $j_{0,SS}$ represent current density of the VRFB employing CS, SMS and SS channels, respectively. The ratios: $j_{0,SMS} / j_{0,CS} \approx 2.5$ and $j_{0,SS} / j_{0,CS} \approx 5$ imply that the SMS flow pattern helps accessing more than 2.5 times the porous spaces of the graphite felt in comparison to using a CS pattern. Using SS flow pattern, 5 times higher area of the electrode can be utilized. These results conclusively state that a better, uniform distribution of electrolyte on the porous electrode is achieved using SMS and SS channels than conventionally used serpentine channel in the flow battery.

4.4 Conclusions

Two new designs of flow pattern, Split Serpentine (SS) and Spilt-Merge Serpentine (SMS), are developed modifying the conventional serpentine (CS), aiming better distribution of electrolyte on porous electrode of a VRFB. The performance of these flow channels through characteristic polarization curves of cell assembly was evaluated at varying flow rates (30, 50, 80 and 120 mL min^{-1}) of fully charged positive and negative electrolytes at its respective side. The kinetic overpotential in each case was quantified using electrochemical impedance spectroscopy (EIS) measurements. Results show that increasing flow increases current and peak power densities, and mass-transfer limitations occur are at very high current. Operation of the battery keeping potential and flow rate constant shows that ~2.5 and ~5 times higher current can be withdrawn employing SMS and SS channels, respectively, in comparison to using a CS channel. Highest peak power density was achieved with the SS channel (552 mW cm^{-2}) followed by SMS (363 mW cm^{-2}) and CS (154 mW cm^{-2}) channels at 120 mL min^{-1}. EIS measurements show that the porous electrode with SMS channel has lowest charge-transfer resistance followed by with SS and CC channels; results are in contrast with the obtained trend of current density. The detailed analysis of all above results suggests that the SS flow pattern shows highest electrolyte distribution ability in porous electrode followed by SMS and CS channels. Even at as low as 30 mL min^{-1}, only 7.5% reduction in power density is observed employing SS channel. This reflects that better electrolyte distribution can be achieved at lower pumping cost. For applications of these designed flow patterns in a VRFB require a detailed study of charge-discharge cycle, estimating performance loss with cycle, and determining voltage, coulombic and energy efficiencies. These results will be included in the next article.

This page is intentionally kept blank

Chapter 5: Higher efficiency of a vanadium redox flow battery integrated with modified serpentine flow patterns

Abstract

In our previous work, we showed that higher power density of a vanadium redox flow battery is achieved employing modified serpentine flow channels – split serpentine (SS) and split-merged serpentine (SMS) – in comparison to a conventional serpentine (CS). In this work, coulombic efficiency (CE) and energy efficiency (EE) of the battery are estimated from discharge-charge cycles employing all channels at currents densities: 20 and 40 mA cm^{-2}, and at electrolyte flow rates of 50 and 100 mL min^{-1}. Results show that the highest potential is achieved employing a SMS channel, during initial period of discharging, but the potential drops steeply later. The battery with a SS channel takes longest discharge-charge time. Highest CE is achieved using SMS channel (95.2%) followed by SS (91.4%) and CS (82.2%) channels. The highest EE values for respective channels are: 77.4%, 73.6% and 60.1%. The efficiencies increase with increasing flow rates. The increasing current slightly improves the CE but adversely affects the EE of the battery. These results clearly illustrate that higher efficiencies can be achieved using modified channels, and an SMS channels outperforms all. Findings of this work will push towards application of these channels in other flow batteries.

5.1 Introduction

Storage of harvested energy from renewable energy sources, such as wind and solar, and their integration with grids can be successfully enabled through use of electrochemical energy storage systems [123]. One such potential system is vanadium redox flow battery (VRFB), which can be scaled up for requirements and can also help in peak shaving and supplying energy during peak energy demand [32,114,115]. A VRFB brings advantages, such as fast response time, negligible cross-contamination due to migration of ions, easy maintenance and prolong life-span and reusability, over other flow battery systems. Owing to its unique characteristics, it has been successfully implemented with wind turbine to stabilize output fluctuations of generated electricity [124,125]. A 60 MWh unit was installed in 2015 by Sumitomo Electric Industries Ltd. for its integration with electric grid [126].

VRFB is an electrochemical energy device, which helps in storing and supplying energy through electrochemical conversion of vanadium redox couples, V(II) ↔ V(III) at negative electrode, and V(III) ↔ V(IV) at positive electrode. Thus, it necessitates the use of positive (VO_2^+/VO^{2+}) and negative (V^{3+}/V^{2+}) electrolytes along with supporting electrolyte, stored in two separate tanks. The device consists of two half-cells, separated by a proton exchange membrane. Each cell has a porous electrode, a flow channel and an end-plate. The construction of the device can be found elsewhere [36,116]. The electrolyte solution stored in a tank is pumped to the respective half-cell. The flow channel helps it to diffuse into the porous electrode, where electrochemical reactions occur. Thus, power and capacity of a VRFB system can be independently scaled up – power depends on the active area of electrode and number of cells in a stack, and capacity depends on the electrolyte volume in the tank and its concentration [32].

One of major issues with a VRFB is non-uniform distribution of electrolyte over the porous electrodes leading to non-uniform current distribution and high mass-transfer resistance, and thus to reduced capacity and efficiency [32,99,110,118]. Two common arrangements, flow through and flow-by, are used to minimize the potential loss emanating from these issues [32]. The flow through arrangement does not require a flow channel, rather a porous electrode is placed in the cavity of the graphite plate. In flow-by arrangement, patterns are engraved on the plate, assisting the electrolyte to distribute over the electrode, and products to come out. Commonly used flow patterns include serpentine, interdigitated, parallel, and no-flow fields [65,72,74,105]. The performance of these flow paths vary with properties and types of electrode materials, electrolyte properties and operating conditions [71,106]. Weighing on the importance of optimizing the loss of potential, and thus, of enhancing capacity and efficiency of the battery, a well-designed flow channel is sought after which will help in fabrication of scaled-up VRFB systems for varied, desired applications.

A brief literature survey of theoretical and experimental studies on different flow patterns and their performance in battery and fuel cell systems is presented here. Xu et al. [63] investigated the performance of a VRFB numerically employing serpentine, parallel, and with no flow fields. Their results illustrate that there exists an optimal flow rate for each flow pattern to achieve maximum efficiency; the serpentine flow field exhibits highest energy efficiency (EE) and round trip efficiency. Later, this research group experimentally analyzed the performance of the battery with and without a flow field, and demonstrated that the a 5% higher EE can be achieved using a flow field [73]. Kumar et al. [74] through experimental findings compared the performance of serpentine, interdigitated, and with no flow field employing in a VRFB. Their results show that electrolyte flow rate significantly affects the performance, that the serpentine flow field provides the highest energy efficiency, attributed to lowest pressure drop and high voltaic efficiency, and that a round trip energy efficiency of ~80% can achieved at highest flow rate. Aaron et al. [60] demonstrated that a zero-gap architecture with serpentine flow field provides dramatic improvement in peak power density. The mass-transfer effect of serpentine, parallel, spiral and interdigitated flow fields investigated by Dennison et al. [85] illustrates that the performance of first three flow fields with perforated electrode improves up to 31% in comparison to the interdigitated channel. The findings were attributed to their better transport properties and greater area utilization of electrode. Maurya et al. [107] computed the energy efficiency of interdigitated, serpentine, and no-flow field with graphite felt electrode. Reported EE values for respective fields are: 55%, 64%, and 75%, which show that no-flow field provides highest efficiency owing to its better electrolyte distribution ability. Alyasiri and Park [89] developed a 3D model and validated with their experimental results, to unearth a relationship among efficiency of the battery, employing a serpentine channel, with electrolyte flow rate, state of charge, current density and channel height. Results show that increasing flow rates improve the EE of the battery and lower channel height provides better EE but at higher pumping cost. Ma et al. [110] investigated the effects of electrolyte flow rate on the performance of the fabricated a kilo-watt VRFB system and found that, at constant applied current density, the capacity of the battery increases, but efficiency decreases with increasing flow rates.

In the previous work, [127] we demonstrated that employing modified serpentine flow patterns, split serpentine (SS) and split-merged serpentine (SMS), with graphite felt electrodes, higher power density of the VRFB can be achieved, stemming from their better electrolyte distribution ability, and thus from higher electrode area utilization. The charge-transfer resistance of the device is lowest if employed with SMS channels, followed by SS and CS channels. However higher current can be withdrawn from the battery employed with SS channels, followed by SMS and CS channels. Results were attributed to highest electrolyte distribution ability of the SS channel, leading to highest area utilization of electrode. In this work, columbic, voltage and energy efficiencies – defining parameters of an energy storage device required for its usage in an application – of the battery employing modified channels are evaluated. The graphite felt electrode is used in the study. Discharge-charge cycles of the battery are performed at current densities of 20 and 40 mA cm^{-2}, and by varying electrolyte flow rates at 50 and 100 mL min^{-1}. Results show that higher efficiencies can be achieved employing these modified serpentine channels in a VRFB.

5.2 Experimental

Design and fabrication of flow channels - The details of design and fabrication of three flow patterns: (a) CS), (b) SS, and SMS, along with flow directions are provided in our earlier study,[127] and presented here in brevity. The photographs of the channels with details are given in **Figure 5.1**.

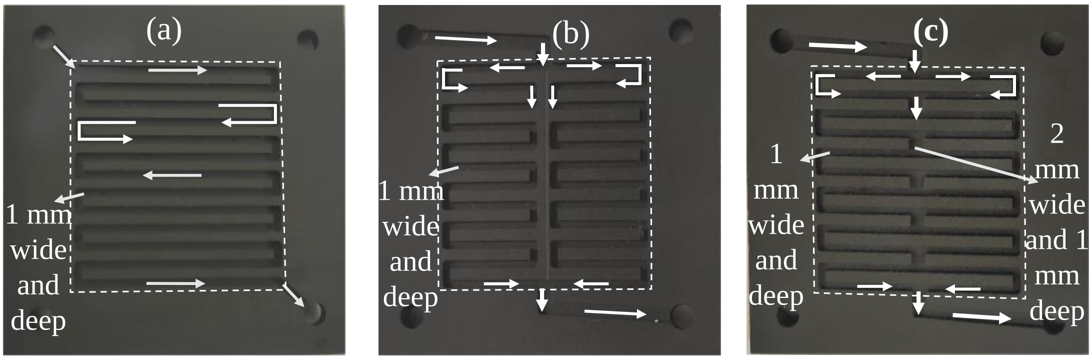

Figure 5.1. Photographs of fabricated flow channels: (a) CS, (b) SS, and (c) SMS. The dotted enclosure shows the area in contact with the electrode. Arrows indicate the flow direction in the channel.

The area, demarcated by dotted enclosure, is 10 cm^2, engraved on a 4-mm thick graphite plate. The electrolyte flow path, indicated by arrows, is 1 mm wide and 1 mm deep, except the midway path of the SMS channel is 2 mm wide. In CS channel, the path follows a single continuous route, from inlet to outlet, whereas inlet and outlet of SS and SMS channels are 2-mm wide which bifurcate into 1-mm-wide flow paths. The thus split flows in the SS channel follow their own, separate path, but the SMS channel allows the electrolyte to alternatively merge and split.

Membrane pretreatment and single-cell assembly - Nafion® 117 membrane (Alfa Aesar), which facilitates proton transport in the battery, is employed as a separator of two half-cells in the VRFB assembly. Before use, the membrane is treated by heating in 3% H_2O_2, followed by heating in deionized water, heating in 0.5 M H_2SO_4 (98.0%, SD Fine-Chem Limited, India), and finally heating in deionized water to remove excess acid [3,121,122]. The temperature at each step is maintained at 80°C.

The hardware of a single-cell VRFB, procured from Fuel Cell Store, USA, is reassembled using treated membrane and two symmetrical half cells, each consisting of a carbon felt electrode (uncompressed thickness of 6.35 mm, Alfa Aesar), a fabricated flow channel plate, a copper-current collector, an end-plate, and a 5 mm thick gasket. The electrode is used as received, without any pretreatment. The VRFB assembly is tightened following a standard crisscross sequential pattern, [74] leading to final compression of carbon felt electrode up to 32%. The contact resistance is measured using a digital multimeter (Fluke), and leakage test is performed by sequentially pumping distilled water and 4.0 M H_2SO_4 solution through both half cells of the assembly at varying flow rates: 30, 50, 80, 110, 150, and 180 mL min^{-1}. This also helps in washing out impurities from the cell, in hydrating the membrane, and in lessening the hydrophobic nature of the graphite felt electrode which is essential for the electrochemical reactions to occur in its porous spaces.

Preparation of electrolyte solutions by 2-step charging method - Positive and negative electrolyte solutions, each of 100 ml, are prepared by applying 2-step electrochemical conversion method, [61] on starting 300 ml solution of 1M vanadyl sulfate ($VOSO_4.xH_2O$, 97% purity, Sisco Research Laboratories Pvt. Ltd., India) dissolved in 4.0 M H_2SO_4 (Sulfuric acid, 96%, Sigma- Aldrich). This is accomplished by employing 857 Redox Flow Cell Test System, Scribner Associates, Inc. At each charging step, flow rate is maintained at 50 mL min^{-1}, and applied current density is kept at 40 mA cm^{-2} with cutoff potential, 1.80 V. The change in the oxidation state during the process is confirmed by characteristic colors: violet (V^{2+}), green (V^{3+}), blue (V^{4+}), and yellow (V^{5+}). The solutions in the tanks are continuously stirred and kept at room temperature. An inert environment in the tanks is maintained by continuous purging with nitrogen gas. After completion of charging process, open circuit potential (OCP) of the solutions is measured which is ~1.51 V.

Discharge-charge cycles - Two discharge-charge cycles of the fully charged electrolyte solutions are obtained, employing fabricated flow patterns (CS, SS or SMS) with fresh graphite felts in the VRFB, at current densities: 20 and 40 mA cm^{-2}. As the experiment is initiated by discharging the electrolyte, the cycle is named as 'discharge-charge' cycle. The cutoff potential for discharging step is set at 0.80 V and for charging at 1.80 V. At each current density, cycles are performed at electrolyte flow rates of 50 and 100 mL min^{-1}, in sequence. The experimental procedure follows: cleaning of vessels and connecting pipes; treatment of membrane; assembling VRFB components with a pair of similar flow channels; leakage test of the assembly; preparation of fully charged electrolyte solutions; and performing two discharge-charge cycles by pumping electrolyte at 50 mL min^{-1}, followed by at 100 mL min^{-1}. The efficiencies of the battery for each channel are estimated using charging and discharging steps.

5.3 Results and discussion

Discharge-charge analysis of VRFB: effect of electrolyte flow rate and current density - Deployment of an energy storage device for an application compels examination of its charge-discharge behavior, and evaluation of its efficiencies. **Figure 5.2** shows two cycles of discharge-charge profile of the VRFB, integrated with CS, SS, and SMS channels, obtained at 20 mA cm^{-2}, and with varying flow rates of electrolyte: 50 and 100

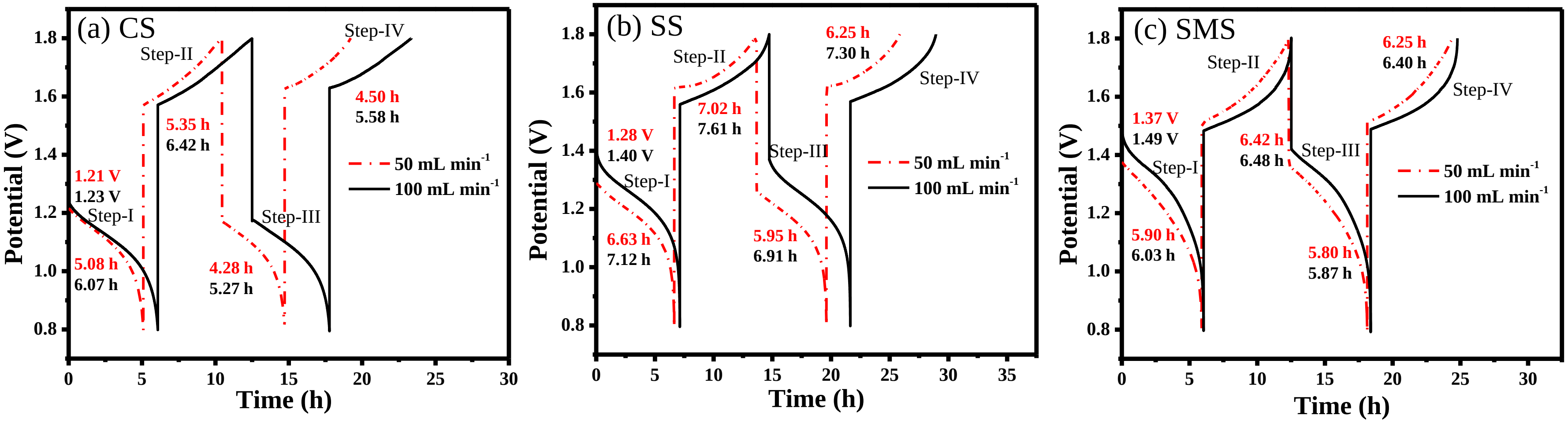

Figure 5.2. Discharge-charge cycles obtained by employing (a) CS, (b) SS and (c) SMS channels in VRFB. Current density is 20 mA cm^{-2} and electrolyte flow rates are: 50 (red, dotted lines) and 100 mL min^{-1} (black solid lines). Steps – I and III are discharging profiles, and Steps II and IV are charging profiles. Initial potentials (V) of Step – I and discharge-charge time (h) at respective steps are mentioned for electrolyte flow rates: 50 mL min^{-1} (red) and 100 mL min^{-1} (black).

mL min^{-1}. The overpotential during charging and discharging is the manifestation of kinetic, ohmic and mass-transfer polarizations, and depends on various parameters such as electrode kinetics, ionic conductivity of electrolyte, electrolyte flow rate, state of charge of electrolyte, type of employed flow pattern, electrolyte distribution in porous electrode, and applied current density. The figure shows that during discharge, there is a sudden drop in initial cell potential from 1.51 V (OCP of fully charged electrolyte). The measured initial potentials of the VRFB employing CS, SS and SMS channels, at discharge current density of 20 mA cm^{-2} and at electrolyte flow rate of 50 mL min^{-1}, are: 1.21, 1.28, and 1.37 V, which increase to: 1.23, 1.40, and 1.49 V, respectively, at 100 mL min^{-1}. This potential loss is due to kinetic and ohmic overpotentials only, no contribution of mass-transfer as concentration is uniform in the wetted pores. Moreover, the ohmic resistance (~0.13 Ω) of the battery is almost invariant with electrolyte flow rate and types of flow pattern, but R_{ct} depends on them: it decreases with increasing flow rates and is highest with the CS channel, followed by SS and SMS channels [127]. This elucidates the effect of flow path and flow rate on the variation of initial potential loss. These findings can also be, alternatively, explained mathematically through Butler-Volmer (BV) equation [66].

Initially, the concentration of electrolyte is same everywhere in the porous electrode and in channel. Assuming symmetrical potential energy curves for electrochemical reactions at cathode and anode, the B-V equation for current, i, can be simplified as:

$$i = i_{0,c} \sinh(f|\eta_c|) = |i_{0,a}| \sinh(f\eta_a), \tag{5.1}$$

where, $i_{0,c}$ and $i_{0,a}$ are exchange currents at cathode and anode, η_c and η_a are respective initial kinetic overpotentials, and $f = F/RT$ with f, R and T representing Faraday constant, universal gas constant and temperature, respectively. The exchange current inversely depends on charge-transfer resistance – higher the value of R_{ct}, lower the value of i_0. Thus, Eq. 5.1 clarifies that, at constant current, higher R_{ct} value of the battery results in higher overpotential. Similar behavior of rise in initial potential is observed while charging the solution.

Figure 5.3 shows discharge-charge cycles along with initial potentials obtained at current density 40 mA cm^{-2} and with varying electrolyte flow rates at 50 and 100 mL min^{-1}. The measured initial potentials of the battery employed with CS, SS and SMS channels at electrolyte flow rate of 50 mL min^{-1}, are: 1.13, 1.23, and 1.29 V, which increase to: 1.16, 1.32, and 1.38 V, respectively, at 100 mL min^{-1}. Comparing values obtained at 20 mA cm^{-2}, results indicate that the initial potential loss also changes with current density. To understand the effect of current density on kinetic and ohmic overpotential. An electrochemical impedance spectroscopy measurement is performed on the VRFB employed with CS channel at 10 and 100 mA cm^{-2}, and at flow rate of 50 mL min^{-1}. Results are presented in **Figure 5.4**. The EIS data are fitted by ZView, and equivalent circuits and circuit parameters are provided.

At lower current, anodic and cathodic kinetic resistances overlap, while at higher current, the data demonstrate two depressed half circles. Increasing current density from 10 to 100 mA cm^{-2}, the total ohmic resistance increases from 0.13 to 0.17 Ω, while total R_{ct} of electrodes decreases from 7.32 to 4.97 Ω, which is consistent with the findings of Sun et al. [128]. The increase in the former resistance can be attributed to higher conversion of vanadium ions at higher current, and decrease in the latter resistance is due to faster kinetics. The combined effect of these resistances at higher current contribute to

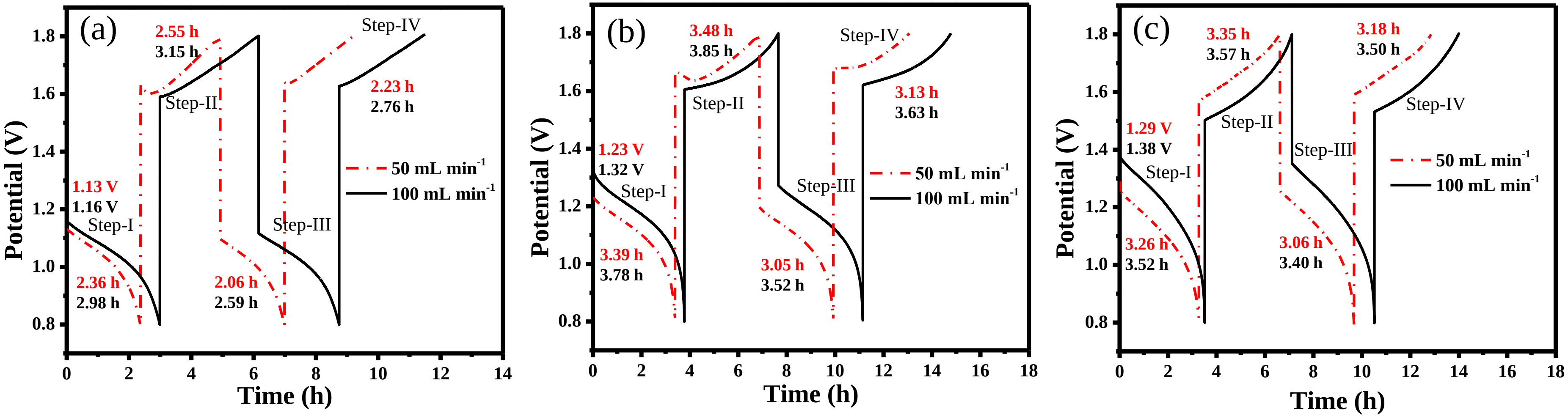

Figure 5.3. Discharge-charge cycles obtained by employing (a) CS, (b) SS and (c) SMS channels in VRFB. Current density is 40 mA cm^{-2} and electrolyte flow rates are: 50 (red, dotted lines) and 100 mL min^{-1} (black solid lines). Steps – I and III are discharging profiles, and Steps II and IV are charging profiles. Initial potentials (V) of Step – I and discharge-charge time (h) at respective steps are mentioned for electrolyte flow rates: 50 (red) and 100 mL min^{-1} (black).

initial loss of potential. Clearly, the loss is lower with SMS channel, followed by SS and CS channels.

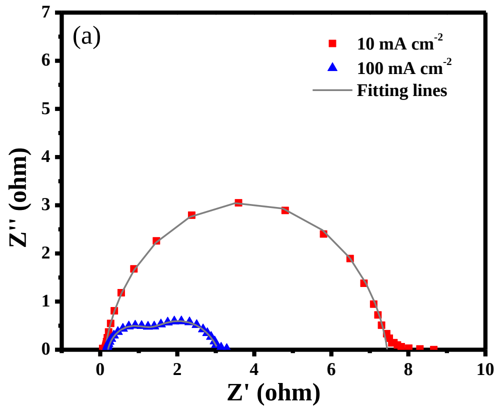

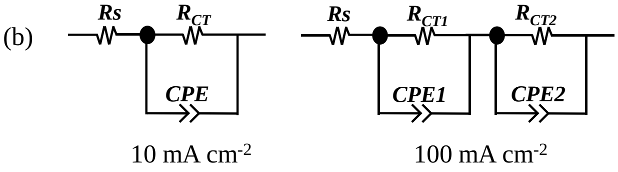

(c)

Flow rate/ Circuit Parameters	50 mL min^{-1}	
	10 mA cm^{-2}	100 mA cm^{-2}
R_s (Ω)	0.13	0.17
R_{ct}/R_{ct1} (Ω)	7.32	1.41
CPE-T/*CPE*1-*T*	0.01	0.02
CPE-P/*CPE*1-*P*	0.88	0.79
R_{ct2} (Ω)		3.56
*CPE*2-*T*		0.13
*CPE*2-*P*		0.42

Figure 5.4. (a) Nyquist plots obtained at withdrawn current densities of 10 and 100 mA cm^{-2}, by performing EIS measurements of the battery integrated with CS channel with electrolyte flow rate of 50 mL min^{-1}. The figure also shows the fitting lines, (b) Equivalent electrical circuit of the battery at 10 and 100 mA cm^{-2}, (c) The circuit parameters are provided in the table. R_s = ohmic resistance (solution + membrane + electrode), R_{ct} = charge-transfer resistance and *CPE* = constant phase element.

Results show that R_s value slightly increases with increase in current, attributed to change in concentration of electrolyte. There is significant decrease in R_{ct} values at higher current, leading to enhanced kinetics. At 10 mA cm^{-2}, R_{ct} value of one side of electrode overlaps over that of the other side, but at 100 mA cm^{-2}, they are distinguishable.

Results presented in **Figures 5.2** and **5.3** also show the continuous decrease in cell potential with time, while discharging, until it reaches the cutoff potential of 0.8 V, and, while charging, it increases up to cutoff potential of 1.8 V. Four steps, Step – I to IV, indicated in the figures correspond to discharging profiles (Steps – I and III) and charging profiles (Steps – II and IV). Time taken at each step is also mentioned at varying flow rates: 50 (indicated by red) and 100 mL min^{-1} (indicated by black). As current is fixed, the respective time represents extent of discharge and charge of electrolytes – longer the time, longer operational capability of VRFB and its higher energy storage capacity. Results illustrate that the discharge-charge time depends on flow rate, flow pattern and applied current density. It increases with increasing flow rates. The effect of flow rate is more substantial for CS channel than for SS and SMS channels. These findings can be attributed to better distribution and higher penetration of electrolyte in porous electrodes at increased flow rate, and by employing modified channels. At 20 mA cm^{-2}, discharge-charge time of the electrolyte employing (refer respective step) SS channel is highest followed by SMS and CS channels. For example, in Step – II, time taken, employing these channels is: [7.02 h, 6.42 h, 5.53 h], respectively, at 50 mL min^{-1}. The total time in two discharge-charge cycles is: [25.85 h, 24.37 h, 19.21 h] at 50 mL min^{-1}, and [28.94 h, 24.78 h, 23.34 h] at 100 mL min^{-1}, respectively. At 40 mA cm^{-2}, the time for SS and SMS channels in respective discharging and charging steps is close, but higher than for a CS channel. The total time in two discharge-charge cycles by employing SS, SMS and CS channels is: [13.05 h, 12.85 h , 9.20 h] at 50 mL min^{-1}, and [14.78 h, 13.99 h, 11.48 h] at 100 mL min^{-1}, respectively. These results demonstrate that doubling the current, discharge-charge time of electrolyte is $< \frac{1}{2}$, $\approx \frac{1}{2}$, and $> \frac{1}{2}$ for CS, SS, and SMS channel, respectively. This indicates improved efficiency of the battery at higher current if employed with modified channels. A comparison of discharge-charge cycles at varying electrolyte flow rate and current density is presented in **Figure 5.5**. The figure illustrates that during discharging, the cell potential steeply decreases for SMS channels (and also for a CS channel) than for a SS channel, although initial potential is higher in the former.

This can be attributed to the better electrolyte distribution and higher electrode area utilization employing a SS channel [127].

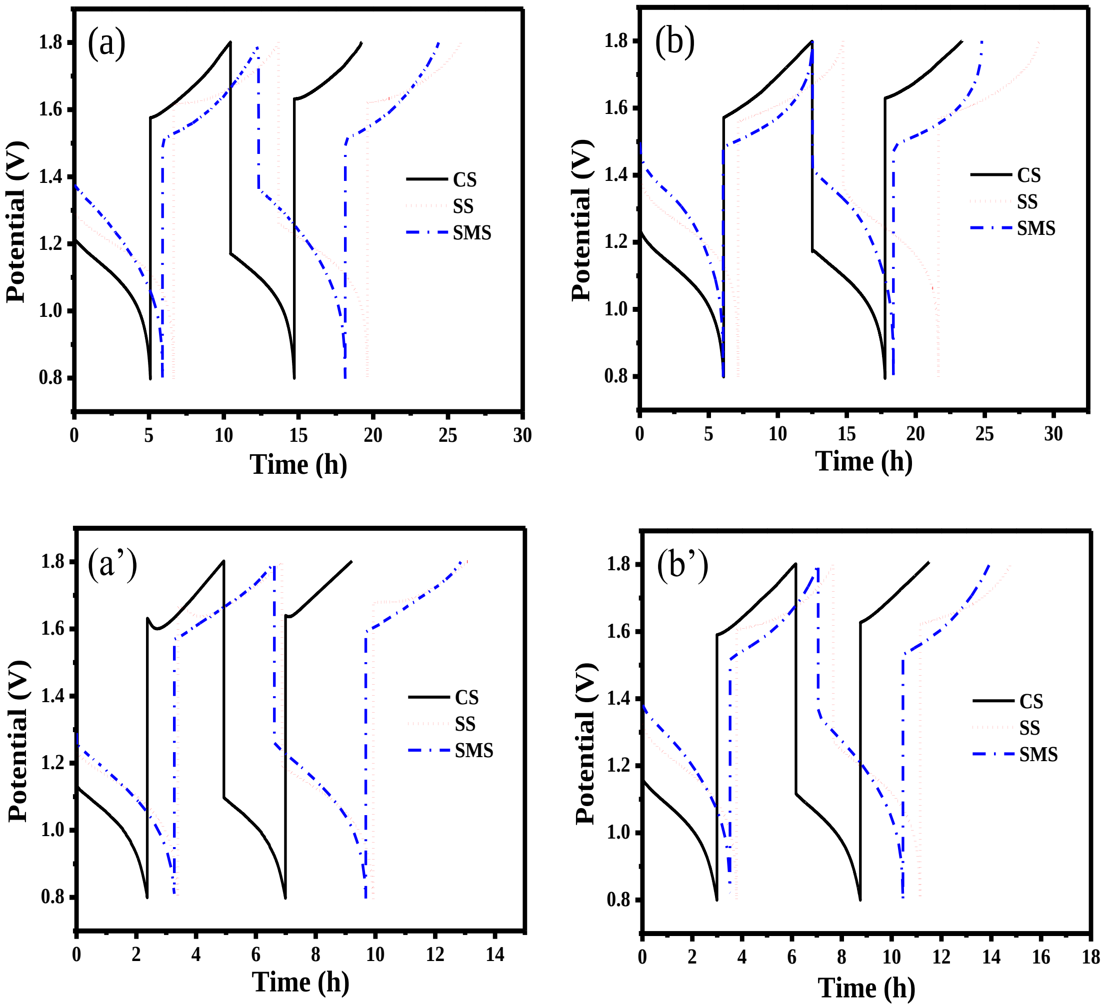

Figure 5.5. Discharge-charge cycles obtained employing CS, SS and SMS channels in the VRFB at applied current density of 20 mA cm^{-2} and electrolyte flow rates at (a) 50 mL min^{-1} (b) 100 mL min^{-1}, and applied current density at 40 mA cm^{-2} and electrolyte flow rates at (a') 50 mL min^{-1} (b') 100 mL min^{-1}.

Table 5.1 presents the initial potential at Steps – I to IV extracted from **Figures 5.2** and **5.3**. Results show that the potential of charging or discharging steps varies with flow rate, current density, and number of cycles, indicating electrolyte does not attain the same state of charge. It increases with increasing flow rates while discharging, but decreases when charging. A comparison of values at Steps – I and III shows that, at constant electrolyte flow rate and current density, the initial potential of discharging steps decreases with number of cycles, and it increases in charging steps (see values for Steps – II and IV) – indicative of loss of efficiency.

Table 5.1. Initial potential of discharging and charging steps, obtained employing CS, SS and SMS channels in VRFB, measured at electrolyte flow rates of 50 and 100 mL min^{-1} and at current densities of 20 and 40 mA cm^{-2}. Steps – I and III are for discharging, and Steps – II and IV are for charging, as shown in Figures 5.2 and 5.3.

Flow pattern	Discharge-charge step	I	II	III	IV	I	II	III	IV
	Flow rate	Potential (V) at 20 mA cm^{-2}				Potential (V) at 40 mA cm^{-2}			
CS	50 mL min^{-1}	1.21	1.57	1.17	1.63	1.13	1.63	1.09	1.64
	100 mL min^{-1}	1.23	1.57	1.18	1.62	1.16	1.59	1.11	1.62
SS	50 mL min^{-1}	1.28	1.61	1.26	1.62	1.23	1.65	1.19	1.67
	100 mL min^{-1}	1.40	1.55	1.36	1.56	1.32	1.6	1.27	1.62
SMS	50 mL min^{-1}	1.38	1.51	1.37	1.51	1.29	1.56	1.27	1.59
	100 mL min^{-1}	1.49	1.48	1.42	1.48	1.38	1.51	1.35	1.53

Efficiency of VRFB: effect of flow pattern – The efficiency of an energy system is evaluated in terms of columbic efficiency (CE), voltage efficiency (VE), and energy efficiency (CE) using following equations [69,129,130]:

$$CE = \frac{\int_0^{t_d} I_d dt}{\int_0^{t_c} I_c dt} \times 100\%; = \frac{\int_0^{t_d} V_d dt}{\int_0^{t_c} V_c dt} \times 100\% \; ; EE = \frac{\int_0^{t_d} V_d I_d dt}{\int_0^{t_c} V_c I_c dt} \times 100\%, \tag{5.2}$$

where, I_d = discharging current, I_c = charging current, t_d = discharge time, t_c = charge time, V_d = discharging potential, and V_c = charging potential. Since I_d and I_c are constant, the above relations reduce to:

$$CE = \frac{t_d}{t_c} \times 100\% \; ; \; EE = VE = \frac{\int_0^{t_d} V_d dt}{\int_0^{t_c} V_c dt} \times 100\%. \tag{5.3}$$

Thus, CE indicates the efficiency of harvesting the stored charge in the electrolyte using VRFB, and is calculated by the ratio of discharging time to charging time. The EE refers to the ratio of harvested energy from the battery to the energy spent in storing it which, in this case, is equal to VE, i.e. ratio of average potential during discharging and charging. Loss of efficiencies (< 100%) of an energy storage device is due to current leakage, crossover of vanadium ions through the membrane, side reactions occurring on electrodes and internal resistances [68,131,132].

Values of CE and EE of the VRFB, employing CS, SS and SMS flow channels, are determined using profiles in Steps – II and III of **Figures 5.2** and **5.3**, and are presented in **Table 5.2**, demonstrating effect of flow pattern, current density and electrolyte flow rate. Results show that efficiencies for SS and SMS channels are higher than for a CS channel. The CE value improves by 8-10% and EE by 10-17%. Efficiencies for an SMS channel is slightly higher than that for an SS channel. A general trend follows: CE and EE values increase with increasing electrolyte flow rate, irrespective of flow channel and applied current density. At the same flow rate, the CE value for a channel slightly improves with increasing current density, whereas EE value decreases. For example, at 50 mL min^{-1}, CE values for CS, SS and SMS channels are: [80.0, 84.8, 90.3] at 20 mA cm^{-2}, respectively, which marginally increase to: [80.8, 87.6, 91.3] at 40 mA cm^{-2}. The EE values are: [56.5, 64.0, 73.5] at 20 mA cm^{-2}, and [55.6, 62.3, 64.5] at 40 mA cm^{-2} for respective channels. Similar trend for dependency of efficiencies on flow rate and current density are reported elsewhere [107]. The increasing current although speeds up crossover of vanadium ions through the membrane, main reason for coulombic efficiency to be < 100%, [132] it also allows lesser time for crossover during a cycle – resulting in the higher

Table 5.2. Coulombic efficiency (CE) and energy efficiency (EE) of a VRFB, employed with CS, SS and SMS channels, calculated from its discharge-charge cycles, obtained at 20 and 40 mA cm^{-2} and at electrolyte flow rates of 50 and 100 mL min^{-1}.

Flow pattern	Current density = 20 mA cm^{-2}				Current density = 40 mA cm^{-2}			
	CE (%) @ 50 mL min^{-1}	CE (%) @ 100 mL min^{-1}	EE (%) @ 50 mL min^{-1}	EE (%) @ 100 mL min^{-1}	CE (%) @ 50 mL min^{-1}	CE (%) @ 100 mL min^{-1}	EE (%) @ 50 mL min^{-1}	EE (%) @ 100 mL min^{-1}
CS	80.0	82.1	56.5	60.1	80.8	82.2	55.6	56.7
SS	84.8	90.8	64.0	73.6	87.6	91.4	62.3	67.6
SMS	90.3	90.6	73.5	77.4	91.3	95.2	64.5	73.3

CE values [3,107,133]. On the contrary, the higher current leads to higher overpotentials, and thus, to lower EE values. Higher efficiency values of the battery employed with SMS channels can be attributed to the lesser difference in discharge-charge time and lower average internal resistance (or lower overpotential) experienced by the device. The results presented in **Table 5.2** show that the coulombic efficiency can be achieved as high as 95% and energy efficiency up to 77% using modified channels, whereas, for a CS channel, maximum values are ~82% and ~60%, respectively. The respective efficiencies for the CS channel are slightly lower that the reported values, [~95, ~85], determined at 40 mA cm^{-2} and 40 mL min^{-1} [107]. The higher reported efficiencies might be due to use of thinner electrode (4.6 mm vs. 6.3 mm in the present study), pretreatment of electrode, smaller amount of electrolyte in reservoir, and difference in method of preparation of fully charged electrolyte solutions. Findings further illustrate that although SS channels help in achieving better distribution of electrolyte in the porous electrodes, [127] higher efficiencies are achieved employing SMS channels.

5.4 Conclusions

The presented work is the extension of our earlier studies on modified serpentine channels, split serpentine (SS) and split-merged serpentine (SMS); employing them in a vanadium redox flow battery (VRFB) helps in obtaining its enhanced power density than using a conventional serpentine (CS) channel. The application of these flow patterns in the device mandates evaluation of their performance in terms of columbic efficiency (CE) and energy efficiency (EE). The experimental procedure follows thorough analysis of discharge-charge cycles, obtained by varying electrolyte flow rates at 50 and 100 mL min^{-1} and at applied current densities of 20 and 40 mA cm^{-2}. Results show that the highest initial potential, while discharging, is achieved employing a SMS channel, but the potential drops steeply later. The highest discharge-charge time of the electrolyte is achieved with a SS channel. The effect of flow rate on the time is least for a SMS channel. The estimated CE value is highest for SMS channel (95.2%), followed by SS (91.4%) and CS (82.2%) channels at 40 mA cm^{-2} and 100 mL min^{-1}. The maximum EE values employing these channels are: 77.4% (SMS), 73.6% (SS) and 60.1% (CS) at 20 mA cm^{-2} and 100 mL min^{-1}. Results further illustrate that the increasing flow rates improve CE and EE values for all channels, but higher current has opposing effect. These findings conclusively suggest that modified channels are superior to a CS channel, and of all, SMS channel helps in achieving higher performance of the battery.

The EE value of the channels has been estimated without taking into account of the energy required for pumping the electrolyte in these channels which will vary with flow pattern. Our future scope of work includes estimation of pressure drop and pumping power, and study of electrolyte distribution, velocity distribution and concentration gradient in channels through numerical simulation.

This page is intentionally kept blank

Chapter 6: Energy efficient flow path for improving electrolyte distribution in a vanadium redox flow battery

Abstract

Aiming to improve electrolyte distribution in flow batteries at lower pumping cost, sinusoidal wave-type serpentine (SWS) flow pattern was designed and fabricated on graphite plate. The performance of the channel with graphite felt electrode, employing in vanadium redox flow battery, was analyzed by polarization curves and electrochemical impedance spectroscopy (EIS) measurements, obtained at varying flow rates. The pressure drop of the half-cell assembly was measured by varying water flow rates. Discharge-charge cycles of the battery were performed at 50 and 100 mL min^{-1}, and at current density: 20 and 40 mA cm^{-2}. Results show that increasing flow rate reduces potential loss. Mass-transfer overpotential is low even at 30 mL min^{-1}, and at 120 mL min^{-1}, the overpotential is negligible even at current density, 500 mA cm^{-2}. The *iR*-free power density monotonically increases with current density. The EIS measurements show that charge-transfer resistance decreases with flow rate and is lower than that for conventional serpentine flow pattern. The pressure drop across the cell is also lower. These results clearly indicate that better electrolyte distribution is achieved using SWS channels at lower pumping cost. The coulombic efficiency > 91%, and energy efficiency of ~73% were achieved.

6.1 Introduction

Recent focus on reduction of carbon footprint by using renewable energy sources, such as wind and solar, and strengthening the infrastructure to harvest energy from these resources have provided impetus to the development of efficient electrical energy storage systems, which can be integrated to the power grid. This can be achieved by an electrochemical energy storage device such as flow batteries [44,123]. Vanadium redox flow battery (VRFB) is one of the most promising and fast-growing technologies, owing to its easily scalable energy storage and power capacity, fast response time and easy maintenance [32,114,115]. The use of vanadium salts in the battery significantly eliminates contamination of electrolytes due to migration of ions and prolongs its life cycle. The battery has progressively been used for various applications, and is commercially viable [124–126].

VRFB consists of two tanks and a cell assembly. Tanks contain acidic electrolyte solution of vanadium ions – V (IV)/V(V) in positive tank, and V(II)/ V(III) in negative tank. A cell is made up of two symmetrical half cells, each consisting of a porous electrode, a flow channel and a current collector, and partitioned by proton conducting membrane. Electrolyte from the tank is pumped to the respective side of the cell, where electrochemical conversion of vanadium ions during charging and discharging occurs:

$$\text{Positive side: } VO^{2+} + H_2O \xrightleftharpoons[\text{Discharging}]{\text{Charging}} VO_2^{+} + 2H^{+} + e;\ E^0 = 1.00V \tag{6.1}$$

$$\text{Negative side: } V^{3+} + e \xrightleftharpoons[\text{Discharging}]{\text{Charging}} V^{2+};\ E^0 = -0.26V \tag{6.2}$$

A detailed schematic of the device and its operation can be found elsewhere [36,116]. The storage of energy is quantified by amount of electrolyte in the tank and its state of charge, and power of the battery is determined by the area of the electrode available for the reactions. The unique features of independently decoupling energy capacity and power capacities, and of alleviating cross-contamination of electrolytes due to use of vanadium ions separate it from other energy storage devices [32,51,134–136].

Graphite felt electrode is commonly employed as electrode in a VRFB which is porous and provides a large surface area for electrochemical reactions. A complete process leading to surface reactions consists of multiple steps: mass-transfer of electroactive species from channel to the pores of electrode, reactions at the surface, and removal of formed products from pores for surface renewal [32]. This necessitates efficient and uniform distribution of electrolyte in the porous spaces. Graphite plate engraved with flow pattern is employed to transport electrolyte for reactions. The non-uniform distribution of electrolyte in pores leads to underutilization of the electrode, and thus to the loss of performance and efficiency of the battery [99,110]. Very few designs of flow patterns have been investigated for VRFB, and similar energy devices, to address the issue of electrolyte maldistribution [94]. Frequently used patterns are: serpentine, interdigitated, parallel, and spiral. The performance of a flow pattern depends on channel geometry, electrode properties and operating conditions [89,105,107,110,111,119,120]. Zhao and coworkers [63,73] through their experimental and numerical investigation illustrated that flow fields help in achieving higher energy efficiency of the battery in comparison to when no flow field is employed, and a serpentine flow pattern is found to be superior to other patterns. Jayanti and his group through hydrodynamic studies showed that the interdigitated pattern allows lesser pressure drop across the cell than using a serpentine channel, owing to smaller residence time in the former [65]. On the contrary, in their other work, the group reported that employing serpentine channel in VRFB, a higher energy efficiency can be achieved at the cost of lower pressure drop than with interdigitated and no-flow fields [74]. Their results show that the performance of the battery depends on electrolyte flow rate, and at the highest flow rate, a round trip efficiency of ~80% was attained using serpentine flow field. They also examined the effect of channel dimension on VRFB of larger areas and recommended wider serpentine channel to obtain better performance [111]. Tsushima et al. [120] examined the effect of channel geometry and operating parameters on VRFB performance with serpentine and interdigitated flow fields. Their results show that the latter performs better, both with carbon felt and carbon paper electrodes. Aaron et al. [60] demonstrated a zero-gap architecture of the battery employing serpentine flow field with stacked sheets of carbon paper, achieving a peak power density of 557 mW cm^{-2}. Houser et al. [71,106] illustrated that a cumulative effect of design of a flow pattern, properties of electrode, and operating conditions have influence on the performance of a VRFB. Interdigitated flow field with thin electrodes performs better at lower electrolyte flow rates, and at higher flow rates, it performs similar to a serpentine channel. Denninson et al. [85] examined mass transport effect of serpentine, parallel, spiral and interdigitated flow fields with perforated carbon paper electrode and illustrated that interdigitated channel is 31% less efficient than other channels. Xu et al. [73] through 3D numerical modelling of a VRFB demonstrated superiority of serpentine flow field over parallel and conventional flow fields.

In our earlier work [127,137], we investigated the performance of two modified serpentine flow patterns, split serpentine (SS) and split-merged serpentine (SMS), in comparison to the conventional serpentine (CS) flow pattern employed with carbon felt electrode in a VRFB. Results show that higher current can be withdrawn, and higher coulombic and energy efficiencies can be achieved, using modified channels, owing to better distribution of electrolyte. The current article presents a sinusoidal wave-type serpentine (SWS) flow pattern. The objective of this design is to increase electrode area utilization for enhanced kinetics, but at lower pumping cost. The performance of the battery employed with the SWS channels was analyzed by polarization curves and electrochemical impedance spectroscopy measurements, obtained at varying flow rates of electrolyte, ranging from 30 to 120 mL min^{-1}. The ohmic resistance contribution was subtracted from polarization curves to examine contribution from kinetics and mass transfer polarizations. The pressure drop across the half-cell set up was measured by varying water flow rates. Discharge and charge cycles were performed to determine efficiency of the battery. Results show that higher *iR*-free power density can be obtained employing this channel in comparison to a CS channel. The coulombic efficiency above 90% and energy efficiency of ~73% are obtained. These findings are attributed to better distribution of electrolyte and higher area utilization of electrode at lower pumping cost, employing SWS channel.

6.2 Experimental

6.2.1 Fabrication of sinusoidal wave-type serpentine (SWS) flow channels

Figure 6.1 presents AUTOCAD design of the flow channel along with the inset figure for the magnified section, and engraved flow pattern in 10 cm^2 area of graphite plate, demarcated by the dotted rectangle, along with flow directions. As illustrated in the inset

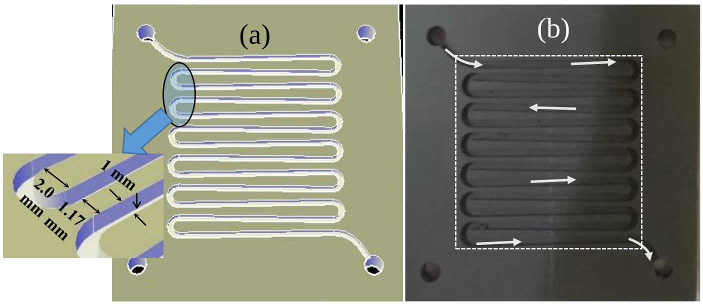

Figure 6.1. Sinusoidal wave-type serpentine (SWS) channel. (a) AUTOCAD design of channel along with magnified section as an inset, and (b) photograph of the fabricated channel. Channel is engraved on graphite plate of thickness 4 mm with channel dimensions: 1 mm wide and 1 mm deep. The bending gap is 2.0 mm, and the distance between the two channels is 1.17 mm. The arrows denote the electrolyte flow path in the channel. The engraved area, indicated by a white dotted rectangle, is ~10 cm^2.

figure, the bending gap of the channel is 2.0 mm, and distance between two bends is 1.17 mm; this provision allows electrolyte, while approaching a bend, to progressively climb up. The flow path visibly looks sinusoidal in nature; the design aims to provide increased coverage of porous electrode with electrolyte at lower pumping cost, in comparison to the conventional serpentine one. The channel has equal depth and width of 1 mm. The path length was measured using a thread and is 416 mm, same as for the CS channel [127].

6.2.2 Membrane pretreatment and single-cell construction

Nafion® 117 membrane (Alfa Aesar), which is acidic and proton conductive in nature, is employed. The membrane was treated at 80 °C for 1 hour sequentially in 3% H_2O_2 solution, deionized water, and 0.5 M H_2SO_4 (98.0%, SD Fine-Chem Limited, India) solution, and finally in deionized water, as reported in literature [3,121,122].

A single-cell VRFB hardware, procured from Fuel Cell Store, of area 10 cm^2 was reassembled employing the treated membrane, with each side having a carbon felt electrode (uncompressed thickness of 6.35 mm, Alfa Aesar) placed in the cavity of a gasket, an SWS flow channel plate, and a current collector. The assembly was tightened, achieving 32% compression. The contact resistances between the cell components were checked using a digital multimeter (Fluke). The leakage test of the assembled cell was performed by circulating distilled water followed by 4.0 M H_2SO_4 solution on both sides of the battery at varying flow rates: 30, 50, 80, 110, 150, and 180 mL min^{-1}. This step also enables in washing out of the impurities, in membrane hydration required for its proton conduction, and in alleviating hydrophobicity of graphite electrode.

6.2.3 Preparation of electrolyte solutions using two-step charging method

Positive and negative electrolyte solutions, each of 100 ml, were prepared by 2-step electrochemical conversion method from starting solution of 1.0 M $VOSO_4.xH_2O$ (97%, Sisco Research Laboratories Pvt. Ltd., India) dissolved in 4.0 M H_2SO_4, employing 857 Redox Flow Cell Test System, Scribner Associates, Inc. The details of the preparation method are presented in our previous studies [127,137] and in other literature [61]. The electrolyte flow rate was maintained at 50 mL min^{-1}. A constant current density of 40 mA cm^{-2} was applied at each step with cutoff potential of 1.80 V. Electrolyte tanks were blanketed from environment by continuously purging with nitrogen gas. The open circuit potential (OCP) of the prepared solutions was ~1.53V.

6.2.4 Polarization curve and electrochemical impedance spectroscopy (EIS) measurements

The polarization curves of fully charged positive and negative electrolyte solutions were obtained at 30, 50, 80, and 120 mL min^{-1} using the test system. The solutions were discharged for 30 s at a constant current density followed by 2 min rest. The average potential of last 20 s is taken, eliminating the time for double layer charging. The applied current density was varied by 5 mA cm^{-2} until the potential reaches at zero value, indicating maximum possible current. The obtained curves were modified by subtracting ohmic or iR-loss, and was determined using high-frequency response (HFR). The HFR measurement helps in estimation of net internal ohmic resistance of the device, and its multiplication with current, i.e. iR is the corresponding potential loss.

The EIS measurement of the battery, employed with the SWS channels, was carried out in the frequency range: [0.001 Hz, 10 kHz], at varying flow rates of electrolytes. The sinusoidal perturbation of 10 mV was applied at 0.01 A cm^{-2}.

6.2.5 Measurement of pressure drop

Pressure drop in the half cell of the system, with and without graphite felt, employing CS and SWS channels was measured by varying water flow rates: 10 – 120 mL min^{-1}. A schematic of experimental set-up is provided in **Figure 6.2**. An assembly of half-cell with

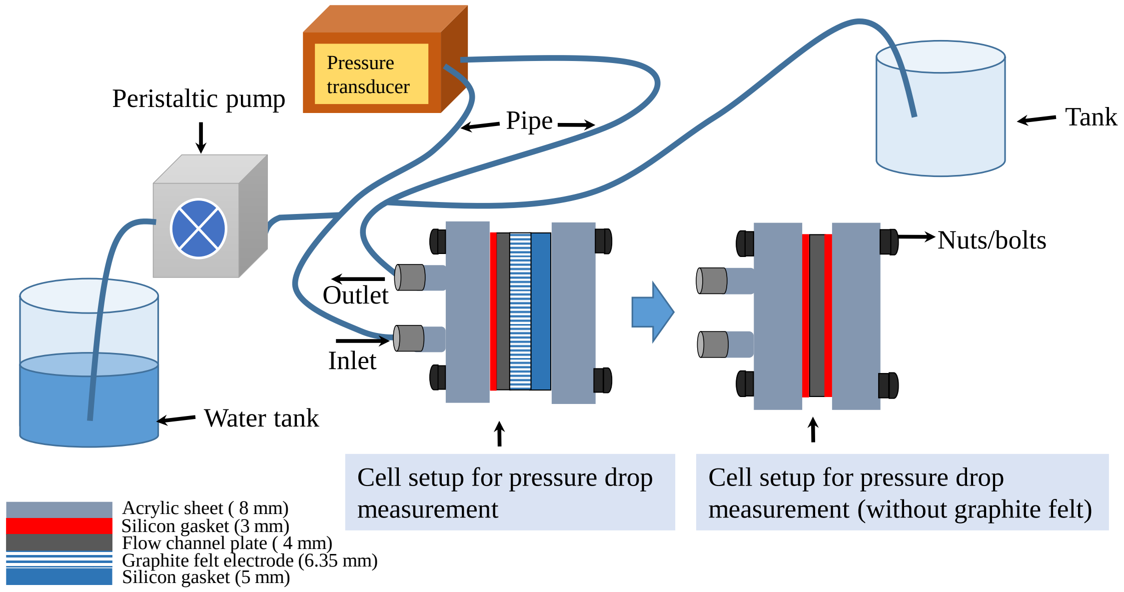

Figure 6.2. Schematic of experimental setup for pressure drop measurement in channels using pressure transducer.

felt has a channel plate, a 5 mm thick silicon gasket with square opening of 10 cm^2, in which a 6.35 mm thick graphite felt is placed, and a silicon gasket (60 mm × 60 mm × 3 mm) – all sandwiched between two acrylic sheets of dimensions 102 mm × 102 mm × 8 mm. The assembly was tightened up to compression of 32%. Its inlet and outlet ports were connected to a pressure transducer (Honeywell ST 700) using T-joints. The transducer measures the pressure difference of the system between two joints. The pressure drop in the cell was estimated by subtracting the effect of pipes at inlet and outlet, and 90° bending of flow. The assembly without felt is a similar set up but without 5 mm thick gasket and felt.

6.2.6 Discharge-charge cycle measurements

The performance of the VRFB, assembled with the SWS channels, was diagnosed by obtaining two discharge-charge cycles at applied current densities of 20 and 40 mA cm^{-2}. At each current density, positive and negative electrolyte solutions prepared from fresh VOSO$_4$.xH$_2$O salt were used. The effect of varying electrolyte flow rates (50 and 100 mL min^{-1}) on the cycles was also analyzed. The cutoff potential of discharging step was set at 0.80 V, and for charging step, it was 1.80 V.

All electrochemical measurements were carried out at room temperature employing 857 Redox Flow Test Station.

6.3 Results and discussion

6.3.1 Polarization curves of VRFB employed with fabricated SWS channels

The polarization curve of any energy device demonstrates variation of its potential with current, and the deviation from ideality (open circuit potential, OCP) shows the loss of potential arising from three overpotentials: kinetic, ohmic or *iR*, and mass transfer – predominant in low, mid and high current density domains, respectively. The kinetic overpotential stems from slow anodic and/or cathodic reactions. Electrical resistivity of electrodes, contact resistances, and ionic resistivity of supporting electrolytes and membrane lead to the ohmic overpotential. The mass transfer overpotential in VRFB originates from the cumulative effect of mass transfer resistance of electroactive species in channel flow and sluggish pore diffusion in graphite felt. **Figure 6.3** shows the effect of electrolyte flow rate on polarization curves and power density of the VRFB assembled with SWS channels. To compare these findings, best performance of a CS channel obtained at 120 mL min^{-1}, previously reported, [127] is also presented in the figure. The dotted horizontal line is the open circuit potential (OCP) of the battery. Thus, the gap between a polarization curve and OCP line is a measure of total potential loss, or potential expense, of the battery at a current density. Results illustrate that increasing flow rate helps shift the polarization curve in the upward direction, indicating decrease in the loss. Consequently, a higher current can be withdrawn from the battery at constant potential by increasing electrolyte flow. For example, at 0.8 V, current density values are 160, 170, 180 and 200 mA cm^{-2} at 30, 50, 80, and 120 mL min^{-1}, respectively. In comparison, the battery with a CS channel, at electrolyte flow rate of 120 mL min^{-1}, provides current density of 130 mA cm^{-2}. This clearly shows that the SWS channel is superior, even at 30 mL min^{-1}, to a CS channel operating at 120 mL min^{-1}.

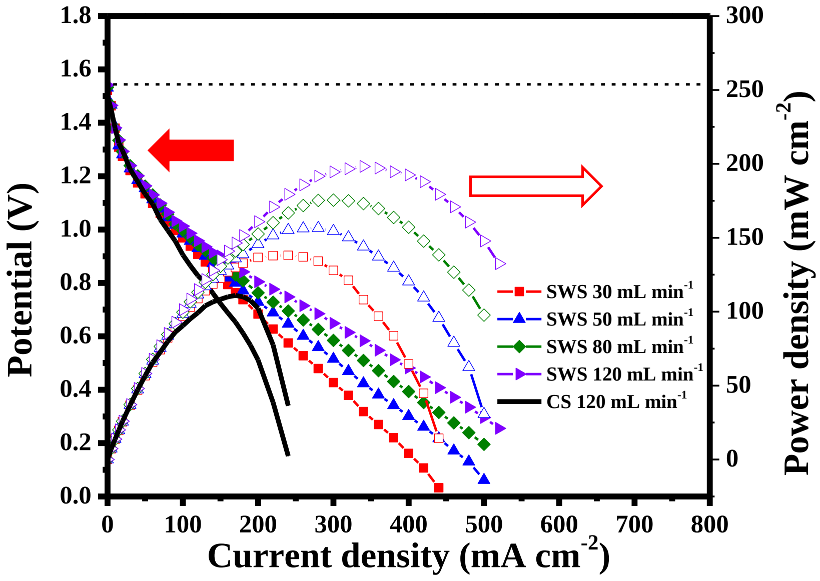

Figure 6.3. Polarization and power density curves of the VRFB with SWS channels obtained by varying electrolyte flow rate. Curves with CS channels are presented by black solid lines for comparison [127]. The black dotted line is the OCP curve measured at the start of the polarization curve measurements.

Polarization and power density curves of the VRFB with SWS channels obtained by varying electrolyte flow rate. Curves with CS channels are presented by black solid lines for comparison [127]. The black dotted line is the OCP curve measured at the start of the polarization curve measurements.

The results shown through **Figure 6.3** do not clearly differentiate the effect of flow rate and type of channel in low current regions. For better illustration, potential versus current density data, extracted from the figure, at varying flow rates are presented in

Table 6.1. Results show that at low current densities, for example at 20 mA cm^{-2}, the increasing flow rates help in reduction in potential loss only up to 20 mV, but has a substantial effect at higher currents. For example, if current density is increased to 150 mA cm^{-2}, cell potential is 0.81 and 0.90 V at 30 and 120 mL min^{-1}, respectively; an advantage of 90 mV. This clearly reflects that the loss of potential, or overpotential, in the the battery decreases with increasing flow rate. As evident from the presented results, only at lower current density value of 20 mA cm^{-2}, SWS and CS channels demonstrate a similar performance at higher flow rates, i.e. 120 mL min^{-1}. The potential of battery using CS channels falls steeply with increasing currents; the SWS channel even at 30 mL min^{-1} performs better than with CS channel at 120 mL min^{-1}. Above results emphasize the fact that in the kinetics limiting regions, flow rate and type of channel have a little effect on the performance of the battery, but at higher current density, where the effect of ohmic and mass transfer is significant, they exhibit a constructive role. The deteriorating performance of the battery can be significantly alleviated using SWS channels in comparison to using CS channels.

Table 6.1. Variation of cell potential with current density and electrolyte flow rates, extracted from Figure 6.3.

Current density (mA cm^{-2})	Potential (V)				
	30 mL min^{-1}	50 mL min^{-1}	80 mL min^{-1}	120 mL min^{-1}	CS channel @ 120 mL min^{-1}
20	1.27	1.28	1.29	1.29	1.29
50	1.13	1.15	1.16	1.16	1.13
100	0.96	0.98	0.99	1.01	0.90
150	0.81	0.85	0.87	0.90	0.72
200	0.68	0.72	0.76	0.80	0.51
360	0.27	0.38	0.47	0.54	-

Figure 6.3 also presents the variation of power density – defined as current density x cell potential – of the battery with increasing currents and flow rates. The results

show that the peak power density increases with increasing flow rates and shifts towards higher current values. For example, the peak power densities of 138, 156, 175, and 198 mW cm^{-2} are achieved at 30, 50, 80, and 120 mL min^{-1}, respectively, at corresponding current densities: 240, 280, 300, and 340 mA cm^{-2}. With CS channels, the value is 111 mW cm^{-2}, at 120 mL min^{-1}. This illustrates that the power density of the battery with modified channel is 2-3 times higher than with the conventional serpentine channel. Findings presented above require systematic investigation to delineate the role of flow channels and flow rates for improving the performance of the battery which can be accomplished only through evaluating the contribution of kinetic, ohmic and mass transfer overpotentials, and is provided in the following sections.

6.3.2 Estimation of overpotentials by EIS and analysis of iR-free polarization curves

To distinguish and estimate three internal resistances of the battery, EIS measurements of the fully charged solutions were performed by withdrawing low current (0.1 A, equivalent current density = 10 mA cm^{-2}) at varying flow rates. The results are presented in **Figure 6.4** as Nyquist plots, which have two intercepts at Z' axis: left one represents the HFR or ohmic resistance, and the right one is the combination of HFR and the resultant charge transfer resistance of positive and negative electrodes, obtained at low frequency. With decreasing frequency, the plots show depressed semicircles, which are a characteristic of an energy device with porous electrode, stemming from constant phase element; revealing its pseudo-capacitive and resistive behavior. The diameter represents magnitude of charge transfer or kinetic resistance. Results in the figure clearly indicate that the kinetic resistance of the battery employed with SWS channels decreases with flow rates, and is lower than with CS channels. The values of ohmic and kinetic resistances, and of constant phase element were determined by fitting the obtained curves using ZView software. The equivalent circuit is presented in the figure, as an inset. The regressed values of circuit elements are provided in **Table 6.2**. For comparison, the values for the CS channels are also provided.

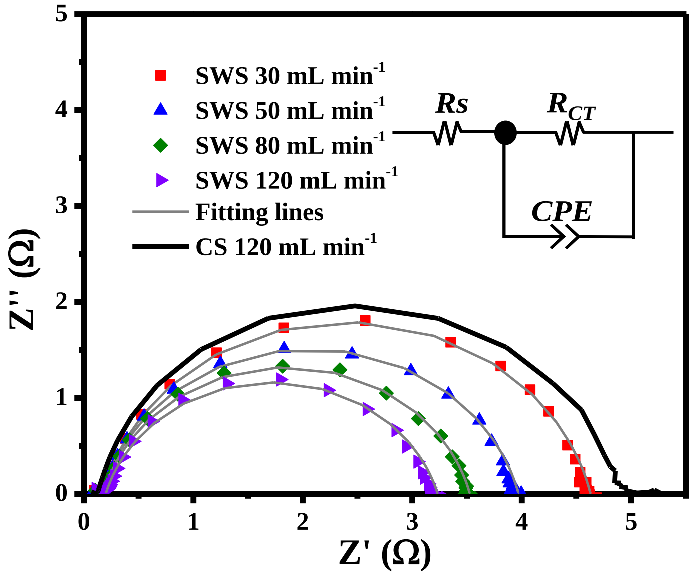

Figure 6.4. Electrochemical impedance spectroscopy (EIS) data obtained by varying flow rate of electrolyte in VRFB coupled with SWS channel. The EIS data are fitted using ZView software and are presented by thin solid lines. The equivalent electrical circuit is presented as inset. The thick black line is EIS curve with CS channel at 120 mL min^{-1} [127]. The values of circuit elements are presented in Table 6.2.

Table 6.2. Equivalent circuit parameters, R_s, R_{ct}, *CPE-T* and *CPE-P*, estimated by fitting EIS data by ZView software. Circuit is shown in Figure 6.4 as inset. Circuit parameters with a CS channel (last row) at 120 mL min^{-1} are also provided for comparison [127].

Flow rate mL min^{-1}	Equivalent circuit elements			
	R_s (Ω)	R_{ct} (Ω)	*CPE-T*	*CPE-P*
30	0.18	4.60	0.01	0.86
50	0.17	3.96	0.01	0.85
80	0.18	3.52	0.01	0.85
120	0.18	3.20	0.01	0.83
120 (CS)	0.12	4.80	0.01	0.87

The symbols, R_s, R_{CT} and *CPE,* represent ohmic resistance, charge transfer resistance and constant phase element, respectively. Results presented in the table indicate that R_s values, obtained at high frequency, of the battery with SWS channels are almost invariant with electrolyte flow rate, and is ~0.18 Ω. This value is slightly higher than that for CS channels (0.12 Ω), and also that for SS and SMS channels, for which it was 0.12 – 0.14 Ω [127]. As the major contribution to R_s arises from ohmic resistance of the membrane (Nafion), thus the slight variation in R_s values can be assigned to change in electrolytic conductivity during the measurements. The R_{CT} value decreases with increasing flow rates: at 30 mL min^{-1}, it is 4.60 Ω, which decreases to 3.20 Ω at 120 mL min^{-1} for SWS channels. However, the value is 4.80 Ω for CS channels, obtained at 120 mL min^{-1}. This indicates that the kinetics of porous graphite felt electrode gets better with an SWS channel than using a CS channel.

The porous electrode shows pseudo-capacitive behavior, emanating from combined effect of diffusion of electroactive ionic species in pores and electrochemical phenomena occurring at the surface, and is represented by *CPE,* having two components: *CPE-T* and *CPE-P*. The corresponding impedance, Z_{CPE}, is mathematically represented as: $Z_{CPE} = \frac{1}{CPE-T(jw)^{1/CPE-P}}$. The value of *CPE-P* reflects impedance characteristics of the battery: *CPE-P* = 0, the impedance is pure resistive (no semicircle); *CPE-P* = 1, the impedance is pure capacitive (perfect semicircle); and *CPE-P* = (0, 1) shows depressed circle – the magnitude of depression depends on its value. The *CPE-P* values presented in **Table 6.2** are ~0.85, which reflects more of capacitive behavior of the battery, emanating from double layer formation in the pores of graphite felt electrode.

The obtained values of R_s are used to eliminate the contribution of ohmic overpoential from the curves (**Figure 6.3**) to obtain *iR*-free polarization and power density curves at varying flow rates, and are presented in **Figure 6.5**. The thus obtained former curve demonstrates the deviation of cell potential from OCP value, ~1.53 V, stemming from kinetics and mass transfer polarizations. Results in the figure elucidate that up to current density value of 100 mA cm^{-2}, increasing flow rates have no significant effect on polarization curves if battery is employed with SWS channels. This shows that mass transfer polarization is negligible, even at low flow rate, and potential loss incurs mainly due to kinetic overpotential. At higher current density, the potential loss increases with current density, only if the battery is operated at lower electrolyte flow rates. At high flow rate, i.e. 120 mL min^{-1}, overpotential is almost constant up to current density as high as 500 mA cm^{-2}. Contrastingly, the steep slope of the polarization curve for CS channels at low current density of 100 mA cm^{-2} indicates early onset of mass transfer polarization. The above result of low potential loss, or ovepotential, by increasing flow rates of electrolyte, and by preferring SWS to CS channels, is directly related to higher electrode

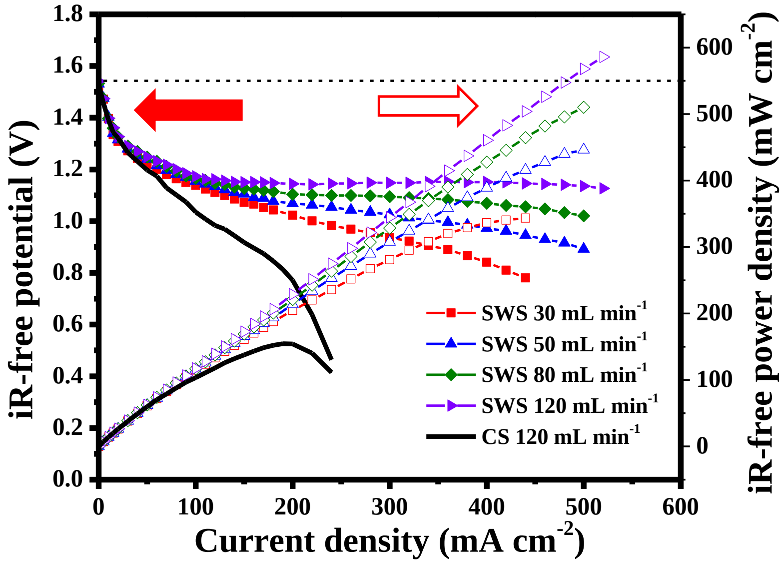

Figure 6.5. Effect of varying electrolyte flow rate on *iR*-free polarization curves, obtained by subtracting ohmic overpotential from OCP (black dotted line), and *iR*-free power density curves of VRFB with SWS channels. Curves with CS channels are presented by black solid lines for comparison [127].

area utilization, and is discussed in the later section in detail. The effect of varying flow rates and current densities on *iR*-free power density of the battery employing the channels is also presented in the figure. Results show that *iR*-free power density monotonically increases with current density, up to experimental limit, and with flow rate. The values of *iR*-free power density of the battery, using SWS channels, are higher than using CS channels at a given flow rate and current density. In fact, the values are higher than even using split serpentine (SS) and split-merged serpentine (SMS) channels [127].

6.3.3 Discussion on the results – higher area utilization of electrode area using SWS channels

The engraved flow path on the graphite plates helps in distribution of liquid electrolyte in the porous spaces of graphite felt electrodes which, as result, increases the effective area utilization. Ionic conductivity of membrane is negligibly affected by the flow pattern. In all experiments in this study, the same cell set-up is used; only variation is allowed in flow rate and in current density. The current density values in all above figures and tables are based on apparent area of electrode, 10 cm^2. The actual active area is the electrolyte-wetted area, where reactions occur. Suppose, *A* and *A'* are apparent and actual areas, and *j* and *j'* are corresponding current densities. These parameters are related by: $jA = j'A'$. The parameter, *j'*, not *j*, is the effect of the applied overpotential, and the dependency can be presented in form of Butler-Volmer equation [66]. From **Figure 6.5**, at *j* = 150 mA cm^{-2}, the values of potential of the battery employed with SWS channels are 1.07, 1.10, 1.12, and 1.15 V at 30, 50, 80, and 120 mL min^{-1}, respectively. Thus corresponding overpotentials (OCP – cell potential) are 0.46, 0.43, 0.41, and 0.38 V. The Butler-Volmer equation states that higher overpotential will result in higher current density, hence order of actual current density should be: $j'_{30} > j'_{50} > j'_{80} > j'_{120}$, which translates to $A'_{30} < A'_{50} < A'_{80} < A'_{120}$. This proves that the increasing flow rates result in higher area utilization of the electrode. As $j'_{30} > j'_{50} > j'_{80} > j'_{120}$, the relatively slower mass transfer will limit the performance of the battery at lower flow rates. In the similar way, the above explanations can be further extended to justify the superiority of SWS channels to CS channels in terms of electrode area utilization. Since, the battery with SWS channels experiences lower overpotential, leading to: $j'_{SWS} < j'_{CS}$, thus the effective area utilization of the porous graphite electrode will be higher.

There is a well-established theory that higher hydrostatic pressure in the channel allows higher penetration of electrolyte in the felt, which in result will provide higher wetted area, overcoming hydrophobic repulsion of graphite felt, and thus in higher area utilization of the electrode. Higher pressure drop required for increased electrolyte flow will reduce overall energy efficiency, and thus will adversely impact the dissemination of the VRFB technology. To qualitatively examine the effect on required pumping energy using these channels, pressure drop in the half-cell of the battery, with and without graphite felt, was measured by varying water flow rates: 10 to 120 mL min^{-1}. The flow rate was converted to Reynold's number (*Re*) by: $Re = \frac{\pi \rho V}{4 \mu d}$, where ρ, μ, and *V* are density, viscosity, and volumetric flow rate of water, respectively, and *d* is the hydraulic diameter of the channel and is equal to its one side, i.e. 0.001 m. The variation of pressure drop with varying flow rates and with *Re* are presented in **Figure 6.6**. Results show that pressure drop in the half-cell with felt is higher than that without felt, demonstrating effect of hydrophobic nature of the felt. The cell, employed with SWS channel, causes only half of pressure drop of that with a CS channel at same flow rate, indicating lower energy penalty. Although, the experiment was performed using water as a medium, not the actual vanadium electrolyte solutions, and untreated carbon felt, results provide adequate insight of required pumping energy, underpinning the superiority SWS channels to CS channels.

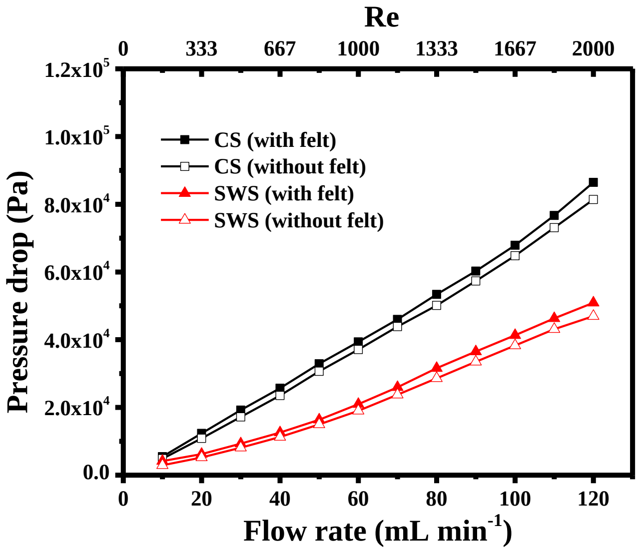

Figure 6.6. Effect of varying water flow rate on pressure drop across the half-cell employing SWS and CS channels with, and without, graphite felt electrode.

6.3.4 Discharge-charge cycles of VRFB employed with SWS channels

The performance of an energy storage device is analyzed by charge-discharge cycles, which further help in the estimation of its coulombic, voltage and energy efficiencies. For this, the electrolyte solutions were first discharged, after preparing the charged solutions employing 2-step charging method, and subsequently charged at constant current density, up to two cycles. **Figure 6.7** shows discharge-charge cycles of the VRFB performed at 20 and 40 mA cm^{-2} with two flow rates: 50 and 100 mL min^{-1}. Steps – I and III represent discharging of battery, and Steps – II and IV represent charging. Time elapsed in respective steps is mentioned in the figure. Values indicated in red and black correspond to 50 and 100 mL min^{-1}. Initial potential values of the battery in Step-I are also mentioned in the figures. Results in Figure 6.7 show that, while discharging, the potential value is higher at 100 mL min^{-1} at a fixed current density, indicating better distribution of electrolyte and higher mass-transfer at increased flow rate. A comparison of initial potential values presented in Figure 6.7(a) and (b) illustrates that, at fixed flow rate, potential decreases with increasing current, stemming from increased kinetic and ohmic loss at higher current. Discharge time in Step-I, as mentioned in the figure, follows the similar trend as the initial potential, i.e. higher flow rates allow operation of the battery for longer duration. Doubling the current density reduces the operation time approximately by half.

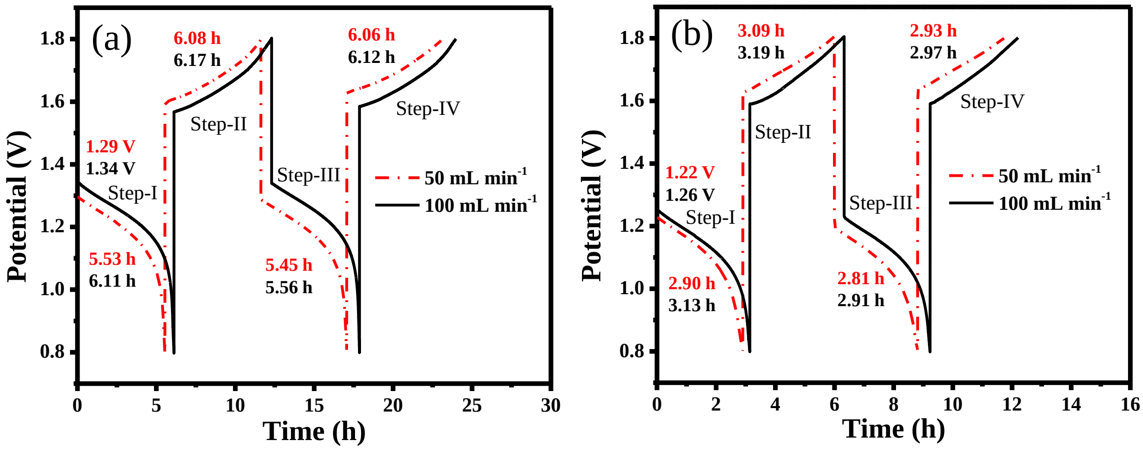

Figure 6.7. Discharge-charge curves of VRFB, coupled with SWS channels, obtained at 50 (red) and 100 mL min^{-1} (black), and at current density (a) 20 mA cm^{-2} and (b) 40 mA cm^{-2}. Steps – I and III represent discharging, and Steps – II and IV represent charging. Time elapsed (in hour) in each step, and initial potentials (in volt) at Step – I are also provided, illustrating the effect of flow rate and current.

Initial potentials in Steps – II to IV (including in Step – I) extracted from Figure 6.7 are provided in the Table 6.3. The results show that the potential slightly differs in Steps I and III (discharging), and in Steps II and IV (charging). The gradual change in the initial potential of discharging and charging steps can be explained by the time elapsed, presented in the figure. There is slight decrease in discharge and charge time from first cycle to second, indicating that the extent of discharge and charge decreases over repeated operations. This results due to the formation of mixture of vanadium ions at the end of Step – I, after reaching cutoff potential of 0.8 V. Charging in Step – II starts with this mixture, leading to higher mass-transfer resistance due to lower concentration of reacting species in the electrolyte. Hence gradual decrease in initial potential occurs while discharging, and increase in potential while charging occurs, as illustrated in Table 6.3.

Table 6.3. Initial potentials of discharging steps (Steps – I and III) and charging steps (Steps – II and IV), as shown in Figure 6.7, obtained at 20 and 40 mA cm^{-2}, and at 50 and 100 mL min^{-1}.

Discharge – charge step/ Flow rate	Initial potential (V) @ 20 mA cm^{-2}				Initial potential (V) @ 40 mA cm^{-2}			
	I	II	III	IV	I	II	III	IV
50 mL min^{-1}	1.29	1.60	1.28	1.63	1.22	1.62	1.19	1.63
100 mL min^{-1}	1.34	1.56	1.33	1.58	1.26	1.58	1.23	1.59

6.3.5 Estimation of efficiency of VRFB employed with SWS channels

The estimation of coulombic, voltage and energy efficiencies of a battery is essential for its use for an application. The coulombic efficiency (*CE*) measures the ratio of charge utilized from the device by an application to the charge stored in the battery. The voltage efficiency (*VE*) provides knowledge of ratio of average potentials during discharge and charge, and the energy efficiency (*EE*) measures the ratio of energy harvested from the battery to the stored energy. The values of these efficiencies are calculated from Steps – II and III in Figure 6.7, corresponding to charging and discharging of the battery. As the discharge-charge cycles of the battery were performed at constant current density. This indicates that *CE* depends on the ratio of discharge-charge time. For an ideal system, the ratio should be unity, and deviation from idealities arises from various losses occurring during operation [3,107,131]. The final expression of *EE* and *VE* is same, and depends on ratio of discharge-charge potential, averaged over respective time. For an energy storage device, charging potential is always higher than discharging potential at fixed current, due to internal resistances of the battery, hence the ratio will be below 1. The calculated efficiencies are presented in Table 6.4. Results illustrate that *CE* at 20 mA cm^{-2} and 50 mL min^{-1} is 89.6%, which slightly increases to 90.1% at 100 mL min^{-1}. Increasing current density betters the *CE* of the battery, but very marginally. These findings further strengthen the fact that the SWS channels uniformly distribute the electrolyte even at lower flow rates, and thus have negligible effect of flow rate and current density on coulombic efficiency. Table 6.4 also shows that the *EE* values at 50 and 100 mL min^{-1} are 70.1% and 72.9%, respectively. The efficiency values decrease with increasing current density, and are 64.4% and 67.4%, respectively, at 40 mA cm^{-2} – a loss of *EE* by ~8% by doubling the current. The higher current contributes more to the ohmic loss, hence significantly increases the charging potential and decreases the discharging potential. This reflects in loss in energy efficiency. The *CE* and *EE* of VRFB using SWS channels are higher than using CS channels, and are in similar range of SS and SMS channels, as reported in our previous work [137].

Table 6.4. Coulombic efficiency (*CE*) and energy efficiency (*EE*) of VRFB, coupled with SWS channels, at 20 and 40 mA cm^{-2}, and at 50 and 100 mL min^{-1}. Efficiencies were estimated using discharge-charge cycles, presented in Figure 6.7.

Current density /Flow rate	*CE* (%)		*VE* (%)	
	20 mA cm^{-2}	40 mA cm^{-2}	20 mA cm^{-2}	40 mA cm^{-2}
50 mL min^{-1}	89.6	90.9	70.1	64.4
100 mL min^{-1}	90.1	91.5	72.9	67.4

The findings presented above clearly indicate that due to curvy nature of SWS channels, electrolyte distributes uniformly in the electrode pores, resulting in higher conversion and utilization of higher pore surface area. Use of higher area leads to significantly lower intrinsic current density than the apparent current density, estimated based on the engraved area [127]. This is why, the concentration polarization occurs at very high current density, as evident from *iR*-free polarization curves. However, the ohmic resistance in the battery employed with SWS channels slightly increases in comparison to that with other channels (CS, SS and SMS), owing to higher conversion of vanadium ions. The SWS channels also help in achieving higher *CE* and *EE* of the battery.

6.4 Conclusions

Electrolyte distribution using flow channel plays an important role in the performance of a flow battery, where liquid electrolyte is used, and helps electroactive species transfer from bulk solution to porous spaces of electrode, leading to surface reactions. A sinusoidal wave-type serpentine (SWS) flow pattern was designed using AUTOCAD, aiming to achieve better performance of the vanadium redox flow battery at lower pumping cost than using a conventional serpentine channel, and was engraved on graphite plates. Graphite felt electrode, which is porous and suitable for electrochemical conversion of vanadium ions, was employed. Positive and negative electrolyte solutions were prepared from V(IV) salt by 2-step changing method. The polarization curves of the battery were obtained by varying flow rates: 30, 50, 80, and 120 mL min^{-1}; the deviation from OCP (~1.53 V) arises from kinetic, ohmic and mass transfer overpotentials. Electrochemical impedance spectroscopy (EIS) measurements were performed to evaluate ohmic and kinetic resistances. The high frequency response (HFR) of the battery was used to obtain *iR*-free polarization curves. The pressure drop of the half-cell employing a channel with, and without, graphite felt was measured using a pressure transducer.

Results show that increasing flow rates allows withdrawing higher current from the battery at a fixed potential, and the calculated peak power density shifts towards higher current density. The ohmic resistance, determined from HFR, using SWS channels is ~0.18 Ω, invariant with increasing flow rates. The value is slightly higher than using conventional serpentine (CS) channels (0.12 – 0.14 Ω) [127]. The charge transfer resistance estimated from EIS measurements through curve fitting of obtained Nyquist plots decreases with increasing flow rates of electrolyte. This stems from better distribution of electrolyte in the porous electrode. The *iR*-free polarization curves of the battery using SWS channels show that the mass transfer overpotential is smaller even at lower flow rates, and at 120 mL min^{-1}, the overpotential is negligible at current density as high as 500 mA cm^{-2}, whereas, for CS channels, the overpotential is higher even at low current density. These results conclusively demonstrate that SWS channels allow higher area utilization of the electrode. The *iR*-free power density monotonically increases with current density of experimental range, and is higher than using CS channels, indicating higher power can be withdrawn from the battery employing SWS channels, if ohmic resistance can be minimized. Additionally, the measured pressure drop across the cell, required for electrolyte flow, is lower by half, illustrating lesser energy penalty. The discharge-charge curves show that time of discharge and charge does not get affected significantly with increasing of flow rate, and thus has a little effect on coulombic efficiency (*CE*). The energy efficiency (*EE*) increases with flow rate and decreases with current density. The *CE* >90% is attained, and the *EE* of ~73% was achieved at 20 mA cm^{-2} and 100 mL min^{-1}. Findings in this work will help in developing flow batteries of higher efficiency by employing SWS channel. Better distribution of electrolyte in porous spaces will also improve area utilization of electrodes. Findings in this work will help in developing flow batteries of higher energy efficiency by employing SWS channel. Better distribution of electrolyte in porous spaces will also improve area utilization of electrodes. The future work will be focused on numerical study of flow pattern in channel and graphite felt, corroborating findings of the current study. Future work will focus on performance evaluation of these channels using thinner graphite felt and carbon cloth electrodes, and on the requirement of pumping power for electrolyte, as the wavy nature of channel is expected to lead to higher pressure drop across the battery.

Overall conclusions

- Performance of VRFB using CS, SS, SMS, and SWS channels are measured through polarization curves which give the information of cumulative potential loss due to kinetic, ohmic or *iR*, and mass-transfer overpotentials, at varying current.
- The potential losses are also determined at varying flow rates of electrolytes: 30, 50, 80, and 120 mL min^{-1}.
- Kinetic and ohmic resistances of VRFB are determined with each channel at above flow rates through EIS measurements.
- The Nyquist plots obtained through EIS measurements with CS, SS, SMS, and SWS channels show depressed semicircles. The experimental data are fitted using an equivalent circuit.
- Intercept of Z'-axis on Nyquist plots at higher frequency region gives the values of ohmic resistance, whereas the diameter of the semicircle gives the value of cumulative charge-transfer resistance of positive and negative sides.
- The high frequency response was used to get *iR*-free polarization curves.
- The performance of VRFB is further validated by its discharge-charge cycles performed at two current densities: 20 and 40 mA cm^{-2} and flow rates: 50 and 100 mL min^{-1}.
- Efficiencies of the battery were determined in terms of coulombic and energy efficiencies (EE).
- The results illustrate that peak power density, P_{peak}, increases with increasing flow rate of electrolyte.
- The highest P_{peak} values is achieved with SWS (585 mW cm^{-2}), followed by SS (552 mW cm^{-2}), SMS (363 mW cm^{-2}), and CS (154 mW cm^{-2}) channels.

- The effect of increasing flow rates on power densities is insignificant in case of SS channel; higher power density can be achieved even at low flow rate.
- The SS channel has a higher distribution ability of electrolyte over the electrode surface followed by SWS, SMS and CS channels.
- 2 to 5 times higher current density can be withdrawn using SMS, SS, and SWS channels compared to CS channel at the same cell potential.
- With increasing flow rates, the diameter of semicircles decreases which indicates charge-transfer kinetics increases.
- The charge-transfer resistance value is highest with CS and lowest with SMS channel, whereas with SS and SWS channels, values are almost same.
- The discharge-charge time obtained in CS, SS, SMS, and SWS channels increases with increasing flow rates of electrolyte owing to convective mass-transfer effect.
- With 20 mA cm^{-2} and 100 mL min^{-1}, overall discharge-charge time is highest using SS channels, followed by SMS, SWS, and CS channels.
- The EE decreases with increasing current density but there is no significant changes in CE values with increasing current density.
- The CE and EE values increase with increasing flow rates; the highest CE is achieved at 40 mA cm^{-2} and with 100 mL min^{-1} in SMS channel (95.2%) followed by SWS (91.5%), SS (91.4%), and CS (82.2%) channels.
- The highest EE is achieved with 20 mA cm^{-2} and with 100 mL min^{-1} in the SMS channel (77.4%), followed by SS (73.6%), SWS (72.9%) and CS channels (60.1%).

Future scope of work

- **Pressure drop measurement:** Estimation of pressure loss in a redox flow battery is one of the important aspects in determining its overall efficiency. The pressure drop across the battery helps in electrolyte flow through the channels, and in penetrating it in the porous electrode and spread over it for electrochemical reactions. If pressure loss increases, pumping cost increases – resulting in decrease in overall system efficiency. The future research work can be performed in estimating the pressure drop across the battery to facilitate electrolyte flow. It can be determined using manometers, but more preciously using differential pressure transducer.

- **Numerical investigation using computational fluid dynamics:** Numerical simulations or computational fluid dynamics are one of important tools to examine the role of flow channels in a VRFB. As the fabricated serpentine channels help in enhancing the performance of the battery by even distribution of electrolytes, numerical studies will further strengthen the statement, and will also provide future direction of work. The loopholes in the flow design can be investigated, and the path can be modified for further performance enhancement.
- **Scaling up of battery:** In the present work, area of a single cell is 10 cm^2, and the achieved power of the battery is below 1 W, which is too low to be used for any application. Scaling up of the single cell of area above 100 cm^2 is required even for a few kW power requirement. Future work can be directed for the use of these channels, designed on larger area, to fulfill the requirement. The performance of the channel might change on scaling up, but can be modified. These channels can be implemented in cell stacks by properly aligning the inlet and outlet ports.
- **Optimization of performance by using hybrid arrangement of channels:** The hybrid arrangements of flow channels in the VRFB can be used in future. The reported kinetics of the negative electrolyte is faster than that of positive electrolyte, thus thinner electrode can be used on the negative side. Accordingly, the channels, resulting in lower pressure drop, can be used. The flow directions can also be altered

from co- to counter-flow. These will help in optimizing the performance of the battery and in reducing its volumetric density.

References

[1] I. Aramendia, U. Fernandez-Gamiz, A. Martinez-San-Vicente, E. Zulueta, J.M. Lopez-Guede, Vanadium Redox Flow Batteries: A Review Oriented to Fluid-Dynamic Optimization, *Energies*. 14 (2020) 176.

[2] Á. Cunha, J. Martins, N. Rodrigues, F.P. Brito, Vanadium redox fl ow batteries : a technology review, (2014).

[3] S.K. Park, J. Shim, J.H. Yang, C.S. Jin, B.S. Lee, Y.S. Lee, K.H. Shin, J.D. Jeon, The influence of compressed carbon felt electrodes on the performance of a vanadium redox flow battery, *Electrochimica Acta*. 116 (2014) 447–452.

[4] B. Dunn, H. Kamath, J.M. Tarascon, Electrical energy storage for the grid: A battery of choices, *Science*. 334 (2011) 928–935.

[5] D. Reynard, C.R. Dennison, A. Battistel, H.H. Girault, Efficiency improvement of an all-vanadium redox flow battery by harvesting low-grade heat, *Journal of Power Sources*. 390 (2018) 30–37.

[6] H. Branco, R. Castro, A. Setas Lopes, Battery energy storage systems as a way to integrate renewable energy in small isolated power systems, *Energy for Sustainable Development*. 43 (2018) 90–99.

[7] P. Vanýsek, V. Novák, Redox flow batteries as the means for energy storage, *Journal of Energy Storage*. 13 (2017) 435–441.

[8] A. Clemente, R. Costa-castelló, Redox Flow Batteries : A Literature Review Oriented to Automatic Control, (2020) 1–31.

[9] B.K.C. N P Brandon, J S Edge, M Aunedi, E R Barbour, P G Bruce, G.H.L. T Esterle, J W Somerville, Y L Ding, C Fu, P S Grant, P J Hall, C Huang, D.J.R. Y L Li, V L Martins, M E Navarro, J O Gil Posada4, A J R Rennie, D.A.W. G Strbac, S Pérez Villar, V Yufit, J Wang, UK Researc Needs in Grid Scale Energy Storage

Technologies, 2015.

[10] B. Pinnangudi, M. Kuykendal, S. Bhadra, Smart Grid Energy Storage, Elsevier Ltd, 2017.

[11] S.S. Williamson, P.A. Cassani, S. Lukic, B. Blunier, Energy Storage, in: Alternative Energy in Power Electronics, Elsevier Inc., 2011: pp. 267–315.

[12] F. Díaz-González, A. Sumper, O. Gomis-Bellmunt, R. Villafáfila-Robles, A review of energy storage technologies for wind power applications, *Renewable and Sustainable Energy Reviews*. 16 (2012) 2154–2171.

[13] M. Skyllas-Kazacos, Electro-chemical energy storage technologies for wind energy systems, in: Stand-Alone and Hybrid Wind Energy Systems, Woodhead Publishing Limited, 2010: pp. 323–365.

[14] P. Krivik, P. Baca, InTech-Electrochemical_energy_storage.pdf, in: n.d.

[15] D. Greenwood, S. Walker, N. Wade, S. Munoz-Vaca, A. Crossland, C. Patsios, Integration of high penetrations of intermittent renewable generation in future electricity networks using storage, in: Future Energy: Improved, Sustainable and Clean Options for Our Planet, Elsevier Ltd, 2020: pp. 649–668.

[16] N. Omar, Y. Firouz, M.A. Monem, A. Samba, H. Gualous, T. Coosemans, P. Van den Bossche, J. Van Mierlo, Analysis of Nickel-Based Battery Technologies for Hybrid and Electric Vehicles, *Reference Module in Chemistry, Molecular Sciences and Chemical Engineering*. (2014) 1–13.

[17] H. Chen, T.N. Cong, W. Yang, C. Tan, Y. Li, Y. Ding, Progress in electrical energy storage system: A critical review, *Progress in Natural Science*. 19 (2009) 291–312.

[18] I. Hadjipaschalis, A. Poullikkas, V. Efthimiou, Overview of current and future energy storage technologies for electric power applications, *Renewable and*

Sustainable Energy Reviews. 13 (2009) 1513–1522.

[19] P. V. Shinde, M.K. Singh, Synthesis, characterization, and properties of graphene analogs of 2D material, in: Fundamentals and Sensing Applications of 2D Materials, Elsevier Ltd, 2019: pp. 91–143.

[20] K.K. Kar, Springer series in materials science 300 handbook of nanocomposite supercapacitor materials I, 2020.

[21] T. Wilberforce, J. Thompson, A.G. Olabi, Classification of Energy Storage Materials, in: Reference Module in Materials Science and Materials Engineering, 2020: pp. 1–7.

[22] P. Hayes, J. Arevalo, Energy storage, in: ABB Review, 2015: pp. 43–49.

[23] K.T. Chau, Pure electric vehicles, in: Alternative Fuels and Advanced Vehicle Technologies for Improved Environmental Performance: Towards Zero Carbon Transportation, 2014: pp. 655–684.

[24] N. Radacsi, W. Nuansing, Fabrication of 3D and 4D polymer micro- and nanostructures based on electrospinning, in: 3D and 4D Printing of Polymer Nanocomposite Materials: Processes, Applications, and Challenges, Elsevier Inc., 2019: pp. 191–229.

[25] J. Kim, Y. Suharto, T.U. Daim, Evaluation of Electrical Energy Storage (EES) technologies for renewable energy: A case from the US Pacific Northwest, *Journal of Energy Storage*. 11 (2017) 25–54.

[26] U. States, S.C. Johnson, F.T. Davidson, J.D. Rhodes, J.L. Coleman, S.M. Bragg-sitton, E.J. Dufek, M.E. Webber, Selecting Favorable Energy Storage Technologies for Nuclear Power, in: Storage and Hybridization of Nuclear Energy, Elsevier Inc., 2019: pp. 119–175.

[27] M. Kim, D. Yun, J. Jeon, Effect of a bromine complex agent on electrochemical

performances of zinc electrodeposition and electrodissolution in Zinc–Bromide flow battery, *Journal of Power Sources*. 438 (2019).

[28] S.T. Revankar, Chapter Six - Chemical Energy Storage, in: Storage and Hybridization of Nuclear Energy: Techno-Economic Integration of Renewable and Nuclear Energy, Elsevier Inc., 2018: pp. 177–227.

[29] Z. Abdin, K.R. Khalilpour, Single and Polystorage Technologies for Renewable-Based Hybrid Energy Systems, in: Polygeneration with Polystorage, Elsevier Inc., n.d.: pp. 77–131.

[30] Vanadium Redox Flow Batteries: An In-Depth Analysis. EPRI; Palo Alto; CA:, 2007.

[31] P. Ang, R. Remick, US Patent 4485154, 1984.

[32] A.Z. Weber, M.M. Mench, J.P. Meyers, P.N. Ross, J.T. Gostick, Q. Liu, Redox flow batteries: A review, *Journal of Applied Electrochemistry*. 41 (2011) 1137–1164.

[33] L. Ouyang, J. Huang, H. Wang, J. Liu, M. Zhu, Progress of hydrogen storage alloys for Ni-MH rechargeable power batteries in electric vehicles: A review, *Materials Chemistry and Physics*. 200 (2017) 164–178.

[34] X. Luo, J. Wang, M. Dooner, J. Clarke, Overview of current development in electrical energy storage technologies and the application potential in power system operation, *Applied Energy*. 137 (2015) 511–536.

[35] B. Garg, Introduction to Flow Batteries : Theory and Applications Charge / Discharge Behavior, (2016) 31–34.

[36] M. Skyllas-Kazacos, L. Cao, M. Kazacos, N. Kausar, A. Mousa, Vanadium electrolyte studies for the vanadium redox battery—A Review, *ChemSusChem*. 9 (2016) 1521–1543.

[37] W. Wang, X. Wei, D. Choi, X. Lu, G. Yang, C. Sun, Electrochemical cells for medium-and large-scale energy storage: Fundamentals, in: Advances in Batteries for Medium and Large-Scale Energy Storage: Types and Applications, 2015: pp. 3–28.

[38] B. Khaki, P. Das, Voltage loss and capacity fade reduction in vanadium redox battery by electrolyte flow control, *Electrochimica Acta*. 405 (2022).

[39] E. Agar, A. Benjamin, C.R. Dennison, D. Chen, M.A. Hickner, E.C. Kumbur, Reducing capacity fade in vanadium redox flow batteries by altering charging and discharging currents, *Journal of Power Sources*. 246 (2014) 767–774.

[40] R. Monteiro, J. Leirós, M. Boaventura, A. Mendes, Insights into all-vanadium redox flow battery: A case study on components and operational conditions, *Electrochimica Acta*. 267 (2018) 80–93.

[41] T. Bocklisch, Hybrid energy storage approach for renewable energy applications, *Journal of Energy Storage*. 8 (2016) 311–319.

[42] T. Haisch, H. Ji, L. Holtz, T. Struckmann, C. Weidlich, Half-cell state of charge monitoring for determination of crossover in vrfb—considerations and results concerning crossover direction and amount, *Membranes*. 11 (2021).

[43] M. Schreiber, M. Harrer, A. Whitehead, H. Bucsich, M. Dragschitz, E. Seifert, P. Tymciw, Practical and commercial issues in the design and manufacture of vanadium flow batteries, *Journal of Power Sources*. 206 (2012) 483–489.

[44] C. Doetsch, A. Pohlig, The use of flow batteries in storing electricity for national grids, in: Future Energy: Improved, Sustainable and Clean Options for Our Planet, Elsevier Ltd, 2020: pp. 263–277.

[45] K.W. Knehr, E.C. Kumbur, Open circuit voltage of vanadium redox flow batteries: Discrepancy between models and experiments, *Electrochemistry*

Communications. 13 (2011) 342–345.

[46] C. Choi, S. Kim, R. Kim, Y. Choi, S. Kim, H. young Jung, J.H. Yang, H.T. Kim, A review of vanadium electrolytes for vanadium redox flow batteries, *Renewable and Sustainable Energy Reviews*. 69 (2017) 263–274.

[47] L.F. Castañeda, F.C. Walsh, J.L. Nava, C. Ponce de León, Graphite felt as a versatile electrode material: Properties, reaction environment, performance and applications, *Electrochimica Acta*. 258 (2017) 1115–1139.

[48] K.J. Kim, M.S. Park, Y.J. Kim, J.H. Kim, S.X. Dou, M. Skyllas-Kazacos, A technology review of electrodes and reaction mechanisms in vanadium redox flow batteries, *Journal of Materials Chemistry A*. 3 (2015) 16913–16933.

[49] L. Gubler, Membranes and separators for redox flow batteries, *Current Opinion in Electrochemistry*. 18 (2019) 31–36.

[50] D.G. Oei, Permeation of vanadium cations through anionic and cationic membranes, *Journal of Applied Electrochemistry*. 15 (1985) 231–235.

[51] M. Skyllas-Kazacos, F. Grossmith, Efficient Vanadium Redox Flow Cell, *Journal of The Electrochemical Society*. 134 (1987) 2950–2953.

[52] H. Zhang, X. Li, J. Zhang, Redox flow batteries: Fundamentals and applications, *Redox Flow Batteries: Fundamentals and Applications*. (2017) 1–432.

[53] X.Z. Yuan, C. Song, A. Platt, N. Zhao, H. Wang, H. Li, K. Fatih, D. Jang, A review of all-vanadium redox flow battery durability: Degradation mechanisms and mitigation strategies, *International Journal of Energy Research*. 43 (2019) 6599–6638.

[54] E. Kjeang, B.T. Proctor, A.G. Brolo, D.A. Harrington, N. Djilali, D. Sinton, High-performance microfluidic vanadium redox fuel cell, *Electrochimica Acta*. 52 (2007) 4942–4946.

[55] M. Benmelouka, S. Messaoudi, E. Furet, R. Gautier, E. Le Fur, J.Y. Pivan, Density functional investigation of hydrated V(II) and V(III) ions: Influence of the second coordination sphere; water exchange mechanism, *Journal of Physical Chemistry A*. 107 (2003) 4122–4129.

[56] F. Sepehr, S.J. Paddison, The solvation structure and thermodynamics of aqueous vanadium cations, *Chemical Physics Letters*. 585 (2013) 53–58.

[57] M. Skyllas-Kazacos, C. Menictas, M. Kazacos, Thermal Stability of Concentrated V(V) Electrolytes in the Vanadium Redox Cell, *Journal of The Electrochemical Society*. 143 (1996) L86–L88.

[58] N. Elgrishi, K.J. Rountree, B.D. McCarthy, E.S. Rountree, T.T. Eisenhart, J.L. Dempsey, A Practical Beginner’s Guide to Cyclic Voltammetry, *Journal of Chemical Education*. 95 (2018) 197–206.

[59] T. Davies, J. Tummino, High-Performance Vanadium Redox Flow Batteries with Graphite Felt Electrodes, *C*. 4 (2018) 8.

[60] D.S. Aaron, Q. Liu, Z. Tang, G.M. Grim, A.B. Papandrew, A. Turhan, T.A. Zawodzinski, M.M. Mench, Dramatic performance gains in vanadium redox flow batteries through modified cell architecture, *Journal of Power Sources*. 206 (2012) 450–453.

[61] D. Aaron, Z. Tang, A.B. Papandrew, T.A. Zawodzinski, Polarization curve analysis of all-vanadium redox flow batteries, *Journal of Applied Electrochemistry*. 41 (2011) 1175–1182.

[62] A. Di Blasi, N. Briguglio, O. Di Blasi, V. Antonucci, Charge-discharge performance of carbon fiber-based electrodes in single cell and short stack for vanadium redox flow battery, *Applied Energy*. 125 (2014) 114–122.

[63] Q. Xu, T.S. Zhao, P.K. Leung, Numerical investigations of flow field designs for

vanadium redox flow batteries, *Applied Energy*. 105 (2013) 47–56.

[64] C. Yin, Y. Gao, S. Guo, H. Tang, A coupled three dimensional model of vanadium redox flow battery for flow field designs, *Energy*. 74 (2014) 886–895.

[65] T. Jyothi Latha, S. Jayanti, Hydrodynamic analysis of flow fields for redox flow battery applications batteries, *Journal of Applied Electrochemistry*. 44 (2014) 995–1006.

[66] A.J. Bard and L.R. Faulkner, Electrochemical methods: Fundamentals and applications, 2nd ed., John Wiley & Sons, Inc., New York, 2001.

[67] D. Sun, Y. Chen, Electrode Kinetics of CO2 Electroreduction, in: 2016: pp. 103–154.

[68] S. Kim, Vanadium redox flow batteries: Electrochemical engineering, *Energy Storage Devices*. (2019) 1–19.

[69] A. Tang, J. Bao, M. Skyllas-Kazacos, Studies on pressure losses and flow rate optimization in vanadium redox flow battery, *Journal of Power Sources*. 248 (2014) 154–162.

[70] W.Y. Hsieh, C.H. Leu, C.H. Wu, Y.S. Chen, Measurement of local current density of all-vanadium redox flow batteries, *Journal of Power Sources*. 271 (2014) 245–251.

[71] J. Houser, J. Clement, A. Pezeshki, M.M. Mench, Influence of architecture and material properties on vanadium redox flow battery performance, *Journal of Power Sources*. 302 (2016) 369–377.

[72] T. Jyothi Latha, S. Jayanti, Ex-situ experimental studies on serpentine flow field design for redox flow battery systems, *Journal of Power Sources*. 248 (2014) 140–146.

[73] Q. Xu, T.S. Zhao, C. Zhang, Performance of a vanadium redox flow battery with

and without flow fields, *Electrochimica Acta*. 142 (2014) 61–67.

[74] S. Kumar, S. Jayanti, Effect of flow field on the performance of an all-vanadium redox flow battery, *Journal of Power Sources*. 307 (2016) 782–787.

[75] T.M. Abou, A.E. Kabeel, M. Mahgoub, Corrugated plate heat exchanger review, *Renewable and Sustainable Energy Reviews*. (2016) 1–9.

[76] P. Agarwal, Adhirathsik, V. Shanthi, Application of heat exchangers in bioprocess industry: A review, *International Journal of Pharmacy and Pharmaceutical Sciences*. 6 (2014) 24–28.

[77] J. Zhang, X. Zhu, M.E. Mondejar, F. Haglind, A review of heat transfer enhancement techniques in plate heat exchangers, *Renewable and Sustainable Energy Reviews*. 101 (2019) 305–328.

[78] N.S. Pandya, H. Shah, M. Molana, A. Kumar, European Journal of Mechanics / B Fluids Heat transfer enhancement with nanofluids in plate heat exchangers : A comprehensive review, *European Journal of Mechanics / B Fluids*. 81 (2020) 173–190.

[79] H. Shokouhmand, M. Hasanpour, Case Studies in Thermal Engineering Effect of flow maldistribution on the optimal design of plate heat exchanger using constrained multi objective genetic algorithm, *Case Studies in Thermal Engineering*. 18 (2020) 100570.

[80] A.A. Bojang, H.S. Wu, Design, fundamental principles of fabrication and applications of microreactors, *Processes*. 8 (2020).

[81] X. Yao, Y. Zhang, L. Du, J. Liu, J. Yao, Review of the applications of microreactors, *Renewable and Sustainable Energy Reviews*. 47 (2015) 519–539.

[82] M. Brivio, W. Verboom, D.N. Reinhoudt, Miniaturized continuous flow reaction vessels: Influence on chemical reactions, *Lab on a Chip*. 6 (2006) 329–344.

[83] X. Li, I. Sabir, Review of bipolar plates in PEM fuel cells: Flow-field designs, *International Journal of Hydrogen Energy*. 30 (2005) 359–371.

[84] P. V. Suresh, S. Jayanti, A.P. Deshpande, P. Haridoss, An improved serpentine flow field with enhanced cross-flow for fuel cell applications, *International Journal of Hydrogen Energy*. 36 (2011) 6067–6072.

[85] C.R. Dennison, E. Agar, B. Akuzum, E.C. Kumbur, Enhancing mass transport in redox flow batteries by tailoring flow field and electrode design, *Journal of The Electrochemical Society*. 163 (2016) A5163–A5169.

[86] A. Arvay, J. French, J.C. Wang, X.H. Peng, A.M. Kannan, Nature inspired flow field designs for proton exchange membrane fuel cell, *International Journal of Hydrogen Energy*. 38 (2013) 3717–3726.

[87] P.J. Hamilton, B.G. Pollet, Polymer electrolyte membrane fuel cell (PEMFC) flow field plate: Design, materials and characterisation, *Fuel Cells*. 10 (2010) 489–509.

[88] M.M. Mench, Fuel Cell Engines, 2008.

[89] M. Al-Yasiri, J. Park, Study on channel geometry of all-vanadium redox flow batteries, *Journal of The Electrochemical Society*. 164 (2017) A1970–A1982.

[90] W.M. Yan, C.H. Yang, C.Y. Soong, F. Chen, S.C. Mei, Experimental studies on optimal operating conditions for different flow field designs of PEM fuel cells, *Journal of Power Sources*. 160 (2006) 284–292.

[91] K.B.S. Prasad, S. Jayanti, Effect of channel-to-channel cross-flow on local flooding in serpentine flow-fields, *Journal of Power Sources*. 180 (2008) 227–231.

[92] S. Maharudrayya, S. Jayanti, A.P. Deshpande, Flow distribution and pressure drop in parallel-channel configurations of planar fuel cells, *Journal of Power Sources*. 144 (2005) 94–106.

[93] C.H. Tian, R. Chein, K.L. Hsueh, C.H. Wu, F.H. Tsau, Design and modeling of

electrolyte pumping power reduction in redox flow cells, *Rare Metals*. 30 (2011) 16–21.

[94] K.B. Shyam Prasad, S. Maharudrayya, S. Jayanti, Flow maldistribution in interdigitated channels used in PEM fuel cells, *Journal of Power Sources*. 159 (2006) 595–604.

[95] Y. Wang, S. Basu, C.Y. Wang, Modeling two-phase flow in PEM fuel cell channels, *Journal of Power Sources*. 179 (2008) 603–617.

[96] R.J. Kee, H. Zhu, Distribution of incompressible flow within interdigitated channels and porous electrodes, *Journal of Power Sources*. 299 (2015) 509–518.

[97] J. Lee, J. Kim, H. Park, Numerical simulation of the power-based efficiency in vanadium redox flow battery with different serpentine channel size, *International Journal of Hydrogen Energy*. 44 (2019) 29483–29492.

[98] E. Ali, H. Kwon, J. Kim, H. Park, Numerical study on serpentine design flow channel configurations for vanadium redox flow batteries, *Journal of Energy Storage*. 32 (2020) 101802.

[99] J.Q. Chen, B.G. Wang, H.L. Lv, Numerical simulation and experiment on the electrolyte flow distribution for all vanadium redox flow battery, *Advanced Materials Research*. 236–238 (2011) 604–607.

[100] H. Yang, T.S. Zhao, Effect of anode flow field design on the performance of liquid feed direct methanol fuel cells, *Electrochimica Acta*. 50 (2005) 3243–3252.

[101] Y. Lu, R.G. Reddy, Effect of flow fields on the performance of micro-direct methanol fuel cells, *International Journal of Hydrogen Energy*. 36 (2011) 822–829.

[102] B.M. Sudaroli, A.K. Kolar, Experimental and Numerical Study of Serpentine Flow Fields for Improving Direct Methanol Fuel Cell Performance, *Fuel Cells*. 15

(2015) 826–838.

[103] W.B. Zhu SQ, Chen JQ, Wang Q, Influence of flow channel structure and electrolyte flow state on the performance of VRB, *Battery*. 38 (2008) 285–287.

[104] S.H. S. Tsushima, S. Sasaki, Influence of Cell Geometry and Operating Parameters On Performance of a Redox Flow Battery With Serpentine and Interdigitated Flow Fields, *ECS Meeting Abstracts*. (2013).

[105] R.M. Darling, M.L. Perry, The influence of electrode and channel configurations on flow battery performance, *Journal of The Electrochemical Society*. 161 (2014) A1381–A1387.

[106] J. Houser, A. Pezeshki, J.T. Clement, D. Aaron, M.M. Mench, Architecture for improved mass transport and system performance in redox flow batteries, *Journal of Power Sources*. 351 (2017) 96–105.

[107] S. Maurya, P.T. Nguyen, Y.S. Kim, Q. Kang, R. Mukundan, Effect of flow field geometry on operating current density, capacity and performance of vanadium redox flow battery, *Journal of Power Sources*. 404 (2018) 20–27.

[108] M. Al-Yasiri, J. Park, A novel cell design of vanadium redox flow batteries for enhancing energy and power performance, *Applied Energy*. 222 (2018) 530–539.

[109] B. Akuzum, Y.C. Alparslan, N.C. Robinson, E. Agar, E.C. Kumbur, Obstructed flow field designs for improved performance in vanadium redox flow batteries, *Journal of Applied Electrochemistry*. 49 (2019) 551–561.

[110] X. Ma, H. Zhang, C. Sun, Y. Zou, T. Zhang, An optimal strategy of electrolyte flow rate for vanadium redox flow battery, *Journal of Power Sources*. 203 (2012) 153–158.

[111] R. Gundlapalli, S. Jayanti, Effect of channel dimensions of serpentine flow fields on the performance of a vanadium redox flow battery, *Journal of Energy Storage*.

23 (2019) 148–158.

[112] V. Pasala, K. Ramanujam, On In–situ Redox Balancing of Vanadium Redox Flow Battery Using D-Fructose as Negative Electrolyte Additive, *ChemistrySelect*. 2 (2017) 720–727.

[113] J. Liu, S. Liu, Z. He, H. Han, Y. Chen, Effects of organic additives with oxygen- and nitrogen-containing functional groups on the negative electrolyte of vanadium redox flow battery, *Electrochimica Acta*. 130 (2014) 314–321.

[114] M. Skyllas-Kazacos, M.H. Chakrabarti, S.A. Hajimolana, F.S. Mjalli, M. Saleem, Progress in flow Battery research and development, *Journal of The Electrochemical Society*. 158 (2011) R55.

[115] W. Wang, Q. Luo, B. Li, X. Wei, L. Li, Z. Yang, Recent progress in redox flow battery research and development, *Advanced Functional Materials*. 23 (2013) 970–986.

[116] P. Leung, X. Li, C. Ponce De León, L. Berlouis, C.T.J. Low, F.C. Walsh, Progress in redox flow batteries, remaining challenges and their applications in energy storage, *RSC Advances*. 2 (2012) 10125–10156.

[117] K. Lourenssen, J. Williams, F. Ahmadpour, R. Clemmer, S. Tasnim, Vanadium redox flow batteries: A comprehensive review, *Journal of Energy Storage*. 25 (2019) 100844.

[118] L. Joerissen, J. Garche, C. Fabjan, G. Tomazic, Possible use of vanadium redox-flow batteries for energy storage in small grids and stand-alone photovoltaic systems, *Journal of Power Sources*. 127 (2004) 98–104.

[119] S. Rudolph, U. Schröder, R.I. Bayanov, K. Blenke, I.M. Bayanov, Optimal electrolyte flow distribution in hydrodynamic circuit of vanadium redox flow battery, Elsevier B.V., 2015.

[120] S. Tsushima, S. Sasaki, S. Hirai, Influence of cell geometry and operating parameters on performance of a redox flow battery with serpentine and interdigitated flow fields, *ECS Meeting Abstracts*. (2013) 2–3.

[121] S. Kim, J. Yan, B. Schwenzer, J. Zhang, L. Li, J. Liu, Z. Yang, M.A. Hickner, Cycling performance and efficiency of sulfonated poly(sulfone) membranes in vanadium redox flow batteries, *Electrochemistry Communications*. 12 (2010) 1650–1653.

[122] J.S. Lawton, A. Jones, T. Zawodzinski, Concentration dependence of VO 2+ crossover of Nafion for vanadium redox flow batteries, *Journal of The Electrochemical Society*. 160 (2013) A697–A702.

[123] Z. Yang, J. Zhang, M.C.W. Kintner-Meyer, X. Lu, D. Choi, J.P. Lemmon, J. Liu, Electrochemical energy storage for green grid, *Chemical Reviews*. 111 (2011) 3577–3613.

[124] T. Shigematsu, T. Kumamoto, H. Deguchi, T. Hara, Applications of a vanadium redox-flow battery to maintain power quality, in: IEEE/PES Transmission and Distribution Conference and Exhibition, 2002: pp. 1065–1070 vol.2.

[125] T. Shigematsu, Redox flow battery for energy storage, *SEI Technical Review*. (2011) 4–13.

[126] K. Yano, S. Hayashi, T. Kumamoto, T. Shibata, K. Yamanishi, K. Fujikawa, Development and demonstration of redox flow battery system, *SEI Technical Review*. (2017) 22–28.

[127] H. Sharma, M. Kumar, Enhancing power density of a vanadium redox flow battery using modified serpentine channels, *Journal of Power Sources*. 494 (2021) 229753.

[128] C.N. Sun, F.M. Delnick, D.S. Aaron, A.B. Papandrew, M.M. Mench, T.A.

Zawodzinski, Probing electrode losses in all-vanadium redox flow batteries with impedance spectroscopy, *ECS Electrochemistry Letters*. 2 (2013) 2013–2015.

[129] J. Xi, S. Xiao, L. Yu, L. Wu, L. Liu, X. Qiu, Broad temperature adaptability of vanadium redox flow battery - Part 2: Cell research, *Electrochimica Acta*. 191 (2016) 695–704.

[130] D. Reed, E. Thomsen, B. Li, W. Wang, Z. Nie, B. Koeppel, V. Sprenkle, Performance of a low cost interdigitated flow design on a 1 kW class all vanadium mixed acid redox flow battery, *Journal of Power Sources*. 306 (2016) 24–31.

[131] M. Skyllas-Kazacos, M. Kazacos, State of charge monitoring methods for vanadium redox flow battery control, *Journal of Power Sources*. 196 (2011) 8822–8827.

[132] J.T. Vardner, A.A. Ye, D.A. Valdes, A.C. West, Current-driven vanadium crossover as a function of SOC and SOD in the vanadium redox flow battery, *Journal of The Electrochemical Society*. 167 (2020) 080512.

[133] E. Agar, Species transport mechanisms governing crossover and capacity loss in vanadium redox flow batteries, Drexel University, 2014.

[134] M. Rychcik, M. Skyllas-Kazacos, Characteristics of a new all-vanadium redox flow battery, *Journal of Power Sources*. 22 (1988) 59–67.

[135] E. Sum, M. Rychcik, M. Skyllas-kazacos, Investigation of the V(V)/V(IV) system for use in the positive half-cell of a redox battery, *Journal of Power Sources*. 16 (1985) 85–95.

[136] P. Singh, B. Jonshagen, Zinc-bromine battery for energy storage, *Journal of Power Sources*. 35 (1991) 405–410.

[137] H. Sharma, M. Kumar, Enhancing energy efficiency of a vanadium redox flow battery using modified serpentine channels, *Submitted. Unplublished Work.* (n.d.).

[138] T. Hadush, Flow in pipes Flow in pipes, 2004.

[139] E. asadipour, Analysis of fluid flow in redox flow batteries, *Engineering and Applied Science*. (2021).

Appendix A

A.1 Calculation of pressure drop for Conventional Serpentine (CS) channel without graphite felt:

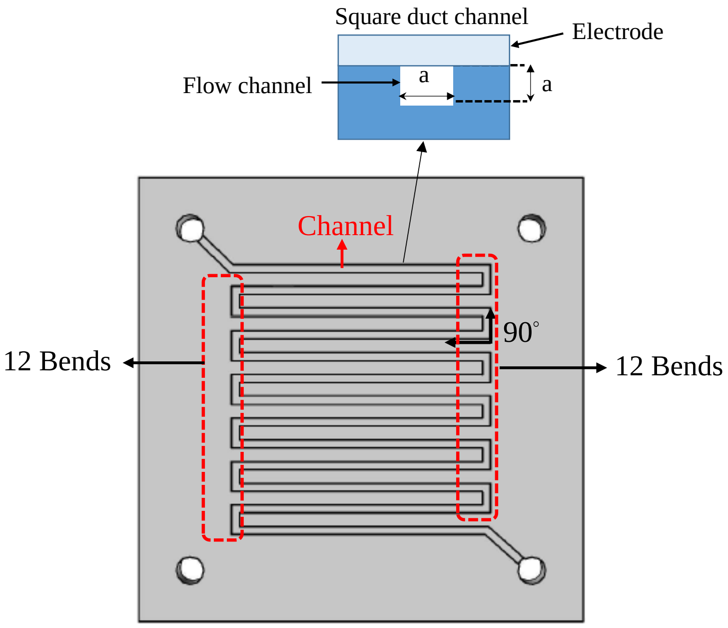

Figure A.1. Image of conventional serpentine (CS) channel.

- Cross sectional area of channel (A_c) = 1 mm × 1 mm = 1×10^{-6} m^2
- Hydraulic diameter (D)= 4 × Flow area / wetted perimeter =

$$\frac{4a^2}{4a} = \frac{4(1\times1)}{4\times1} = 0.001\text{ m}$$

- Density of water = ρ_{water} =1000 kg m^{-3}
- Viscosity of water = μ = 0.001 Pa.s

where *f* is a friction factor, K_L is a coefficient of loss due to bend, *L* is the total length of flow channels, *D* is the diameter of a channel and *v* is the velocity of water in channel.

- K_L = 1.1 for 90° bend [138],

For 24 bends, net $K_L = 24 \times 1.1 = 26.4$

- Velocity of water at 30 mL min^{-1} $= \dfrac{\text{Flow rate}}{\text{Area}} = \dfrac{Q_f}{A_c} = \dfrac{30\times10^{-6}\ \text{m}}{1\times10^{-6}\ \text{m}^2\times 60\,\text{s}} = 0.5\,\text{m}\,\text{s}^{-1}$

- Reynolds number = $N_{Re} = \dfrac{\rho v D}{\mu} = \dfrac{1000\times0.5\times0.001}{0.001} = 500$

N_{Re} is less than 2100, flow is laminar

- $f = \dfrac{16}{N_{Re}} = \dfrac{16}{500} = 0.032$

- Pressure drop $= \rho_{water}\times(4f\dfrac{L}{D}+K_L)\dfrac{v^2}{2} = 1000\times(4\times0.032\times\dfrac{0.416}{0.001}+26.4)\times\dfrac{0.5^2}{2} = 9956$ Pa

Table A.1. Calculated pressure drop in CS channel at 30, 50, 80, and 120 mL min^{-1}.

Flow rate, Q_t (mL min^{-1})	Velocity, v (m/s)	N_{Re}	f	$4f\frac{L}{D}$	Pressure drop (Pa)
30	0.5	500	0.032	53	9956
50	0.83	830	0.019	32	20142
80	1.33	1330	0.012	20	41054
120	2.0	2000	0.008	13	79424

A.2 Calculation of pressure drop for Conventional Serpentine (CS) channel with graphite felt:

Darcy’s law is applicable for flow of liquid through porous medium. In case of low Reynolds number the pressure drop across porous medium is linearly proportional to the velocity of liquid and the proportionality constant is expressed in terms of permeability, K, as:

$$\frac{dP}{dZ} = (\mu / K) v$$

where $\frac{dP}{dZ}$ a pressure gradient (N m^{-1}) is, μ is a dynamic viscosity (Ns m^{-2}), v is a superficial velocity (m s^{-1}), and K is the permeability (m^2).

Jyoti and Latha ex-situ experimental analysis shows variation of velocity with channels in serpentine flow field [72]. The velocity in second and the subsequent channels in serpentine flow field is little decreased as compared to first channel.

On the basis of Navier Strokes assumptions, Erfan Asadipour demonstrates that pressure gradient in lateral directions are negligible which shows velocity in that direction is negligible. It describes most of the part of liquid will flow in channels and less than or equal to 1% is contributed in porous medium [139]. By following these results the overall pressure drop across felt and channels can be calculated separately using Darcy's law.

Total flow rate (Q_t) = 0.99 × Flow rate in channel (Q_c) + 0.01 × flow rate in felt (Q_f)

- Uncompressed thickness of graphite felt = 6.35 mm
- Thickness of graphite felt after compression of 32 % = 4.318 mm
- Permeability of graphite felt (K) in a compressed state = 4.5×10^{-11} m^2 [72]
- Width of graphite felt = 32 mm
- Area of graphite felt = 32 mm × 4.318 mm = 138.176×10^{-6} m^2
- Distance between first and last channel = 32.2 mm
- Total flow rate = 30 mL min^{-1}
- Flow rate in channel = 0.99 × 30 mL min^{-1} = 29.7 mL min^{-1}
- Flow rate in felt = 0.01 × 30 mL min^{-1} = 0.3 mL min^{-1}
- $\text{Velocity in channel} = \frac{\text{Flow rate in channel}}{\text{Area of channel}} = \frac{29.7 \times 10^{-6}\ \text{m}^3}{60\,\text{s} \times 10^{-6}\ \text{m}^2} = 0.495\,\text{m s}^{-1}$

- $\text{Velocity in felt} = \dfrac{\text{Flow rate in felt}}{\text{Area of felt}} = \dfrac{0.3\times10^{-6}\ \text{m}^3}{60\,\text{s}\times138.176\times10^{-6}\ \text{m}^2} = 3.62\times10^{-5}\ \text{m s}^{-1}$

- Reynolds number = $N_{Re} = \dfrac{\rho v D}{\mu} = \dfrac{1000\times0.495\times0.001}{0.001} = 495$

- $f = \dfrac{16}{N_{Re}} = \dfrac{16}{495} = 0.0323$

- $\text{Pressure drop in channel} = \rho_{water}\times(4f\dfrac{L}{D}+K_L)\dfrac{v^2}{2} = 1000\times(4\times0.0323\times\dfrac{0.416}{0.001}+26.4)\times\dfrac{0.495^2}{2}$

  = 9824 Pa = $\Delta P_{channel}$

- $\text{Pressure drop in felt} = (\mu/K)v\times0.322 = \left(\dfrac{0.001}{4.5\times10^{-11}}\right)\times3.62\times10^{-5}\times0.322$

  = 259 Pa = ΔP_{felt}

- Total pressure drop = $\Delta P_{channel} + \Delta P_{felt} = 9824 + 259 = 10083$ Pa

Table A.2. Comparison of calculated pressure drop in CS channels and in graphite felt at 30, 50, 80, and 120 mL min^{-1}.

Total flow rate, Q_f (mL min^{-1})	Flow rate in channel (mL min^{-1}) = 0.99 × Q_f	Flow rate in felt (mL min^{-1}) = 0.01 × Q_f	Velocity in channel (m s^{-1})	Velocity in felt (m s^{-1})	N_{Re}	f	Pressure drop in channel, $\Delta P_{channel}$ (Pa)	Pressure drop in felt, ΔP_{felt} (Pa)	Total pressure drop = $\Delta P_{channel} + \Delta P_{felt}$ (Pa)
30	29.7	0.3	0.495	3.62×10^{-5}	495	0.0323	9824	259	10083
50	49.5	0.5	0.825	6.03×10^{-5}	825	0.0194	19967	432	20399
80	79.2	0.8	1.32	9.65×10^{-5}	1320	0.0121	40572	690	41262
120	118.8	1.2	1.98	1.44×10^{-4}	1980	0.0081	78107	1036	79143

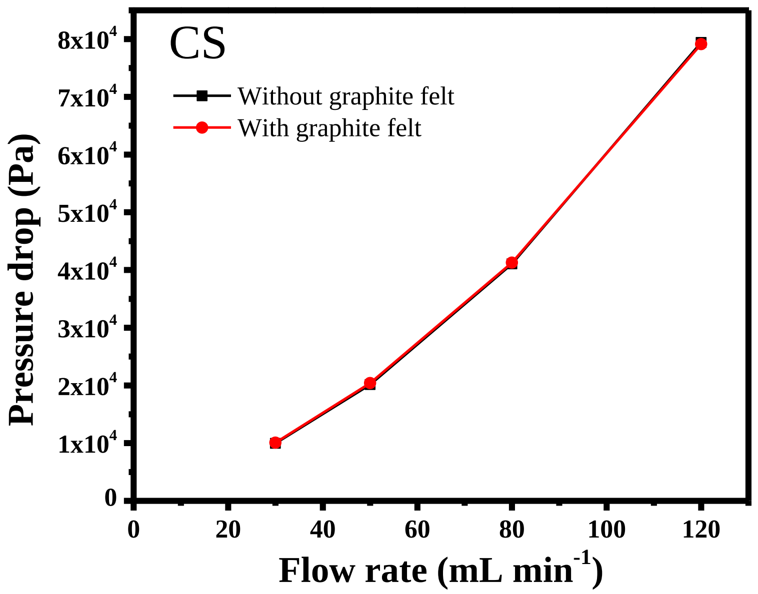

Figure A.2. Flow rate (mL min^{-1}) vs. Pressure drop (Pa) graph of CS channel.

Table. A.3. Summarized table of pressure drop calculated with and without felt.

Flow rate, Q_t (mL min^{-1})	Pressure drop without felt (Pa)	Pressure drop with felt (Pa)
30	9956	10083
50	20142	20398
80	41054	41262
90	49668	49654
100	58853	58765
110	68772	68594
120	79424	79143

Note: The comparison of pressure drop calculated at 30, 50, and 80 mL min^{-1}, between with and without felt in the summarized Table A.3, shows that the pressure drop with felt is higher than without felt. But as on increasing the flow rate above 80 mL min^{-1}, the same trend is reversed. This result is presented based on assumptions of 1 % of liquid electrolyte is passing through felt, the pressure drop in lateral direction is almost zero by the Navier Strokes equation.

A.3 Calculation of pressure drop for Split Serpentine (SS) channel without graphite felt:

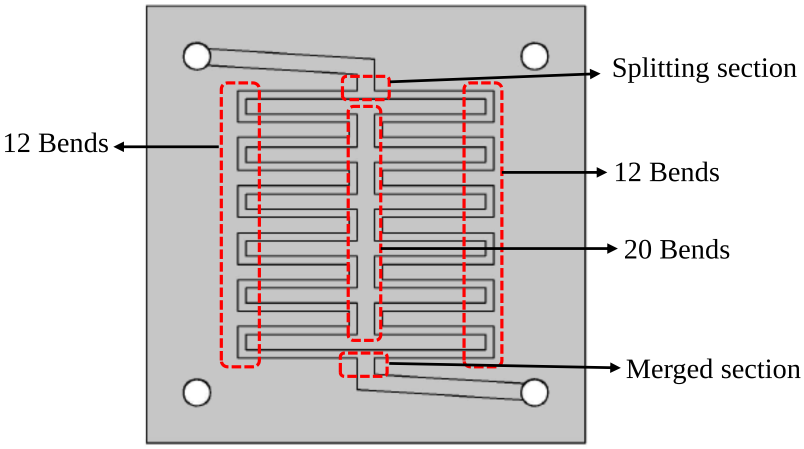

Figure A.3. Image of Split serpentine (SS) channel.

- K_L = 1.1, for 90° bend,
- Net value of K_L for bends = 1.1 × 24 bends = 26.4
- Velocity of water at 30 mL min^{-1} = 0.5 m s^{-1}
- K_s = 2 (for splitting section) [138] = K_s × number of split section = 2 × 1 = 2
- K_m = 0.5 (for merged section) [138] = K_m × number of merged section = 0.5 × 1 = 0.5
- Distance between first and last channel = 32.3 mm
- Pressure drop at 30 mL min^{-1} $= \rho_{water} \times (4f\frac{L}{D} + K_L + K_s + K_m)\frac{v^2}{2} =$

$$1000 \times (4 \times 0.032 \times \frac{0.206}{0.001} + 26.4 + 2 + 0.5) \times \frac{0.5^2}{2} = 6909 \text{ Pa}$$

Table A.4. Calculated pressure drop in SS channel at 30, 50, 80, and 120 mL min^{-1}.

Flow rate, Q_t (mL min^{-1})	Velocity, v (m s^{-1})	N_{Re}	f	$4f\frac{L}{D}$	Pressure drop (Pa)
30	0.5	500	0.032	26	6909
50	0.83	830	0.019	16	15426
80	1.33	1330	0.012	10	34328
120	2.0	2000	0.008	7	70984

A.4 Calculation of pressure drop for Split Serpentine (SS) channel with graphite felt:

Table A.5. Comparison of calculated pressure drop in SS channels and in graphite felt at 30, 50, 80, and 120 mL min^{-1}.

Total flow rate, Q_f (mL min^{-1})	Flow rate in channel (mL min^{-1}) = 0.99 × Q_f	Flow rate in felt (mL min^{-1}) = 0.01 × Q_f	Velocity in channel (m s^{-1})	Velocity in felt (m s^{-1})	N_{Re}	f	Pressure drop in channel, $\Delta P_{channel}$ (Pa)	Pressure drop in felt, ΔP_{felt} (Pa)	Total pressure drop = $\Delta P_{channel} + \Delta P_{felt}$ (Pa)
30	29.7	0.3	0.495	3.62×10^{-5}	495	0.0323	6804	260	7064
50	49.5	0.5	0.825	6.03×10^{-5}	825	0.0194	15273	433	15706
80	79.2	0.8	1.32	9.65×10^{-5}	1320	0.0121	33879	693	34572
120	118.8	1.2	1.98	1.44×10^{-4}	1980	0.0081	69702	1039	70741

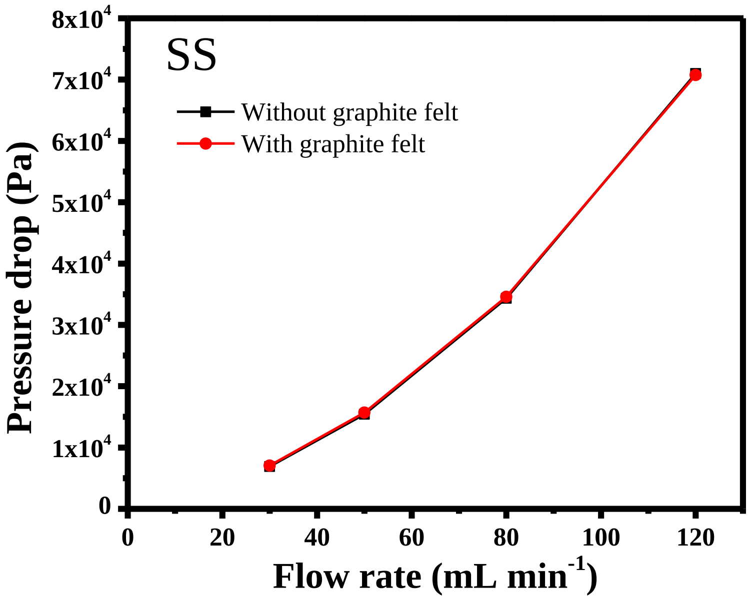

Figure A.4. Flow rate (mL min^{-1}) vs. Pressure drop (Pa) graph of SS channel.

A.5 Calculation of pressure drop for Split Merged Serpentine (SMS) channel without graphite felt:

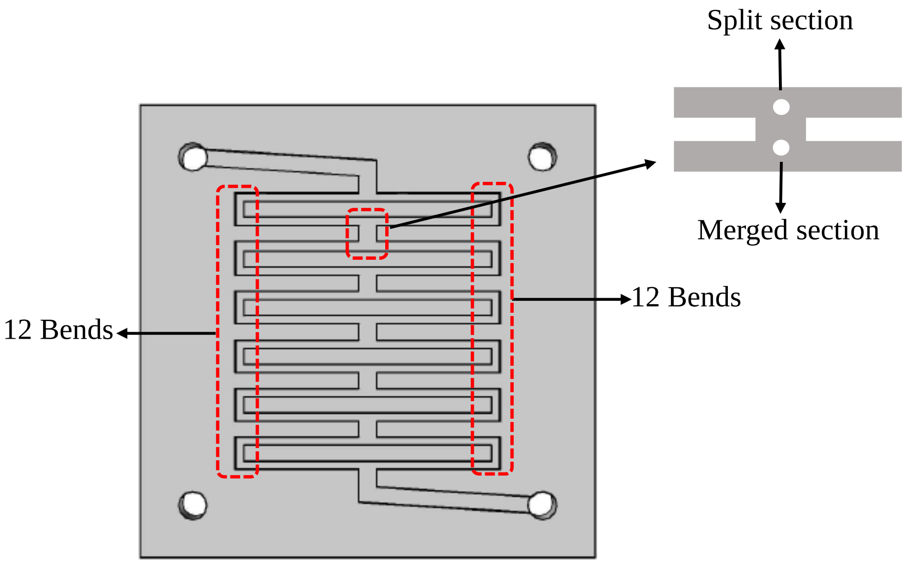

Figure A.5. Image of Split Merged Serpentine (SMS) channel

- K_L = 1.1, for 90° bend,
- Net value of K_L for bends = 1.1 × 24 bends = 26.4
- Velocity of water at 30 mL min^{-1} = 0.5 m s^{-1}
- K_s = 2 (for splitting section) = K_s × number of split section = 2 × 6 = 12
- K_m = 0.5 (for merged section) = K_m × number of merged section = 0.5 × 6 = 3
- Distance between first and last channel = 32.3 mm
- $\text{Pressure drop at 30 mL min}^{-1} = \rho_{water} \times (4f\frac{L}{D} + K_L + K_s + K_m)\frac{v^2}{2} =$

$$1000 \times (4 \times 0.032 \times \frac{0.206}{0.001} + 26.4 + 12 + 3) \times \frac{0.5^2}{2} = 8471 \text{ Pa}$$

Table A.6. Calculated pressure drop in SMS channel at 30, 50, 80, and 120 mL min^{-1}.

Flow rate, Q_t (mL min^{-1})	Velocity, v (m s^{-1})	N_{Re}	f	$4f\frac{L}{D}$	Pressure drop (Pa)
30	0.5	500	0.032	26	8471
50	0.83	830	0.019	16	19732
80	1.33	1330	0.012	10	45384
120	2.0	2000	0.008	7	95984

A.6 Calculation of pressure drop for Split Merged Serpentine (SMS) channel with graphite felt:

Table A.7. Comparison of calculated pressure drop in SMS channels and in graphite felt at 30, 50, 80, and 120 mL min^{-1}.

Total flow rate, Q_f (mL min^{-1})	Flow rate in channel (mL min^{-1}) = $0.99 \times Q_f$	Flow rate in felt (mL min^{-1}) = $0.01 \times Q_f$	Velocity in channel (m s^{-1})	Velocity in felt (m s^{-1})	N_{Re}	f	Pressure drop in channel, $\Delta P_{channel}$ (Pa)	Pressure drop in felt, ΔP_{felt} (Pa)	Total pressure drop = $\Delta P_{channel} + \Delta P_{felt}$ (Pa)
30	29.7	0.3	0.495	3.62×10^{-5}	495	0.0323	8335	260	8595
50	49.5	0.5	0.825	6.03×10^{-5}	825	0.0194	19527	433	19960
80	79.2	0.8	1.32	9.65×10^{-5}	1320	0.0121	44769	693	45462
120	118.8	1.2	1.98	1.44×10^{-4}	1980	0.0081	94204	1039	95243

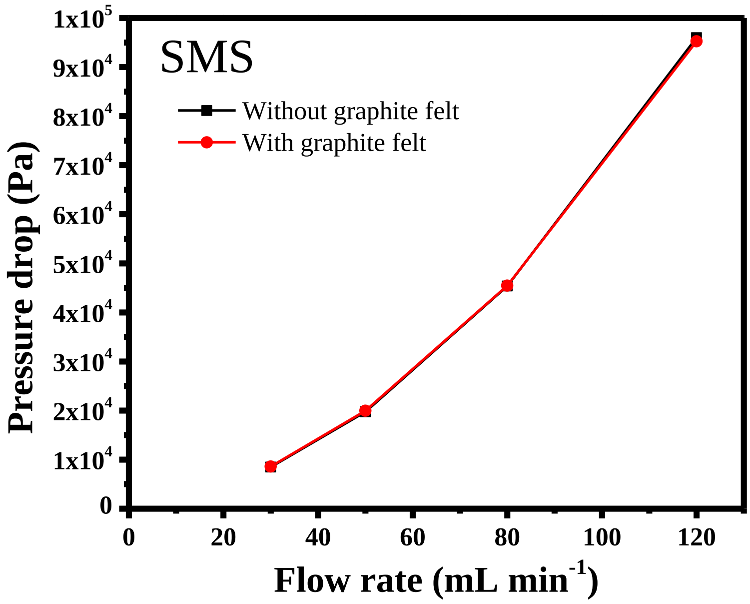

Figure A.6. Flow rate (mL min^{-1}) vs. Pressure drop (Pa) graph of SMS channel.

A.7 Calculation of pressure drop for Sinusoidal Wave-Type Serpentine (SWS) channel without graphite felt:

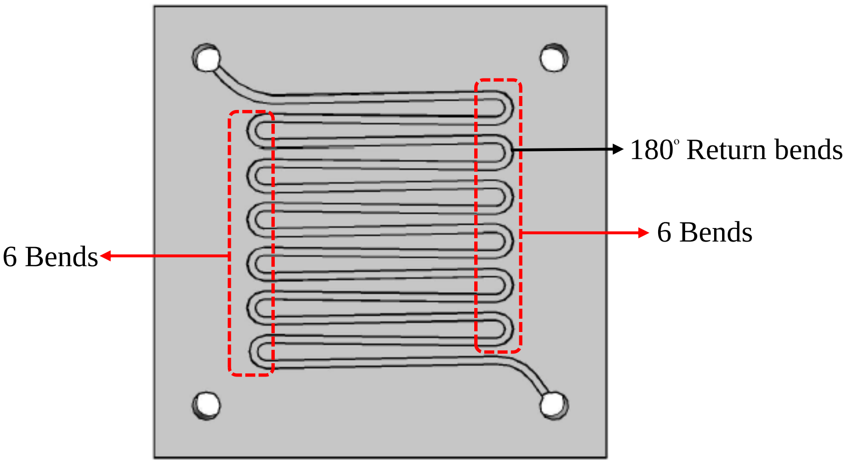

Figure A.7. Image of Sinusoidal Wave-Type Serpentine (SWS) channel.

- K_L = 0.2, for 180° return bend [138],
- Net value of K_L for return bends = 0.2 × 12 bends = 2.4
- Velocity of water at 30 mL min^{-1} = 0.5 m/s
- Distance between first and last channel = 32.5 mm

- Pressure drop at 30 ml/min = $\rho_{water} \times (4f\frac{L}{D} + K_L)\frac{v^2}{2} =$

$$1000 \times (4 \times 0.032 \times \frac{0.416}{0.001} + 2.4) \times \frac{0.5^2}{2} = 6956 \text{ Pa}$$

Table A.8. Calculated pressure drop in SWS channel at 30, 50, 80, and 120 mL min^{-1}.

Flow rate, Q_t (mL min^{-1})	Velocity, v (m s^{-1})	N_{Re}	f	$4f\frac{L}{D}$	Pressure drop (Pa)
30	0.5	500	0.032	53	6956
50	0.83	830	0.019	32	11876
80	1.33	1330	0.012	20	19828
120	2.0	2000	0.008	13	31424

A.8 Calculation of pressure drop for Sinusoidal Wave-Type Serpentine (SWS) channel with graphite felt:

Table A.9. Comparison of calculated pressure drop in SWS channels and in graphite felt at 30, 50, 80, and 120 mL min^{-1}.

Total flow rate, Q_f (mL min^{-1})	Flow rate in channel (mL min^{-1}) = 0.99 × Q_f	Flow rate in felt (mL min^{-1}) = 0.01 × Q_f	Velocity in channel (m s^{-1})	Velocity in felt (m s^{-1})	N_{Re}	f	Pressure drop in channel, $\Delta P_{channel}$ (Pa)	Pressure drop in felt, ΔP_{felt} (Pa)	Total pressure drop = $\Delta P_{channel} + \Delta P_{felt}$ (Pa)
30	29.7	0.3	0.495	3.62×10^{-5}	495	0.0323	6883	261	7144
50	49.5	0.5	0.825	6.03×10^{-5}	825	0.0194	11799	436	12235
80	79.2	0.8	1.32	9.65×10^{-5}	1320	0.0121	19663	697	20360
120	118.8	1.2	1.98	1.44×10^{-4}	1980	0.0081	31062	1045	32107

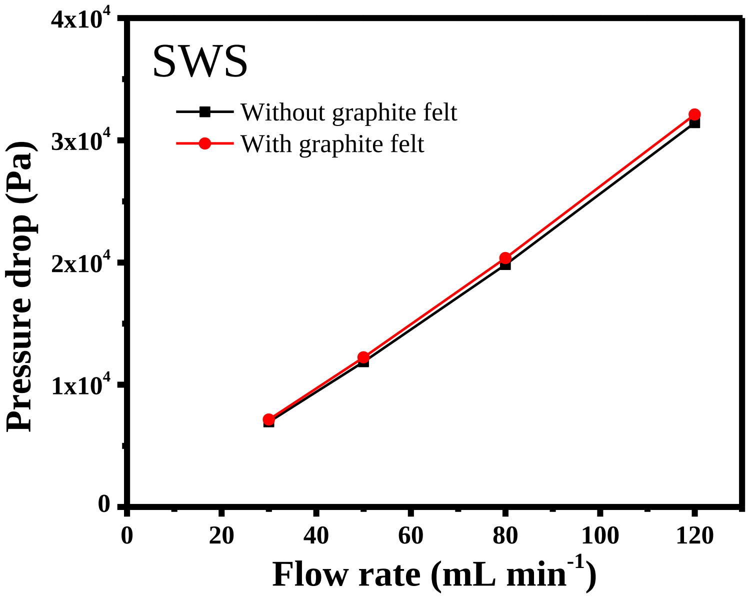

Figure A.8. Flow rate (mL min^{-1}) vs. Pressure drop (Pa) graph of SWS channel.

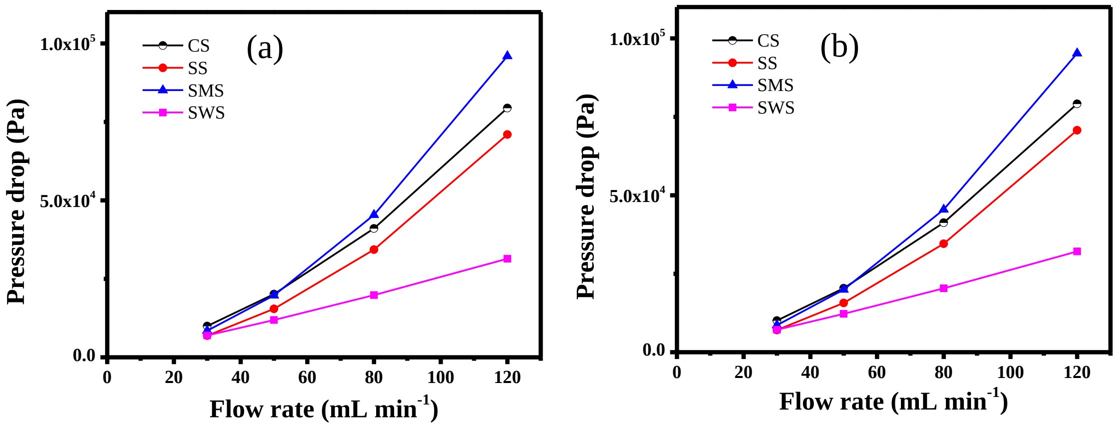

Figure A.9. Comparison of Flow rate (mL min^{-1}) vs. Pressure drop (Pa) graph for (a) without graphite felt (b) with graphite felt in CS, SS, SMS, and SWS channels.

List of Publications

- Harsh Sharma, Milan Kumar, Enhancing power density of a vanadium redox flow battery using modified serpentine channels, *Journal of Power Sources*. 494 (2021) 229753.
- Harsh Sharma, Milan Kumar, Energy efficient flow path for improving electrolyte distribution in a vanadium redox flow battery, *International Journal of Energy Research* (2022) 1–9.
- Harsh Sharma, Milan Kumar, Higher efficiency of a vanadium redox flow battery integrated with modified serpentine flow patterns. **(Under preparation)**
- Gargi Dey, Shadab Saifi, **Harsh Sharma**, Milan Kumar, *Arshad Aijaz, Nitrogen- and Oxygen-Decorated Highly Hydrophilic Porous Carbon Felt for High Performance Vanadium Redox Flow Battery. **(Submitted)**

List of workshops and presentations

- Global initiatives of Academic Networks (GIAN) "Fuel Cell Technology" a short course 5th -9th DECEMBER 2016 IIT Gandhinagar.
- 2nd National Workshop on Hydrogen Energy and Fuel Cells at the National Institute of Solar Energy 22 – 23rd NOVEMBER 2017 Gurugram.
- Harsh Sharma, Milan Kumar, " Performance Evaluation of $HClO_4$ as a Supporting Electrolyte in Vanadium Redox flow Battery" Oral presentation in Chemcon-2019 Conference held at IIT Delhi during 15 –19th December 2019.

___________________________End___________________________